

UNIVERSITY OF VIRGINIA

DOCTORAL THESIS

**Rubidium Ionic Core Polarization and
Non-Adiabatic Correction Using RF and
Microwave Spectroscopy of Rydberg States**

SETH BERL

M.A. Physics, University of Virginia, 2017

B.S. Physics, Old Dominion University, 2014

B.S. Electrical Engineering, Old Dominion University, 2014

*A Dissertation presented to the Graduate Faculty of The University of Virginia in
Candidacy for the Degree of Doctor of Philosophy*

Department of Physics



July, 2020

Copyright © 2020 Seth Berl

All rights reserved.

“This institution [The University of Virginia] will be based on the illimitable freedom of the human mind. For here we are not afraid to follow truth wherever it may lead, nor to tolerate any error so long as reason is left free to combat it.”

– Thomas Jefferson

December 27, 1820

Copyright © 2020 Seth Berl

All rights reserved.

UNIVERSITY OF VIRGINIA

*Abstract***Rubidium Ionic Core Polarization and Non-Adiabatic Correction Using RF and
Microwave Spectroscopy of Rydberg States**

by SETH BERL

Advisor: Charles Sackett

Department of Physics

Doctor of Philosophy

A precision measurement of the rubidium ionic core polarizability has been realized at The University of Virginia. Development and implementation of a rubidium Rydberg state spectroscopy apparatus, an appropriate model for interpreting spectroscopic results, analysis, and conclusions are documented and presented herein. Due to experiment design, the spectroscopy measurements in this dissertation feature a greater precision and higher fidelity due to less pronounced systematic effects when compared to previous experiments. Furthermore, the implementation of a non-adiabatic core polarization correction leads to a core polarizability result that is more precise and commensurate with theory, potentially resolving a long-standing discrepancy between experiment and theory. These results may prove to be useful in future experiments and interpretation including, but not limited to: parity non-conservation, black-body radiation shifts in atomic clocks, and quantum computation.

Acknowledgements

First and foremost, I would like to thank and acknowledge my parents. Their continued support and encouragement has helped me succeed in my career, schooling, and hobbies.

I would like to thank my advisor, Professor Cass Sackett. I am very happy to have had the opportunity to work with and learn from Cass on very interesting research projects. Throughout my tenure at UVa, Cass has afforded me the opportunity to work on three distinct and exciting projects. He is an unparalleled mentor with a willingness to be accessible, possesses an incredible breadth of knowledge, and has an extraordinary ability to convey that knowledge in an understandable fashion to his graduate students.

I would also like to thank Professor Tom Gallagher. On one of the projects facilitated by Cass, I had the honor and privilege of working with Tom; his knowledge and expertise in Rydberg atoms have greatly aided my understanding of the greater field of atomic physics. In addition to Tom, I would like to thank Olivier Pfister and Ian Harrison for serving on my Ph.D committee. My committee members have provided great feedback, insights, and dialog to better articulate and understand the physics of my research.

I am also grateful for my laboratory colleagues for which I have learned so much. Jirakan Nunkaew, a former student of Tom's, possesses an incredible knowledge of non-adiabatic corrections to alkaline earth metal atoms and her assistance in the analysis is greatly appreciated. Adam Fallon was an invaluable resource when I first entered the laboratory. His experimental know-how and methodology are excellent. I would like to also thank Edward Moan, Zhe Lou, and Marybeth Beydler for their contributions to other projects that I have had the privilege to work on while in Cass' laboratory.

Furthermore, I would not have had all of these opportunities without former professors and mentors such as Gail Dodge, Charles Sukenik, Harold Metcalf, and Vikki Wismer.

Contents

Abstract	iv
Acknowledgements	v
List of Figures	x
List of Tables	xiii
List of Abbreviations	xv
List of Symbols	xvii
1 Introduction	1
1.1 Motivation	1
1.2 Atomic Parity Violation	4
1.3 Dipole Matrix Elements	8
1.4 Rydberg atoms	12
1.5 Core polarization model	15
1.6 Non-adiabatic correction of the core polarization model	16
1.7 This Work	18
References	21
2 Experimental systems and methods	26
2.1 Vacuum system	28
2.1.1 Pump method	30

2.1.2	Experimental region	32
2.2	Atom beam	34
2.3	Dye laser system	37
2.3.1	$5s \rightarrow 6p$ laser setup	41
2.3.2	$4d \rightarrow nf$ laser setup	43
2.4	Microwave and rf systems	46
2.4.1	Synthesizers	47
2.4.2	Microwave signal transmission	47
2.4.3	Rf signal application	49
2.5	Detection & data acquisition systems	50
2.5.1	Field ionization	50
2.5.2	Signal detection and processing	55
2.6	Experiment timing	59
	References	64
3	Atomic spectra measurements	66
3.1	Introduction	66
3.1.1	Fine structure	67
3.1.2	Spectral linewidth broadening	70
3.1.3	DC Stark effect	71
3.1.4	AC Stark effect	76
3.1.5	Zeeman effect	79
3.1.6	Lineshape analysis	80
3.2	Single-photon transition	81
3.2.1	DC Stark shift	82
3.2.2	Zeeman shift	86
3.2.3	Fine structure	88

3.2.4	Spectroscopy results	89
3.3	Two-photon transition	90
3.3.1	DC Stark shift	92
3.3.2	AC Stark shift and spectroscopy results	93
3.4	Three-photon transition	96
3.4.1	DC Stark shift	99
3.4.2	AC Stark shift and spectroscopy results	100
3.5	Summary of results	102
	References	103
4	Ionic dipole and quadrupole core polarizabilities	105
4.1	Core polarization model	105
4.1.1	Theory	106
4.1.2	Results and analysis	108
4.1.3	Comparison to previous work	109
4.2	Non-adiabatic core polarization model	112
4.2.1	Theory	112
4.2.2	Non-adiabatic corrected results	127
4.2.3	Comparison to theory	130
4.3	Quantum defects	130
4.3.1	Comparison to previous work	132
	References	134
5	Conclusion and future work	139
5.1	Summary of results	140
5.2	Comparison to previous work	141
5.3	Future work	142
5.4	Impact of this work	144

References	146
A Rubidium core polarization paper submitted for publication	148
B Hydrogen Radial Functions and Spherical Harmonics	158
C Expectation values for hydrogenic states	160
D Calculated quantum defects for $n = 10 - 40, \ell = 4 - 8$	161
E 3D printed coil forms	167
F Continuum Surelite SLI-20 Trigger Setup	168
G LabView experiment control software	174
G.1 Front panel	174
G.2 Back panel	175
H Laser dyes	178
H.1 Stilbene 420	179
H.2 LDS 722	180
Index	181

List of Figures

1.1	Weak mixing angle as a function of particle interaction energy	3
1.2	Rb $5s_{1/2} \rightarrow 6s_{1/2}$ energy level illustration	5
1.3	Rb atom polarizability as a function of wavelength between the $5p_{1/2}$ and $5p_{3/2}$ transitions	11
1.4	Alkali Rydberg atom showing the ionic core and valence electron, similar to Hydrogen	13
2.1	Illustration of the vacuum system, including the experimental region and vacuum pumps	29
2.2	Illustration of the operation of a rotary vane pump	31
2.3	Illustration of the operation of a diffusion pump	33
2.4	Illustration of the experimental region of the vacuum chamber	35
2.5	Rb oven schematic using a stainless steel tube	38
2.6	Atomic states used in this experiment	39
2.7	Littrow and Littman-Metcalf laser configurations	42
2.8	$4d \rightarrow nf$ dye laser cavity configuration with a single beam expanding prism	44
2.9	Bias tee circuit diagram	50
2.10	Experiment setup without the vacuum chamber	51
2.11	Illustration of the ionizing field pulse amplitude as a function of principal quantum number	53
2.12	Field ionization circuit	54
2.13	Measured field ionization amplitude versus n	56

2.14	Illustration of the operation of a multi-channel plate	56
2.15	Dual multi-channel plate detector design	58
2.16	Multi-channel plate circuit diagram	59
2.17	Experiment timing diagram illustration	60
2.18	Laser trigger connection diagram	61
2.19	Experimental system block diagram	62
3.1	Doublet fine structure center of gravity	68
3.2	Hydrogen Stark map centered at $n = 17 - 19$	74
3.3	Rubidium Stark map centered at $n = 17 - 19$	75
3.4	Calculated Stark shifts for the $n = 17 f \rightarrow g, f \rightarrow h,$ and $f \rightarrow i$ transitions .	76
3.5	Illustration of a three-level system and two-photon transition	77
3.6	Single photon transition for nf to ng	81
3.7	Typical ionization signals for $n = 17 - 19 f \rightarrow g$ single photon transitions .	83
3.8	Measured dc Stark shift for $17f_{5/2} \rightarrow 17g_{7/2}$	84
3.9	Experimental measurements of Zeeman shifts along the X and Y axes	87
3.10	Two-photon transition illustration for nf to nh	91
3.11	Typical ionization signals for a two-photon transition	92
3.12	Measured dc Stark shift for $17f_{5/2} \rightarrow 17h_{9/2}$	94
3.13	Typical ac Stark shift measurement for $19f_{5/2} \rightarrow 19h_{9/2}$ with respect to mi- crowave power	95
3.14	Three-photon transition illustration for nf to ni	97
3.15	Typical ionization signal for a three-photon transition	97
3.16	Measured dc Stark shift for $17f_{5/2} \rightarrow 17i_{11/2}$	99
3.17	Typical ac Stark shift measurements for $19f_{5/2} \rightarrow 19i_{11/2}$ with respect to microwave and rf power	101
4.1	Core polarizability measurement results in the adiabatic approximation . . .	110

4.2	Core polarizability measurement by Lee, <i>et al.</i>	111
4.3	Energy level diagram showing ion states, Rydberg bound states, and the continuum	113
4.4	Energy distribution of the 18g Rydberg matrix elements	122
4.5	Core polarizability with the non-adiabatic correction	129
E.1	Coil forms to fit around the vacuum chamber for a bias magnetic field . . .	167

List of Tables

1.1	Azimuthal quantum number and corresponding atomic sublevel orbital . . .	5
1.2	Rydberg atom properties exaggerated at high n	13
1.3	Rb quantum defects for $0 \leq \ell \leq 5$	16
2.1	5s to 6p transition wavelengths	42
2.2	Laser dyes and concentrations	43
2.3	Laser wavelength measurements for the $4d_{3/2} \rightarrow nf_{5/2}$ transition measured by a monochrometer	45
2.4	Calculated microwave transition frequencies using the previous experimen- tal results	46
2.5	Waveguide names and characteristics	48
2.6	Tabulated lifetimes of high- ℓ H and Rb Rydberg states	52
2.7	Estimated lifetimes of high- ℓ Rb Rydberg states	52
2.8	Measured ionization field pulse amplitude thresholds for $n = 16 - 19$. . .	55
2.9	SRS DG 535 delay generator parameters	61
3.1	Spin-orbit interaction calculated values	69
3.2	Spin-orbit interaction energy ratios for the ℓ states of interest	69
3.3	Calculated dc Stark shift polarizability coefficients	73
3.4	Calculated dc Stark shift systematic uncertainty for $n = 17 - 19 f_{5/2} \rightarrow 19g_{7/2}$	85
3.5	Measured transition frequencies for $17f_{5/2} \rightarrow 17g_{7/2}$ and $17f_{7/2} \rightarrow 17g_{9/2}$.	88
3.6	Measured transition frequencies for $n = 17 - 19 f_{5/2} \rightarrow g_{7/2}$	90
3.7	Measured transitions frequencies for $n = 17 - 19 f_{5/2} \rightarrow g_{7/2}$	90

3.8	Calculated dc Stark shift systematic uncertainty for $n = 17 - 19 f_{5/2} \rightarrow 19h_{9/2}$	93
3.9	Measured transition frequencies for $n = 17 - 19 f_{5/2} \rightarrow h_{7/2}$	96
3.10	Measured transitions frequencies for $n = 17 - 19 f_{5/2} \rightarrow h_{9/2}$	96
3.11	Calculated dc Stark shift systematic uncertainty for $n = 17 - 19 f_{5/2} \rightarrow 19i_{11/2}$	100
3.12	Measured transitions frequencies for $n = 17 - 19 f_{5/2} \rightarrow i_{11/2}$	101
3.13	Measured transitions frequencies for $n = 17 - 19 f_{5/2} \rightarrow i_{11/2}$	102
3.14	Measured transition frequencies and calculated center of gravity transition frequencies	102
3.15	Center of gravity transition frequencies with systematic uncertainties con- sidered	103
4.1	Core polarizability measurement results in the adiabatic approximation . . .	109
4.2	Ionization limits and first excited state energies for H, Kr, and Rb^+	125
4.3	Non-adiabatic correction factors	127
4.4	Quantum defects for $n = 17$ to $19 g, h,$ and i states	132
4.5	Quantum defect Ritz expansion coefficients	133
5.1	Non-adiabatic corrected experimental results in this work compared to pre- vious experimental results and theory	139

List of Abbreviations

a.u.	Atomic Units
AC	Alternating Current
APV	Atomic Parity Violation
BNC	Bayonet Neill–Concelman Coaxial Connector
BNC	Berkeley Nucleonics Corp.
Cs	Cesium
DAT	Direct Access Triggering
DFI	Delayed Field Ionization
DG	Delay Generator
FET	Field Effect Transistor
H	Hydrogen
HV	High Voltage
Kr	Krypton
LDS	Linear Dichroism Spectrometry
MCP	Multi-Channel Plate
Nd:YAG	Neodymium-doped yttrium aluminum garnet
NI	National Instruments
PNC	Parity Non-Conservation
Rb	Rubidium
RF	Radio Frequency
SFI	Selective Field Ionization
SMA	SubMiniature version A Coaxial Connector

SRS Stanford Research Systems

List of Symbols

ω	angular frequency
Z	atomic number
ℓ	azimuthal quantum number
α_{core}	core polarizability
α_{cv}	core-valence polarizability
k_d	dipole non-adiabatic correction factor
α_d	dipole polarizability
\mathbf{d}	electric dipole moment
\mathcal{E}	electric field
e	electron charge
E	energy
α	fine structure constant
ν	frequency
g_s	gyromagnetic ratio of the electron
H	Hamiltonian
I	intensity
g_j	Landé g-factor
B	magnetic field
m_j	magnetic quantum number
f	oscillator strength
h	Planck's constant
A	PNC transition rate

α	polarizability
W_{pol}	polarization energy
P	power
σ_{PI}	photoionization cross-section
n	principal quantum number
k_q	quadrupole non-adiabatic correction factor
α_q	quadrupole polarizability
δ	quantum defect
Ω	Rabi frequency
d_{if}	reduced dipole matrix elements
Ry	Rydberg constant
c	speed of light
j	total angular momentum quantum number
θ_w	weak mixing angle

*This dissertation is dedicated to my parents, Lenny and Donna Berl,
and my brother, Chad Berl.*

1 | Introduction

1.1 Motivation

The main driving force for this work, like most work in physics, is to better understand our universe. There are many questions that remain unanswered, and I hope this work serves to promote future research and understanding to potentially answer some of these questions. One of the largest motivations in physics at this moment in time is finding *physics beyond the Standard Model*. Ultimately, we are in the pursuit of *truth* and it is important to push the boundaries of what we currently know. This allows us to learn and form a more complete knowledge of phenomena in the future. There are countless examples throughout history where an explanation is improved upon by probing further to facilitate a more robust theory succeeding.

The Standard Model is the best description of subatomic processes at the moment, but does not characterize all phenomena. By pushing the boundary of the Standard Model and further exploring physics that support this goal, we can hope to learn a great deal of novel physics and improve theories. Some phenomenons that are not well characterized by the Standard Model include, but are not limited to: dark matter, dark energy, matter/anti-matter asymmetries, and neutrino oscillations.

The fine details of the Standard Model and its theories and subatomic particles are outside the scope of this dissertation; however, one may learn more by reviewing Ref. [1, 2]. The main goal of this work is to help facilitate the exploration of physics beyond the Standard Model by supporting efforts that investigate fundamental symmetries.

A symmetry is characterized as an invariance of a system under a transformation; and a *fundamental symmetry* is characterized as an invariance of the universe under a transformation. Theories generally encompass observed symmetries, however if a symmetry is proven to be broken experimentally, the theory is then adapted to take these factors into account. The fundamental symmetry of interest to this work is parity symmetry. Under a *parity transformation*, spatial coordinates (X , Y , and Z) are reflected.

$$\begin{pmatrix} X \\ Y \\ Z \end{pmatrix} \rightarrow \begin{pmatrix} -X \\ -Y \\ -Z \end{pmatrix} \quad (1.1)$$

Parity is conserved in electromagnetic, strong, and gravitational interactions; however, parity is not conserved in weak interactions [3]. *Parity violation* present in weak interactions are represented as a chiral process in the Standard Model with left-handed components for particles and right-handed components for anti-particles. Given the chirality of this process, parity symmetry is not considered to be a fundamental symmetry of the universe [4]. This parity asymmetry in the weak interaction may be important in understanding matter and anti-matter asymmetries in our universe and further testing and potentially adapting the Standard Model.

One of the major deficiencies of the Standard Model is its inability to explain matter-antimatter asymmetry, the observed difference between imbalance in baryonic matter in the observable universe. Within the Standard Model and General Theory of Relativity, a system remains unchanged under a charge (C) conjugation. Along this line of reasoning, special relativity requires charge-parity-time (CPT) symmetry, implying that under a mirror-image of our universe corresponding to a reversal of charge, parity, and time, the universe would evolve in the same fashion. Therefore, charge, parity and time are all related, and studied intensely within the physics community. The primary interest of this work is to support further research into the violation of parity symmetry.

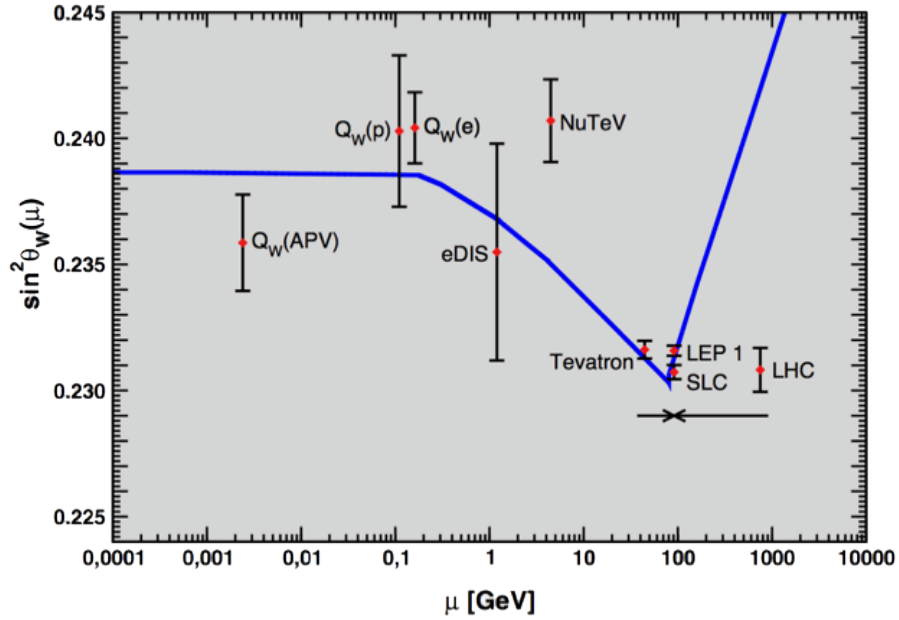


FIGURE 1.1: The weak mixing angle, $\sin^2(\theta_w)$, as a function of particle interaction energy. The Standard Model theory prediction is denoted by the line and the data points are from experiments [5, 6]. The arrows indicate the energy region where a new particle is created, also explaining the turning point in the Standard Model prediction.

Parity violation is characterized in the Standard Model by the *weak mixing angle* (θ_w). The weak mixing angle is the measure of parity conservation, with parity conserved when $\theta_w = 0$ and violated when $\theta_w = \pi/2$, corresponding to $\sin^2(\theta_w) = 0$ and $\sin^2(\theta_w) = 1$ respectively. The degree to which parity violating effects are manifested depends upon the energy of the particle interactions. Figure 1.1 shows the Standard Model prediction for the weak mixing angle, displayed as the line, and experimental results as data points [5]. The energy scales at which this process can be observed range from the atomic level to high-energy nuclear level.

As expected, new experiments, improved theory, simulations, and calculations lead to reduced uncertainty. However, it is clear from the plot that the Standard Model theory does not agree with experimental results across all interaction energies. For this reason, there is a lot of interest in the areas of parity violation and the weak interaction with new

experiments being proposed and conducted regularly. Most of the experiments to date have been conducted at high particle interaction energies and are characterized as nuclear and high energy measurements; however, one experiment was conducted at low particle interaction energies, labeled *atomic parity violation* (APV) [7]. In the case of the 1997 APV measurement shown in Figure 1.1, parity non-conserving effects (PNC) were observed by measuring a transition rate between the $6s$ and $7s$ even parity states in Cesium. To further explore atomic parity violation and the Standard Model, Carl Wieman presents a concise review in Ref. [8].

The goal of the work presented here is to help garner interest in motivating another APV measurement in the future; this time using rubidium (Rb) as the species being investigated instead of Cesium (Cs). Measurements using each species present advantages and disadvantages. The main advantage for rubidium is that there have been significant advances in measurement and theory of electronic dipole moments [9]. The primary disadvantage of investigating APV in rubidium is the fact that parity non-conservation effects scale as Z^3 , where Z is the atomic number. This means that APV effects are approximately 3 times smaller in Rb compared to Cs, and thus more difficult to measure.

1.2 Atomic Parity Violation

Parity violation in an atomic system is dependent upon the atomic wavefunction and can be observed as an electric dipole transition between two states of the same parity. In the case of Cesium presented above, the transition measured is the $6s$ ground state to the $7s$ excited state [7]. For rubidium, APV effects could be observed in the $5s$ ground state to $6s$ excited state transition. To get an idea for the energy scale for this transition, Figure 1.2 depicts the energy between the $5s_{1/2}$ ground state and $6s_{1/2}$ excited state of rubidium. The transition between these states is forbidden by *selection rules*, but shown here nonetheless for scale. Selection rules are discussed further in this section.

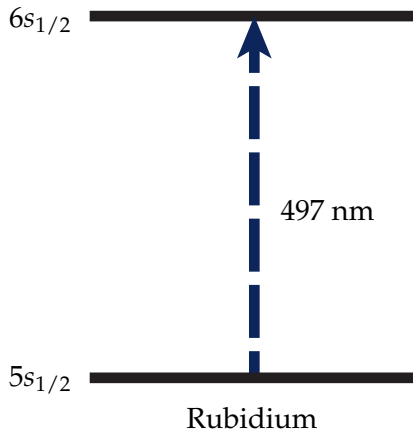


FIGURE 1.2: Rubidium $5s_{1/2}$ to $6s_{1/2}$ states for illustrative purposes of the energy separation. A transition between these energy levels are forbidden by conservation of angular momentum and parity, but can be observed through an APV experiment.

ℓ	<i>Orbital</i>
0	s
1	p
2	d
3	f
4	g
5	h
6	i
\vdots	\vdots

TABLE 1.1: Azimuthal quantum number and corresponding atomic sublevel orbital.

Atomic orbitals have $(-1)^\ell$ parity with $\ell = 0, 2, 4, \dots$ being *even* parity and $\ell = 1, 3, 5, \dots$ being *odd* parity. The azimuthal quantum number, ℓ , corresponding to the orbital angular momentum, is shown in Table 1.1. The atomic wavefunction for even parity would be

$$\Psi_{n\ell m}(-\mathbf{r}) = \Psi_{n\ell m}(\mathbf{r}). \quad (1.2)$$

And, the atomic wave function for odd parity would be

$$\Psi_{n\ell m}(-\mathbf{r}) = -\Psi_{n\ell m}(\mathbf{r}). \quad (1.3)$$

Ultimately, the even or odd behavior of the wavefunction is dictated by the atomic orbitals. The wave function in terms of the radial $R_{n\ell}(r)$ and spherical harmonics functions $Y_{\ell m}(\theta, \phi)$ are

$$\Psi_{n\ell m}(r, \theta, \phi) = R_{n\ell}(r)Y_{\ell m}(\theta, \phi) \quad (1.4)$$

for a hydrogen atom in spherical coordinates. The radial and spherical harmonics are independent of each other and can be evaluated separately. Appendix B contains a list of the first few *radial functions* and *spherical harmonics*. It follows that under a parity inversion, $r \rightarrow r$, $\theta \rightarrow \pi - \theta$, and $\phi \rightarrow \phi + \pi$, the radial portion of the wavefunction remains unchanged $R_{n\ell}(r) = R_{n\ell}(r)$ as expected. However, the spherical harmonic under a parity inversion is given by

$$Y_{\ell m}(\pi - \theta, \phi + \pi) = (-1)^\ell Y_{\ell m}(\theta, \phi). \quad (1.5)$$

The wavefunction is therefore an eigenfunction of parity with the $(-1)^\ell$ dependence being evident.

Now that the parity of the Hydrogen wavefunction has been shown, attention can be turned to the total angular momentum. Total angular momentum and parity are both

conserved with the following condition is satisfied

$$\mathbf{J}_i = \mathbf{J}_f + \gamma. \quad (1.6)$$

The angular momentum and parity of the initial atomic state \mathbf{J}_i must be the same as the combined angular momentum and parity of the final atomic state \mathbf{J}_f and angular momentum of the interacting photon γ . Angular momentum $\mathbf{J} = \mathbf{L} + \mathbf{S}$ where \mathbf{L} is the orbital angular momentum and \mathbf{S} is the spin. For parity to be conserved, $|n\ell\rangle \rightarrow |n'\ell\rangle$ would be a *forbidden transition* based upon the above principles and the $\Delta\ell = \pm 1$ *selection rule* for an electric dipole transition. Here, n is the principal quantum number, ℓ is the azimuthal quantum number, and m the magnetic quantum number. Just as described above, a photon interacting with an atomic state must exchange at least quantum of angular momentum for an electric dipole transition, reflected as a change in the ℓ atomic sublevel.

The *PNC transition rate*, $A_{\text{PNC}}^{\text{Theory}}$, of parity non-conservation effects in theory is represented as a second order perturbation and shown in Eqn. (1.7). This process is dependent upon the electric dipole moment $\mathbf{d} = e\mathbf{r}$ and the parity non-conserving Hamiltonian H_{PNC} .

$$A_{\text{PNC}}^{\text{Theory}}(\text{Rb}) = \sum_{n'=5}^{\infty} \left(\frac{\langle 6s_{1/2} | \mathbf{d} | n'p_{1/2} \rangle \langle n'p_{1/2} | H_{\text{PNC}} | 5s_{1/2} \rangle}{E_{5s_{1/2}} - E_{n'p_{1/2}}} + \frac{\langle 6s_{1/2} | H_{\text{PNC}} | n'p_{1/2} \rangle \langle n'p_{1/2} | \mathbf{d} | 5s_{1/2} \rangle}{E_{6s_{1/2}} - E_{n'p_{1/2}}} \right) \quad (1.7)$$

APV coupling strength is given by $\langle n'p_{1/2} | H_{\text{PNC}} | ns_{1/2} \rangle$ and the dipole matrix elements are given by $\langle ns_{1/2} | \mathbf{d} | n'p_{1/2} \rangle$. State 5s and 6s transitions are depicted in the atomic parity violation transition amplitude to reflect Rb as the species being investigated. The PNC transition rate is in turn related to the weak mixing angle through knowledge of dipole

matrix elements, either measured or calculated. It is therefore apparent that parity non-conserving effects are manifested as the mixing of $|n'p_{1/2}\rangle$ states into the $|ns_{1/2}\rangle$ states [7].

Unfortunately, atomic theory uncertainties are currently the dominant limiting factor in evaluating the weak mixing angle from the APV experiment. These theoretical uncertainties stem from additional experimental uncertainties and unknowns when calculating the dipole matrix elements. In order to relate the measurable APV transition rate A_{PNC} to the motivational goal of further constraining weak mixing angle $\sin^2(\theta_w)$ to test the Standard Model, the PNC Hamiltonian H_{PNC} must be determined. To accomplish this, the electric dipole matrix elements, $\langle n'p_{1/2}|\mathbf{d}|ns_{1/2}\rangle$, must be known.

1.3 Dipole Matrix Elements

Dipole matrix elements can be experimentally measured both directly and indirectly. A direct measurement of dipole matrix elements can be achieved through *spontaneous emission*. The rate of spontaneous emission between two states, i and f is represented in Eqn. (1.8).

$$\Gamma_{i \rightarrow f}^{\text{spn}} = \frac{4\alpha\omega_{if}^3 |d_{if}|^2}{3c^2} \quad (1.8)$$

where α is the fine structure constant, c is the speed of light, d_{if} is the dipole reduced matrix element, and $\omega_{if} = (E_i - E_f)/\hbar$ [10].

However, measuring spontaneous emission accurately is challenging. The spontaneous emission rate equation, Eqn. (1.8), provides some key insights into these weak coupling effects. Further analyzing this equation shows that the spontaneous emission transition rate depends on the transition frequency (ω_{if}) and electric dipole moments, displayed in this equation as reduced dipole matrix elements d_{if} . For higher frequency transitions, transitions with large energy level separation, the spontaneous transition rate occurs

more rapidly. For lower frequency transitions, the transition rate is slower. Additionally, higher spontaneous emission rates are allowed for larger electric dipole matrix elements. Due to this dependence on electric dipole matrix elements, transitions that are forbidden by selection rules have a small probability of occurring. The very low probability of the forbidden $5s \rightarrow 6s$ transition occurring for an APV measurement makes measurement of this effect to better than 10^{-3} uncertainty a challenge [11, 12].

Indirect measurement of dipole matrix elements using *electric polarizability* is an alternative approach with more easily identifiable effects. The relationship between polarizability and the dipole matrix elements is

$$\alpha \sim \sum_{n'=5}^{\infty} \frac{|\langle n' p_{1/2} | \mathbf{d} | 5s_{1/2} \rangle|^2}{E_{5s_{1/2}} - E_{n' p_{1/2}}} \quad (1.9)$$

with $\mathbf{d} = e\mathbf{r}$ being the electric dipole moment introduced above. There is a clear and evident dependency of electric dipole polarizability on electric dipole matrix elements.

Electric dipole polarizability measurements are accomplished by applying an electric field and observing the response of the atom. This is known as the *Stark effect* and shown in Eqn. (1.10).

$$\Delta E = -\frac{1}{2}\alpha \langle \mathcal{E} \rangle^2 \quad (1.10)$$

where α is the electric polarizability and \mathcal{E} is an externally applied electric field. This therefore scales linearly depending upon the electric field intensity $I = c\epsilon \langle \mathcal{E} \rangle^2$, where c is the speed of light and ϵ is relative permittivity.

$$\langle \Delta E \rangle = -\frac{1}{2c\epsilon} \alpha(\omega) I \quad (1.11)$$

A strong electric field can be achieved with a laser, however it is non-trivial to calibrate laser intensity accurately; thus this is a limiting factor in polarizability measurement uncertainty. The polarizability term α was replaced with $\alpha(\omega)$ between equations Eqn. (1.10)

and Eqn. (1.11) to show a *dynamic polarizability*, or polarizability dependent on external electric field frequency. There are techniques such as *tune-out wavelength spectroscopy* utilizing the ac Stark effect in Eqn. (1.11) to better constrain polarizability measurements [13]. The tune-out wavelength is the wavelength where atom polarizability goes to zero. The polarizability of rubidium between the $5p_{1/2}$ and $5p_{3/2}$ transitions are shown in Figure 1.3. Since tune-out wavelength spectroscopic measurements are concerned with measuring where atom polarizability is equal to zero, precision measurements are possible. This is because the tune-out wavelength measurement is independent of laser intensity, the dominant source of uncertainty in polarizability measurements. This is of significant interest to the Sackett research group with the work presented here in support of the tune-out wavelength measurements. More information about the tune-out wavelength measurements can be found in Ref. [14].

Theoretical computation of dipole matrix elements is possible; however, it is difficult to know the accuracy. Challenges to this calculation accuracy stems from small final calculated numbers and large correlation corrections required for different contributions. Individual dipole matrix elements are able to be calculated to 10^{-4} with heavy computational resources required to obtain each individual matrix element value. However, there are an infinite number of terms, and computation results in a finite number as a result. Additionally, the polarizability has been presented without core contributions. For atoms with a single valence electron, the total polarizability of the atom can be separated to account for two contributions: the polarizability of the valence electron and the polarizability of the core. The core contribution is similar to that of the corresponding ion which is denoted as α_{core} . However, there is an additional correction because the ionic polarizability is modified by the presence of the valence electron. This correction is denoted as α_{cv} [15, 16]. For Alkali atoms, the valence contribution of the ground state polarizability is primarily dominated by the contribution from the lowest excited state. In the case of Rb^+ , the $5s_{1/2} \rightarrow 5p_{1/2}$ and $5s_{1/2} \rightarrow 5p_{3/2}$ transitions contribute more than 99% of the Rb valence polarizability

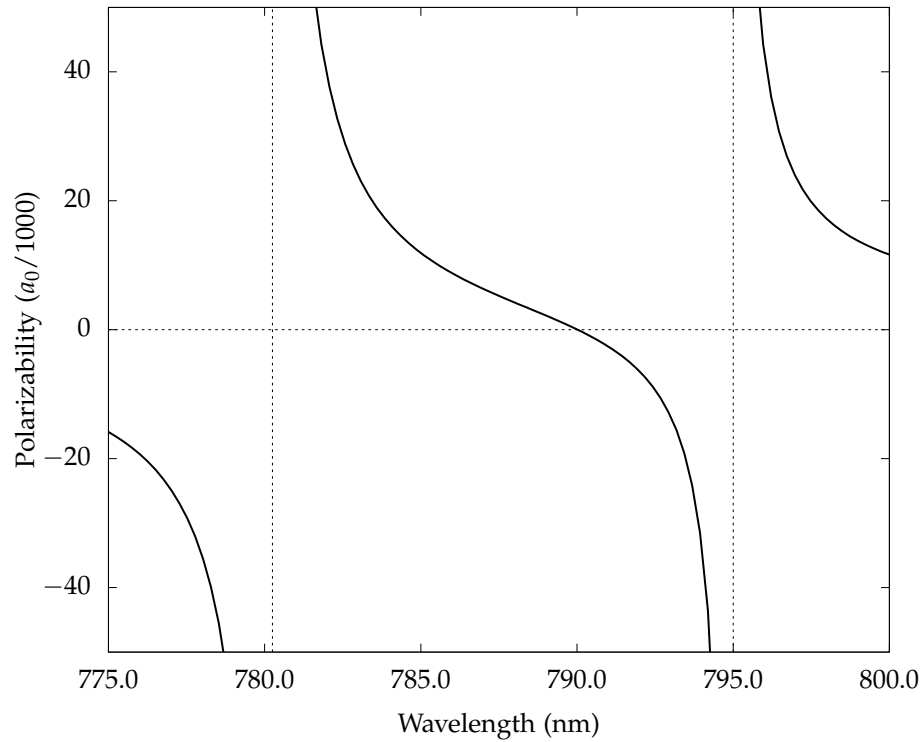


FIGURE 1.3: Atom polarizability as a function of wavelength between the $5p_{1/2}$ and $5p_{3/2}$ transitions, illustrated with dotted lines. A tune-out wavelength is located where the polarizability crosses zero, near 790 nm. Polarizabilities are calculated as a function of wavelength given by the polarizability contributions in Ref. [9].

[17]. As for the total polarizability, the Rb ionic core polarizability contributes a significant portion, approximately 11% [18]. With these additional terms, the polarizability can be expressed as shown in Eqn. (1.12).

$$\alpha = \sum_{n'=5}^{\infty} \frac{|\langle n' p_{1/2} | \mathbf{d} | 5s_{1/2} \rangle|^2}{E_{5s_{1/2}} - E_{n' p_{1/2}}} + \alpha_{core} + \alpha_{cv} \quad (1.12)$$

Ultimately, the theories combine with experimental measurements to infer the values of the dipole matrix elements. Therefore, high-precision measurements better constraining the matrix elements and contributions from other effects are required [18]. The atomic core and high-lying valence state manifold effects can be determined, and knowledge of these are required for relating to atomic parity violation measurements. These contributions are relatively small; however, they are the dominant source of uncertainty in interpreting experimental results. And of primary interest herein, the atomic core polarizability contribution α_{core} is investigated and determined directly by a Rydberg atom experiment.

1.4 Rydberg atoms

A *Rydberg atom* is an atom in a state of high principal quantum number, n . Generally, these include atoms of principal quantum number $n > 10$. Rydberg atoms have long been of interest due to their exaggerated properties such as size, geometric cross section, long lifetime, low binding energy, and large dipole moment. These exaggerated properties lead to a high sensitivity to electric and magnetic fields, long decay times compared to the ground state, and wavefunctions that can sometimes be approximated by classical orbits. Table 1.2 shows how some atom properties scale with principal quantum number [19].

Alkali metals, identified in group 1 of the periodic table of elements, have one valence electron. Due to the large orbit radius of the alkali Rydberg atom, the valence electron is spatially distant from the core; where the core is defined as the atom nucleus and core electrons with the valence electron excluded. The core electrons effectively shield the valence

Property	n dependence
Binding energy	n^{-2}
Energy between adjacent n states	n^{-3}
Orbital radius	n^2
Geometric cross section	n^4
Dipole moment $\langle nd e\mathbf{r} nf \rangle$	n^2
Polarizability	n^7
Radiative lifetime	n^3
Fine structure interval	n^{-3}

TABLE 1.2: Rydberg atom properties are exaggerated at high principal quantum number, n . This table shows the scaling dependence of various atom characteristics based on n [19].

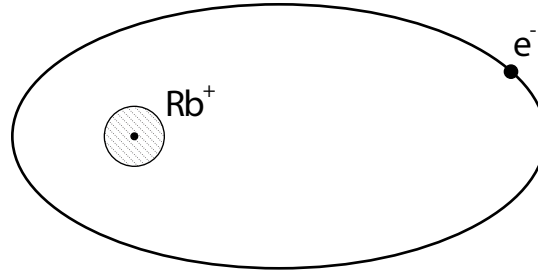


FIGURE 1.4: Rubidium Rydberg atom with core electrons, depicted as the shaded region, shielding the valence electron from the electric field of the nucleus. This figure is not drawn to scale to show the similarity of alkali metal Rydberg atoms with the hydrogen atom, and accentuating the cloud of core electrons of finite size.

electron from the electric field of the nucleus. The result is effectively a positive ionic core with one orbiting valence electron, depicted in Figure 1.4. This therefore resembles the hydrogen atom and can be approximated as such.

To account for the ionic core of the alkali Rydberg atom when compared to hydrogen, the resulting potential seen by the valence electron is deeper than that of just the Coulomb potential for hydrogen. This corrected potential is represented by

$$\text{P.E.} = -\frac{1}{r} - V_{\text{core}}(r) \quad (1.13)$$

where V_{core} is a short range potential difference between the alkali atom and Hydrogen. For $0 < r < r_0$, the radius of the rubidium core, the potential is non-zero. This is the correction that accounts for the polarization effects and the valence electron penetrating and the ionic core. For $r > r_0$, the lower potential of the alkali atom compared to Hydrogen manifests as a phase shift to the wavefunction and leads to a lower energy when compared to hydrogen.

The energies of the Rydberg states, denoted as W , are given by the *Rydberg formula*

$$W = \frac{-Ry}{(n - \delta_\ell)^2} \quad (1.14)$$

where Ry is the Rydberg constant and δ_ℓ corresponds to the phase shift to the wavefunction depressing the energies compared to hydrogen. This δ_ℓ is known as the *quantum defect*. The quantum defect corresponds to the correction to the Coulomb potential introduced earlier to account for core penetration and polarization effects. Additionally, it is sometimes convenient to use the effective principal quantum number $n^* = (n - \delta_\ell)$, and this convention will occasionally be used throughout this writing; and unlike n , n^* can be a non-integer because it is an effective quantum number.

For low orbital momentum states, the valence electron's orbit is highly elliptical and the valence electron comes close to or penetrates the core electrons on each orbit. Low orbital momentum states are characterized as $\ell < 4$ for rubidium. This results in polarization or penetration of the core and a depression of energy levels when compared to Hydrogen.

For high angular momentum states ($\ell > 3$), the orbit path is more circular and the valence electron is less likely to sample the ionic core. This results in high angular momentum states being less susceptible to core penetration effects. The dominant effect on the valence electron is thus due to core polarization. For this reason, it is the intent of this work to measure core polarization of rubidium α_{core} , as shown in Eqn. (1.12) by studying high angular momentum states of rubidium Rydberg atoms.

1.5 Core polarization model

The *core polarization model* makes the assumption that the valence electron is moving in a hydrogenic orbit around the ionic core and the ionic core is polarized by the electrostatic interaction with the valence electron [20, 21]. For $\ell > 3$ states of rubidium, where the valence electron energy shift from Hydrogen is mainly due to core polarization, the energy levels can be expressed (in atomic units, *a.u.*) as

$$W_{n\ell} = -\frac{1}{2n^2} + W_{pol} \quad (1.15)$$

where W_{pol} is the energy shift from Hydrogen due to core polarization. This equation thus neglects core penetration effects, and W_{pol} accounts for the energy shift due to core polarization effects, meaning that the quantum defect is now encompassed in this term.

First introduced by Born, the following equation approximates the polarization energy W_{pol} as

$$W_{pol} = -\frac{\alpha_d}{2} \langle r^{-4} \rangle - \frac{\alpha_q}{2} \langle r^{-6} \rangle \quad (1.16)$$

in a multipole expansion, with α_d and α_q being the dipole and quadruple polarizability, respectively [20]. Within the concepts and framework presented by Mayer and Mayer, the octopole and higher order terms in the expansion are treated as negligible [21]. The expectation values $\langle r^{-4} \rangle$ and $\langle r^{-6} \rangle$ are for the hydrogen wave functions and are tabulated analytically in Ref. [22]. Hydrogen wave functions can be used to determine the expectation values since this model assumes that the Rydberg electron is moving in a hydrogenic orbit around the ionic core with high ℓ states having quantum defects which are largely due to core polarization effects. The first term on the right hand side of Eqn. (1.16) corresponds to energy shift due to the static field of the Rydberg electron. The electric field from the Rydberg electron is given by $E = -1/r^2$ in atomic units, with $\langle r^{-4} \rangle$ corresponding to $\langle E \rangle^2$. The second term on the right hand side of Eqn. (1.16) corresponds to the

State	Quantum Defect
s	3.13
p	2.64
d	1.35
f	0.016
g	0.004
h	0.001

TABLE 1.3: Quantum defects for Rubidium. Due to increasingly circularity of the valence electron orbit at higher angular momentum states, the valence electron interacts less with the core. Therefore, core penetration effects decrease, and by consequence the quantum defect decreases.

energy shift as a result of the gradient of the field from the Rydberg electron, with $\langle r^{-6} \rangle$ corresponding to $|\nabla E|^2$.

Measurement of the core polarization effects and the quantum defects can be achieved through spectroscopic methods [23, 24, 25]. The quantum defects for $\ell = 0 - 5$ for rubidium are shown in Table 1.3. From this table, it is evident that as the angular momentum state increases, the quantum defect decreases. This is due to core penetration and core polarization effects decreasing due to the more circular orbit of the valence electron. This therefore results in the rubidium energy spectrum beginning to become more similar to hydrogen.

1.6 Non-adiabatic correction of the core polarization model

Up to this point in the formalism, the core polarization energy shift had been determined by the electrostatic interaction. Ignoring the time-dependence of the electric field due to the valence electron is known as the *adiabatic approximation*. However, the core polarizability is dynamic and the motion of the valence electron leads to a change in the energy shift. This dynamic polarizability effect is small, however it has the ability to affect the quadrupole polarizability term in a non-negligible manner.

For the adiabatic approximation presented earlier to be a representative approximation, the orbit of the valence electron must be sufficiently circular around the ionic core and absorption frequencies of the ionic core must be large compared to the Bohr frequencies of transitions accessible to the valence electron [26]. Therefore, for the adiabatic approximation to be applied to Rydberg atoms, the Bohr frequencies of the outer electron must be negligible compared to the ionic core states. In the case of alkali atoms such as rubidium, the energy difference between the ionic energy level of the core and the Rydberg electron states are relatively large, thereby meeting the conditions set forth above. Unlike an alkali atom, an alkaline earth atom core includes the inner valence electron and the energy difference between the ion states, and the Rydberg electron states are comparatively smaller. For example, the lowest lying excited state of the rubidium ionic core is 16.53 eV; whereas the lowest lying excited state of the Barium ionic core is 0.60 eV, comparable to the Rydberg energy intervals [27, 28]. This rationale has led to the assumption that non-adiabatic effects were significant for alkaline earth atoms and negligible for alkali atoms.

As introduced previously, the departure from the adiabatic approximation occurs when the ionic energy spacing is not large compared to the Bohr frequencies of the valence electron. The non-adiabatic effects thus reduce to the adiabatic approximated core polarization model when the ionic energy spacing is large. To characterize the non-adiabatic correction, it is useful to include correction factors, $k_{d,n\ell}$ and $k_{q,n\ell}$, to the adiabatic polarization energy in Eq (1.16) [19].

$$W_{pol} = -\frac{1}{2}k_{d,n\ell}\alpha_d\langle r^{-4} \rangle - \frac{1}{2}k_{q,n\ell}\alpha_q\langle r^{-6} \rangle \quad (1.17)$$

This equation and the non-adiabatic effect are explained further in Chapter 4, but for brevity here, only a brief overview is discussed. In the adiabatic approximation, $k_{d,n\ell} \rightarrow 1$ and $k_{q,n\ell} \rightarrow 1$. The adiabatic approximation corresponds to the case where the span of Rydberg energies is small compared to the ionic core energy level separation. Since the range of Rydberg energies are found to be appreciable compared to the ionic core for rubidium,

approximately 15%, it would be reasonable to take into account these non-adiabatic effects.

Prior to this work, it had not been realized that non-adiabatic effects were needed for polarizability determination in alkali atoms. Previously, non-adiabatic corrections had been applied to two-electron atoms or alkaline earth atoms, but not alkali metals. It has been believed that the adiabatic core polarization model was sufficient for alkali metal atoms; however this is found not to be the case. Furthermore, there has been a long-standing large discrepancy between experiments and theoretical calculations with reference to the quadrupole polarizability term. Discovering the source of this discrepancy is often cited as "future work" in publications. Previous experimental work cites dipole and quadrupole polarizabilities of $\alpha_d = 9.12 \pm 0.02$ a.u. and $\alpha_q = 14 \pm 3$, respectively. Theory cites dipole and quadrupole polarizabilities of $\alpha_d = 9.10 \pm 0.45$ a.u. and $\alpha_q = 34$, respectively [24, 18].

1.7 This Work

The Experimental systems and methods chapter details the design, rationale, and limitations of the apparatus used to accomplish the desired spectroscopic measurements. This experiment is performed under vacuum at a pressure of approximately 10^{-7} torr, measured by an ionization gauge. A diffusion pump is used to reach this pressure, with a mechanical rotary vane backing pump. Rubidium is heated by a home-built oven that ejects a hot atom vapor beam directed at the center of the experimental region of the vacuum chamber. Two home-built dye lasers are pumped by second and third harmonics of separate pulsed Nd:YAG lasers. These pulsed dye lasers are independently tuned to the $5s \rightarrow 6p$ and $4d \rightarrow nf$ transitions and both focused at the center of the experimental region within the vacuum system. A microwave field pulse is directed at the center of the experimental region to drive high angular momentum state transitions $nf \rightarrow ng$ and $nf \rightarrow nh$. The $nf \rightarrow ni$ transition is accomplished with a simultaneous combination of a microwave

field pulse and rf field pulse. The Rydberg atoms are ionized and the ions detected by a spatially integrating multi-channel plate. Ionization signal data is recorded and analyzed on a computer with a custom LabVIEW™ program.

The Atomic spectra measurements chapter discusses the spectroscopy measurements of the single-photon $nf \rightarrow ng$ transition, $nf \rightarrow nh$ two-photon transition, and $nf \rightarrow ni$ three-photon transition. Considerations are made for spectral linewidth broadening due to transform broadening, the Zeeman effect, and Rabi oscillations. External static electric fields are minimized within the constraints of the current apparatus with dc Stark shifts measured for the single, two, and three-photon transitions. AC Stark shifts are present for the two and three-photon transitions due to a time-dependent oscillating electric field. These shifts are accounted for by extrapolating the measured transition frequencies to zero electric field strength. The ng and higher angular momentum states are determined to be hydrogenic by measuring fine structure splitting for the successful application with the core polarization model. Upon consideration of these effects and accounting for the associated errors, spectroscopy results are presented.

Core polarization analysis and results are presented in the Ionic dipole and quadrupole polarizabilities chapter. The core polarization model in the adiabatic limit is first discussed [20, 21]. Core polarizability results are calculated with this adiabatic approximation and quantum defects are determined based on the calculated core polarizability. Comparisons to the previous work are discussed, primarily with an emphasis on the fact that this experiment yields an approximate three-fold improvement in precision. When compared to theoretical calculations, dipole polarizabilities are in reasonable agreement; however, there had been a relatively large discrepancy for the quadrupole polarizability value. This quadrupole polarizability discrepancy appears to be resolved upon applying a non-adiabatic correction to the core polarization model, with the dipole polarizability remaining in reasonable agreement. This approach is novel when applying to alkali metal atoms, and its successful application features an extrapolation of isoelectronic neutral Kr atomic

properties are made to the Rb^+ ionic core.

Finally, conclusions and future work are presented in the Conclusion and future work chapter. The dominant source of uncertainty in our results is due to the determination non-adiabatic effects, because accurate atomic structure calculations for Rb are not available at this time. Nevertheless, the dipole polarizability precision has been improved by over an order of magnitude compared to the estimate used in the previous tune-out wavelength studies [13]. Previously, the uncertainty of the core polarization was the single largest contribution to the the tune-out wavelength analysis. Using the new experimental results, the relative uncertainty of the tune-out matrix elements have been reduced by 20%. Further improvements can include better precision of the spectroscopic measurements and more accurate non-adiabatic calculations. Additionally, the non-adiabatic corrections developed here can be applied to other alkali metal measurements.

References

- [1] Antonio Pich. “The Standard Model of Electroweak Interactions”. In: *arXiv:0705.4264 [hep-ex, physics:hep-ph]* (May 2007). URL: <http://arxiv.org/abs/0705.4264> (visited on 05/17/2020).
- [2] Tilman Plehn. *Lectures on LHC physics*. eng. 2. ed. Lecture notes in physics 886. Cham: Springer, 2015. ISBN: 978-3-319-05941-9.
- [3] C. S. Wu et al. “Experimental Test of Parity Conservation in Beta Decay”. en. In: *Physical Review* 105.4 (Feb. 1957), pp. 1413–1415. ISSN: 0031-899X. DOI: [10.1103/PhysRev.105.1413](https://doi.org/10.1103/PhysRev.105.1413). URL: <https://link.aps.org/doi/10.1103/PhysRev.105.1413> (visited on 05/17/2020).
- [4] W. N. Cottingham and D. A. Greenwood. *An introduction to the standard model of particle physics*. 2nd ed. Cambridge ; New York: Cambridge University Press, 2007. ISBN: 978-0-521-85249-4.
- [5] Dominik Becker et al. “The P2 experiment: A future high-precision measurement of the weak mixing angle at low momentum transfer”. en. In: *The European Physical Journal A* 54.11 (Nov. 2018), p. 208. ISSN: 1434-6001, 1434-601X. DOI: [10.1140/epja/i2018-12611-6](https://doi.org/10.1140/epja/i2018-12611-6). URL: <http://link.springer.com/10.1140/epja/i2018-12611-6> (visited on 05/24/2020).
- [6] M. Tanabashi et al. “Review of Particle Physics”. en. In: *Physical Review D* 98.3 (Aug. 2018), p. 030001. ISSN: 2470-0010, 2470-0029. DOI: [10.1103/PhysRevD.98.030001](https://doi.org/10.1103/PhysRevD.98.030001). URL: <https://link.aps.org/doi/10.1103/PhysRevD.98.030001> (visited on 06/03/2020).
- [7] C. S. Wood. “Measurement of Parity Nonconservation and an Anapole Moment in Cesium”. In: *Science* 275.5307 (Mar. 1997), pp. 1759–1763. ISSN: 00368075, 10959203.

- DOI: [10.1126/science.275.5307.1759](https://doi.org/10.1126/science.275.5307.1759). URL: <https://www.sciencemag.org/lookup/doi/10.1126/science.275.5307.1759> (visited on 05/17/2020).
- [8] Carl Wieman and Andrei Derevianko. "Atomic parity violation and the standard model". In: *arXiv:1904.00281 [hep-ph, physics:physics]* (Mar. 2019). URL: <http://arxiv.org/abs/1904.00281> (visited on 05/17/2020).
- [9] M. S. Safronova and U. I. Safronova. "Critically evaluated theoretical energies, lifetimes, hyperfine constants, and multipole polarizabilities in Rb 87". en. In: *Physical Review A* 83.5 (May 2011), p. 052508. ISSN: 1050-2947, 1094-1622. DOI: [10.1103/PhysRevA.83.052508](https://doi.org/10.1103/PhysRevA.83.052508). URL: <https://link.aps.org/doi/10.1103/PhysRevA.83.052508> (visited on 06/06/2020).
- [10] David Park. *Introduction to the quantum theory*. English. Mineola, N.Y.: Dover Publications, 2005. ISBN: 978-0-486-44137-5.
- [11] R. F. Gutterres et al. "Determination of the 87 Rb 5 p state dipole matrix element and radiative lifetime from the photoassociation spectroscopy of the Rb 2 0 g - (P 3 / 2) long-range state". en. In: *Physical Review A* 66.2 (Aug. 2002), p. 024502. ISSN: 1050-2947, 1094-1622. DOI: [10.1103/PhysRevA.66.024502](https://doi.org/10.1103/PhysRevA.66.024502). URL: <https://link.aps.org/doi/10.1103/PhysRevA.66.024502> (visited on 06/30/2020).
- [12] A. Kreuter et al. "Experimental and theoretical study of the 3 d D 2 -level lifetimes of Ca + 40". en. In: *Physical Review A* 71.3 (Mar. 2005), p. 032504. ISSN: 1050-2947, 1094-1622. DOI: [10.1103/PhysRevA.71.032504](https://doi.org/10.1103/PhysRevA.71.032504). URL: <https://link.aps.org/doi/10.1103/PhysRevA.71.032504> (visited on 06/30/2020).
- [13] R. H. Leonard et al. "High-precision measurements of the Rb 87 D -line tune-out wavelength". en. In: *Physical Review A* 92.5 (Nov. 2015), p. 052501. ISSN: 1050-2947, 1094-1622. DOI: [10.1103/PhysRevA.92.052501](https://doi.org/10.1103/PhysRevA.92.052501). URL: <https://link.aps.org/doi/10.1103/PhysRevA.92.052501> (visited on 07/01/2020).

- [14] Adam Fallon and Charles Sackett. "Obtaining Atomic Matrix Elements from Vector Tune-Out Wavelengths Using Atom Interferometry". en. In: *Atoms* 4.2 (Mar. 2016), p. 12. ISSN: 2218-2004. DOI: [10.3390/atoms4020012](https://doi.org/10.3390/atoms4020012). URL: <http://www.mdpi.com/2218-2004/4/2/12> (visited on 05/18/2020).
- [15] A. Derevianko et al. "High-Precision Calculations of Dispersion Coefficients, Static Dipole Polarizabilities, and Atom-Wall Interaction Constants for Alkali-Metal Atoms". en. In: *Physical Review Letters* 82.18 (May 1999), pp. 3589–3592. ISSN: 0031-9007, 1079-7114. DOI: [10.1103/PhysRevLett.82.3589](https://doi.org/10.1103/PhysRevLett.82.3589). URL: <https://link.aps.org/doi/10.1103/PhysRevLett.82.3589> (visited on 06/24/2020).
- [16] Bindiya Arora, M. S. Safronova, and Charles W. Clark. "Determination of electric-dipole matrix elements in K and Rb from Stark shift measurements". en. In: *Physical Review A* 76.5 (Nov. 2007), p. 052516. ISSN: 1050-2947, 1094-1622. DOI: [10.1103/PhysRevA.76.052516](https://doi.org/10.1103/PhysRevA.76.052516). URL: <https://link.aps.org/doi/10.1103/PhysRevA.76.052516> (visited on 06/02/2020).
- [17] M. S. Safronova, W. R. Johnson, and A. Derevianko. "Relativistic many-body calculations of energy levels, hyperfine constants, electric-dipole matrix elements, and static polarizabilities for alkali-metal atoms". en. In: *Physical Review A* 60.6 (Dec. 1999), pp. 4476–4487. ISSN: 1050-2947, 1094-1622. DOI: [10.1103/PhysRevA.60.4476](https://doi.org/10.1103/PhysRevA.60.4476). URL: <https://link.aps.org/doi/10.1103/PhysRevA.60.4476> (visited on 06/02/2020).
- [18] Bindiya Arora, M. S. Safronova, and Charles W. Clark. "Tune-out wavelengths of alkali-metal atoms and their applications". en. In: *Physical Review A* 84.4 (Oct. 2011), p. 043401. ISSN: 1050-2947, 1094-1622. DOI: [10.1103/PhysRevA.84.043401](https://doi.org/10.1103/PhysRevA.84.043401). URL: <https://link.aps.org/doi/10.1103/PhysRevA.84.043401> (visited on 05/31/2020).
- [19] Thomas F. Gallagher. *Rydberg atoms*. Digitally printed 1st pbk. version. Cambridge monographs on atomic, molecular, and chemical physics 3. Cambridge ; New York: Cambridge University Press, 2005. ISBN: 978-0-521-02166-1.

- [20] M. Born and W. Heisenberg. “Über den Einfluss der Deformierbarkeit der Ionen auf optische und chemische Konstanten. I”. de. In: *Zeitschrift für Physik* 23.1 (Dec. 1924), pp. 388–410. ISSN: 1434-6001, 1434-601X. DOI: [10.1007/BF01327603](https://doi.org/10.1007/BF01327603). URL: <http://link.springer.com/10.1007/BF01327603> (visited on 07/16/2020).
- [21] Joseph E. Mayer and Maria Goeppert Mayer. “The Polarizabilities of Ions from Spectra”. en. In: *Physical Review* 43.8 (Apr. 1933), pp. 605–611. ISSN: 0031-899X. DOI: [10.1103/PhysRev.43.605](https://doi.org/10.1103/PhysRev.43.605). URL: <https://link.aps.org/doi/10.1103/PhysRev.43.605> (visited on 05/21/2020).
- [22] G. W. F. Drake and R. A. Swainson. “Expectation values of r^P for arbitrary hydrogenic states”. en. In: *Physical Review A* 42.3 (Aug. 1990), pp. 1123–1126. ISSN: 1050-2947, 1094-1622. DOI: [10.1103/PhysRevA.42.1123](https://doi.org/10.1103/PhysRevA.42.1123). URL: <https://link.aps.org/doi/10.1103/PhysRevA.42.1123> (visited on 05/21/2020).
- [23] Jianing Han et al. “Rb $n f$ quantum defects from millimeter-wave spectroscopy of cold Rb 85 Rydberg atoms”. en. In: *Physical Review A* 74.5 (Nov. 2006), p. 054502. ISSN: 1050-2947, 1094-1622. DOI: [10.1103/PhysRevA.74.054502](https://doi.org/10.1103/PhysRevA.74.054502). URL: <https://link.aps.org/doi/10.1103/PhysRevA.74.054502> (visited on 06/03/2020).
- [24] Jeonghun Lee, J. Nunkaew, and T. F. Gallagher. “Microwave spectroscopy of the cold rubidium $(n + 1) d_{5/2} \rightarrow n g$ and $n h$ transitions”. en. In: *Physical Review A* 94.2 (Aug. 2016), p. 022505. ISSN: 2469-9926, 2469-9934. DOI: [10.1103/PhysRevA.94.022505](https://doi.org/10.1103/PhysRevA.94.022505). URL: <https://link.aps.org/doi/10.1103/PhysRevA.94.022505> (visited on 05/25/2020).
- [25] S. J. Berl et al. “Core polarizability of rubidium using spectroscopy of the ng to nh , ni Rydberg transitions”. In: *arXiv:2004.08226 [physics]* (Apr. 2020). arXiv: 2004.08226. URL: <http://arxiv.org/abs/2004.08226> (visited on 06/03/2020).
- [26] J. H. Van Vleck and N. G. Whitelaw. “The Quantum Defect of Nonpenetrating Orbits, with Special Application to Al II”. en. In: *Physical Review* 44.7 (Oct. 1933), pp. 551–

569. ISSN: 0031-899X. DOI: [10.1103/PhysRev.44.551](https://doi.org/10.1103/PhysRev.44.551). URL: <https://link.aps.org/doi/10.1103/PhysRev.44.551> (visited on 05/22/2020).
- [27] Joseph Reader. "Spectrum and energy levels of singly ionized rubidium (Rb ii)". en. In: *Journal of the Optical Society of America* 65.3 (Mar. 1975), p. 286. ISSN: 0030-3941. DOI: [10.1364/JOSA.65.000286](https://doi.org/10.1364/JOSA.65.000286). URL: <https://www.osapublishing.org/abstract.cfm?URI=josa-65-3-286> (visited on 05/22/2020).
- [28] Hans Karlsson and Ulf Litzén. "Revised Ba I and Ba II Wavelengths and Energy Levels Derived by Fourier Transform Spectroscopy". In: *Physica Scripta* 60.4 (Oct. 1999). Publisher: IOP Publishing, pp. 321–328. DOI: [10.1238/physica.regular.060a00321](https://doi.org/10.1238/physica.regular.060a00321). URL: <https://doi.org/10.1238/physica.regular.060a00321>.

2 | Experimental systems and methods

It is important to critically design an efficient and functional system to achieve the goals set forth by the experimental objective. In this case, the objective is to obtain more precise results for core polarizability than from previous experiments. This reduction in the uncertainty of atom polarizability is useful for theoretical calculations and future experiments, as expressed in the introduction. To achieve this goal of reduced uncertainty, it is critical to determine sources of systematic uncertainty in the previous experiment of interest, referenced in Ref. [1]. The identified sources of systematic uncertainties are from background electric fields due to the high principal quantum number and the limit of the experimental apparatus to drive higher angular momentum state transitions, mitigated by the fact that d state energies are known.

In the work by Lee, *et al.* in Ref. [1], $(n + 1)d$ to ng and nh state energies are determined through microwave spectroscopy of $27 \leq n \leq 30$. As described in the introduction, the response of an atom to an external electric field is dependent upon atom polarizability, shown in Eqn. (1.10). Furthermore, atom polarizability scales as n^7 as shown in Table 1.2. Reducing sensitivity to external electric fields thereby improves the precision and reduces systematic uncertainty of spectroscopic measurements. To achieve this, using a lower principal quantum number is beneficial. For the purposes of this research, $n = 17 - 19$ provides the lowest n values for which the desired high angular momentum state transition frequencies remain experimentally accessible via microwave technology. When

comparing $n = 17 - 19$ to $n = 27 - 30$, there is an approximate factor of 25 reduction in sensitivity to electric fields, including background or stray fields.

Additionally, an increase in the angular momentum state corresponds to less core penetration effects, since the valence electron orbit is more circular and more hydrogenic. Core penetration and polarization effects are represented as an energy shift from hydrogen, corresponding to a reduction in quantum defect. This is introduced in Eqn. (1.14) and the quantum defect values are shown Table 1.3. To isolate the core polarization effects from the core penetration effects, higher angular momentum states are desired. In this research, relative spectroscopic measurements of $\ell = 3 \rightarrow 4 - 6$ are used, whereas in the previous experiment, absolute measurements of $\ell = 2 \rightarrow 4, 5$ are conducted using prior knowledge of the $\ell = 2$ quantum defect values. This experimental difference is mainly due to accessibility of angular momentum states with microwave technology, rather than an advantage.

Experimental improvements have been sufficiently identified in this critical design phase, however it is equally important to identify potential issues, flaws, and sources of uncertainty for the proposed experiment. Unfortunately, with the experimental choice to mitigate energy shifts due to background electric and magnetic fields by selecting $n = 17 - 19$, the ability to drive $nd \rightarrow nf$ is not present with the given terahertz-scale energy level separations. Shorter lifetimes of the atoms in the Rydberg states equate to more strict experiment timings. Smaller dipole moments correspond to smaller transition amplitudes and thus can contribute a lower *signal to noise ratio (SNR)*, which can be compensated for by an increased microwave drive amplitude. Large energy spacing between adjacent n states requires a highly tunable laser. Fine structure is measurable and plays a role in determining the center of gravity transition frequency, which will be discussed in further detail in Chapter 3. Additionally, lower n requires a higher ionization field making experiments more difficult given the higher fields required to strip the valence electron from the ionic core. An upper limit of applied voltage is present due to the high voltage limitations of the

field pulse electronics and arcing between the electric field plates in the vacuum system.

In the following sections within this chapter, the vacuum system, dye laser systems, timing systems, microwave/rf systems, field ionization, and data acquisition systems are discussed in more detail. To provide a brief overview, this experiment is conducted using a Rb oven to create a hot rubidium vapor beam. Two laser pulses in quick succession are focused at the center of the vacuum chamber to drive $5s$ ground state to nf Rydberg state transitions. Following these laser pulses, a microwave pulse or combination of microwave and RF pulses are applied to drive the higher angular momentum state transitions. The atoms are then ionized using state-selective field ionization techniques and either ions or electrons are detected, depending upon the sign of the ionizing potential, on a spatially integrating *multi-channel plate (MCP)*. The current on the MCP is converted to a voltage reading and sent to a suite of analysis equipment.

2.1 Vacuum system

The experiment is performed under vacuum. The vacuum system consists of a vacuum chamber, mechanical roughing pump, and diffusion pump. An illustration of this system is shown in Figure 2.1. What is denoted as the *vacuum chamber* is the region where the scientific experiments take place, separate from the vacuum pumping systems. The experimental region of the vacuum chamber consists of a rubidium oven, quartz glass windows to allow for laser light to pass through, multiple electrical feedthrough connectors on vacuum flanges to allow for electrical connections within the chamber, a hot-filament ionization gauge to measure vacuum pressure, and a rubidium oven with electrical connections to create a thermal atom beam.

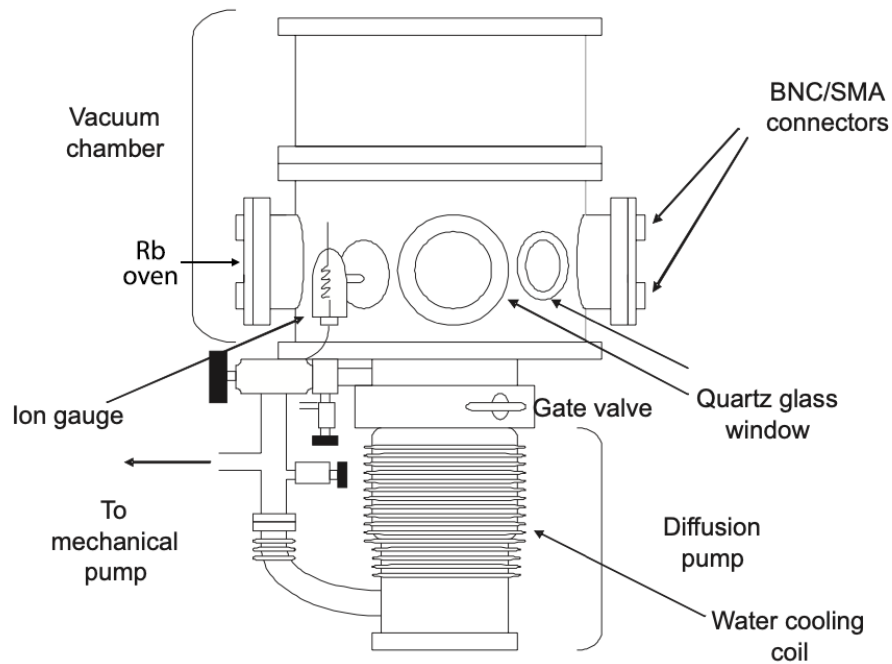


FIGURE 2.1: Illustration of the vacuum system. This image from Ref. [2] has been utilized and adapted since the vacuum systems in both experiments are similar. The portion of the vacuum system labeled "vacuum chamber" is the area where scientific experiments are conducted. This is located above the diffusion pump. The vacuum chamber includes quartz glass windows for laser light to enter the chamber, electrical feedthrough connections on vacuum flanges to allow for electrical connections within the chamber, a hot-filament ionization gauge to measure pressure, and a rubidium oven with electrical connections to create a thermal atom beam. Below the vacuum chamber, there is a gate valve to separate the diffusion pump. The intricacies of the diffusion pump are discussed in more detail in the text and illustrated in Figure 2.3. Following the diffusion pump, there is a mechanical vane roughing forepump separated by another valve.

2.1.1 Pump method

As shown in the vacuum system diagram (Figure 2.1), a diffusion pump is connected directly to the vacuum chamber, followed by a mechanical roughing pump. The *mechanical roughing pump* is capable of reaching pressures of approximately 10^{-3} torr to reach a sufficient vacuum before the diffusion pump can be safely turned on. The roughing pump is a rotary vane design. A basic *rotary vane pump* consists of an outer housing, an eccentric rotor, vanes that move radially with the rotor under spring tension, and inlet and outlet valves. This design relies on oil with the outlet valve oil-sealed and closed until the gases are compressed by the rotor operation to atmospheric pressure where the gas is expelled and the second vane seals the opposite end of the rotor. A diagram depicting the operation of this is shown in Fig. 2.2.

Upon reaching approximately 10^{-3} torr, the *diffusion vacuum pump* is turned on. A schematic of the generic operation of the diffusion pump is shown in Fig 2.3. The diffusion pump used in this experiment is a Varian VHS6. Pump oil is heated using a 208 V heater assembly below the diffusion pump; these are a set of heater coils connected directly to the facilities supplied 208 V single-phase AC power and turned on/off by a circuit breaker on the wall. Santovac diffusion pump oil is vaporized and a jet of oil molecules are sent upwards through the center stack of metallic surfaces. The oil molecules are then deflected by the stack geometry disrupting laminar flow and sent downwards where oil and gas molecules collide. The oil condenses onto the surfaces of the stack, and gas molecules are driven to the bottom of the pump. To facilitate condensation, coolant is flowed through coolant lines around the diffusion pump assembly; in this experiment, a continuous flow of tap water is used. This process results in a pressure gradient between the top and bottom of the diffusion pump where the forepump removes the trapped air from the bottom of the diffusion pump. Oil is continuously being boiled so long as the heater is active, making vacuum pumping continuous with this design. A major drawback of this vacuum pump

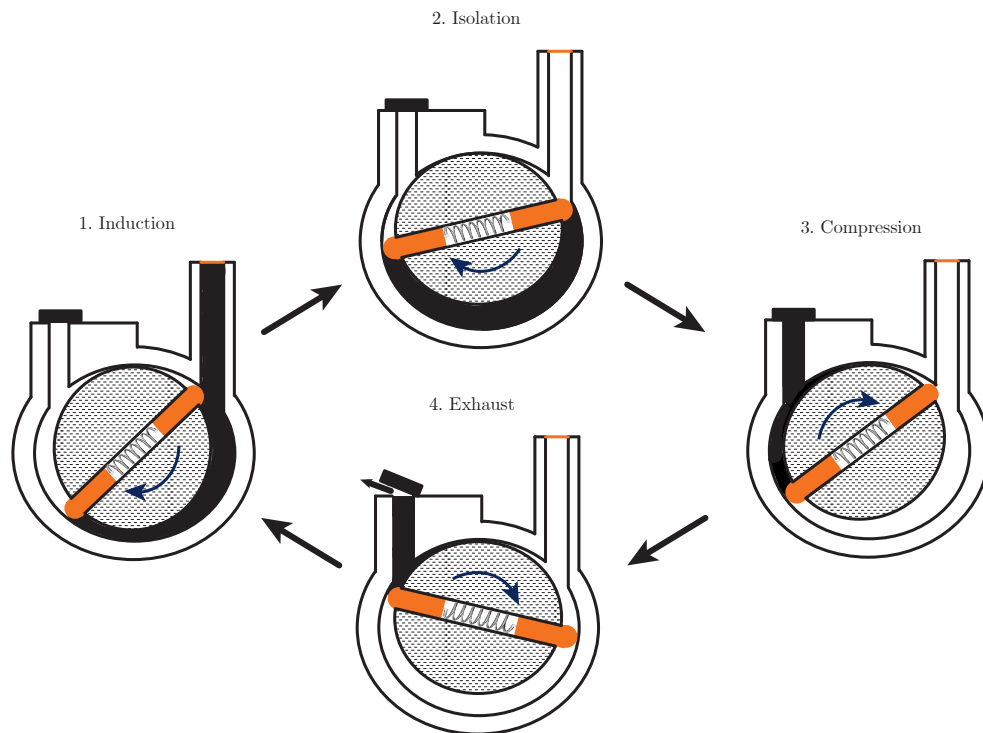


FIGURE 2.2: Illustration of the operation of a rotary vane vacuum pump. The components of a rotary vane pump usually consist of an outer housing, an eccentric rotor, vanes that move radially with the rotor under spring tension, and inlet and outlet valves. This design relies on oil with the outlet valve oil-sealed and closed until gases are compressed by rotor operation to atmospheric pressure where the gas is expelled and the second vane seals the opposite end of the rotor.

design is the unavoidable use of vacuum oil, coating surfaces within the vacuum system with oil.

Vacuum pressures are measured in two locations: at the bottom of the diffusion pump before the forepump and in the vacuum chamber (shown in Figure 2.1). The vacuum pressure gauge between the diffusion pump and forepump is a *thermocouple gauge*, typically rated for pressures between 10^{-3} and 760 torr with approximately 15% accuracy. Within the vacuum chamber, a *hot-filament ionization gauge* is used and vacuum pressure is reported with a *Granville Phillips 330 Hot Cathode Ion Gauge Controller*. Upon initially pulling a vacuum and pumping down the chamber, pressures will quickly fall to and plateau at approximately 5×10^{-6} torr. There are many sources of contaminants that affect vacuum performance and applying heat accelerates outgassing. When the chamber is heated by wrapping heater tape around the chamber and left to sit for an extended period of time, pressures can fall as low as 5×10^{-8} torr after the chamber is left to cool. The outgassing process explains the higher pressures observed during the heating process and the lower pressure after allowing the chamber to cool. However, vacuum baking is not always necessary since under normal operation, 3×10^{-7} torr is usually observed and found to be sufficient for data acquisition. This pressure is achieved after a few days of letting the chamber sit with the diffusion and roughing pumps on. When the rubidium oven is set to a higher temperature for diagnostic purposes, the pressure in the chamber can rise as high as 1×10^{-6} torr.

2.1.2 Experimental region

The portion of Figure 2.1 that is denoted as the "vacuum chamber" is where the scientific equipment that makes scientific measurements possible are located. Figure 2.4 shows these elements and their geometry more clearly, with the main components within this vacuum system being:

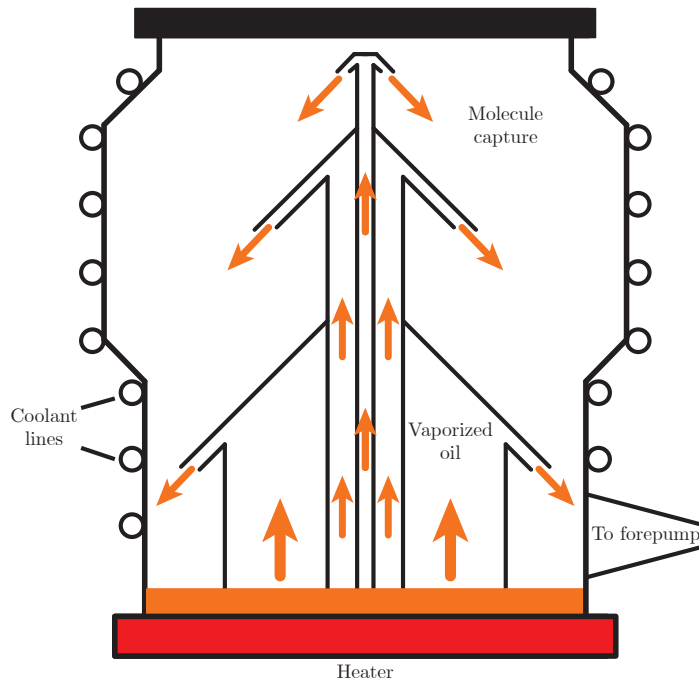


FIGURE 2.3: Illustration of the fundamental operation of a diffusion pump. Pump oil is heated using a heater assembly below the diffusion pump. Diffusion pump oil is vaporized and a jet of oil molecules are sent upwards through the center stack of metallic surfaces. Oil molecules are then deflected by the stack geometry disrupting laminar flow and sent downwards where oil and gas molecules collide. Oil condenses onto the surfaces of the stack, and gas molecules are driven to the bottom of the pump. To facilitate condensation, coolant is flowed through coolant lines around the diffusion pump assembly. A pressure gradient is present between the top and bottom of the vacuum pump where the forepump removes the trapped gases from the bottom of the diffusion pump. This process is continuous with oil continuously being boiled so long as the heater is active.

- (a) Rubidium oven where the hot rubidium vapor is created and a beam is directed towards the center of the vacuum chamber.
- (b) Field ionization plates where Rydberg atoms are ionized by stripping the valence electron from the Rb ionic core.
- (c) Laser beams focused at the center of the vacuum chamber, defining this as the experimental region at the center of field ionization plates and aligned with the Rb atom beam.
- (d) Multi-channel plate (MCP) in a spatially integrating configuration to detect an ionization signal, configured either to detect electrons or ions depending upon the polarity of the field ionization plates.
- (e) Microwave horn facing the atoms to drive ℓ state transitions.

In the following sections of this chapter, each of these components are discussed in more detail.

2.2 Atom beam

The heated oven allows for a rubidium *thermal beam*. Rubidium is contained within a stainless steel tube that is heated by flowing current through the tube. The tube design used in this experiment to accommodate the mounting structure is shown in Figure 2.5. This tube design was adopted due to readily accessible materials. The design can be altered so long as the chosen oven design mounts to the existing structure and an electrical connection is made for current to flow through the metal thereby heating and vaporizing the rubidium contained within the tube.

The oven assembly is home-built and fabricated using the following process:

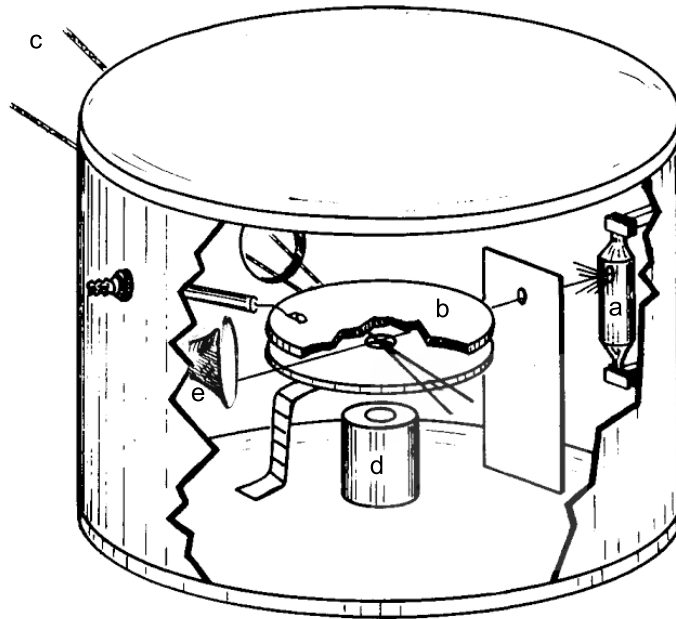


FIGURE 2.4: Vacuum science chamber illustration with (a) rubidium oven creating a hot thermal atom beam directed toward the center of the vacuum chamber and collimated by a hole in a plate. At the center of the vacuum chamber and center of the (b) field ionization plates, (c) two laser beams are focused. This is the region where the atoms are interacting with the lasers and microwaves directed at the center of the chamber to drive atomic transitions with (e) microwave horns. A (d) multi-channel plate (MCP) in a spatially-integrating configuration is used to detect ions or electrons depending upon the polarity of the field ionization plates. This figure has been adapted from Ref. [3].

-
- Procure a stainless steel tube approximately 7.5 in in length and 0.75 in in diameter with a wall thickness of approximately 1/32 in. Notably, the length of the tube is longer than shown in Fig. 2.5. Later in the assembly, the ends of the tube will eventually be crimped and folded.
 - Clean the inside and outside of the tube thoroughly with soap and water to remove contaminants, followed by an acetone wash to prepare for the installation into the vacuum chamber.
 - Pinch/crimp one end with a mechanical press and fold over once for structural integrity and to make a better seal.
 - Drop a glass Rb ampule into the tube.
 - Pinch/crimp the other end with a mechanical press and fold over once for structural integrity and to form a seal.
 - Use a Dremel with a cutting tool attachment to cut the four mounting screw holes in the top and bottom sides of the assembly. A drill press can instead be used for this step; however, a sturdy mounting mechanism is necessary to ensure that the tube and Rb ampule are not accidentally crushed and that vibrations from the drill do not break the ampule.
 - On a drill press, use approximately a 0.5 mm drill bit to drill a hole in the tube, perpendicular to the now flat crimped ends and approximately at the height of the atoms within the vacuum chamber once installed.
 - Clean the outside of the tube once again with soap and water, followed by an acetone wash, to remove contaminants before installing into vacuum. Prevent water and acetone from entering the hole.
 - Install the fabricated oven into the vacuum chamber mounting bracket.

- User pliers to crush the stainless steel tube and break the Rb ampule.
- When the glass is heard shattering, quickly reinstall, seal flange, and turn on roughing pump to return the system to vacuum. It is crucial to have this system under vacuum as quickly as possible to minimize the oxidation of rubidium.

A hot rubidium beam is achieved once the current passing through the oven is set to an appropriate setting, corresponding to a temperature to reach a desired vapor pressure of the Rb, generally above 80°C. The vapor subsequently sprays out of the drilled hole in a conical fashion and is roughly collimated by a hole drilled in a plate following the initial atom spray that is aligned with the height of the atoms. The resistance of the stainless steel tube is $R \ll 1 \Omega$, so the voltage across the ends of the tube should be relatively small. A Variac variable transformer is plugged directly into the wall to allow for current adjustment, then a voltage step-down transformer is employed to attain high current and low voltage across the tube to allow the oven to heat. Good experimental operation is achieved at an oven current of 15A. However, a maximum of 30A is possible for flooding the chamber with rubidium for diagnostic testing. An even higher current is possible; however, with the higher current, there is a potential risk of heating the components beyond their breaking point. Additionally, vacuum performance is degraded when flooding the chamber with rubidium, with a pressure of approximately 1×10^{-6} torr, experimentally too high for data acquisition.

2.3 Dye laser system

Rubidium atoms begin in their ground state of 5s. To excite the Rb atoms to the desired $n = 17 - 19$ range of Rydberg states, two pulsed Nd:YAG lasers use either second or third harmonics to pump two home-built dye lasers. An illustration of the atomic transitions are shown Figure 2.6. Rubidium atoms are first excited to the 6p state using a laser pulse.

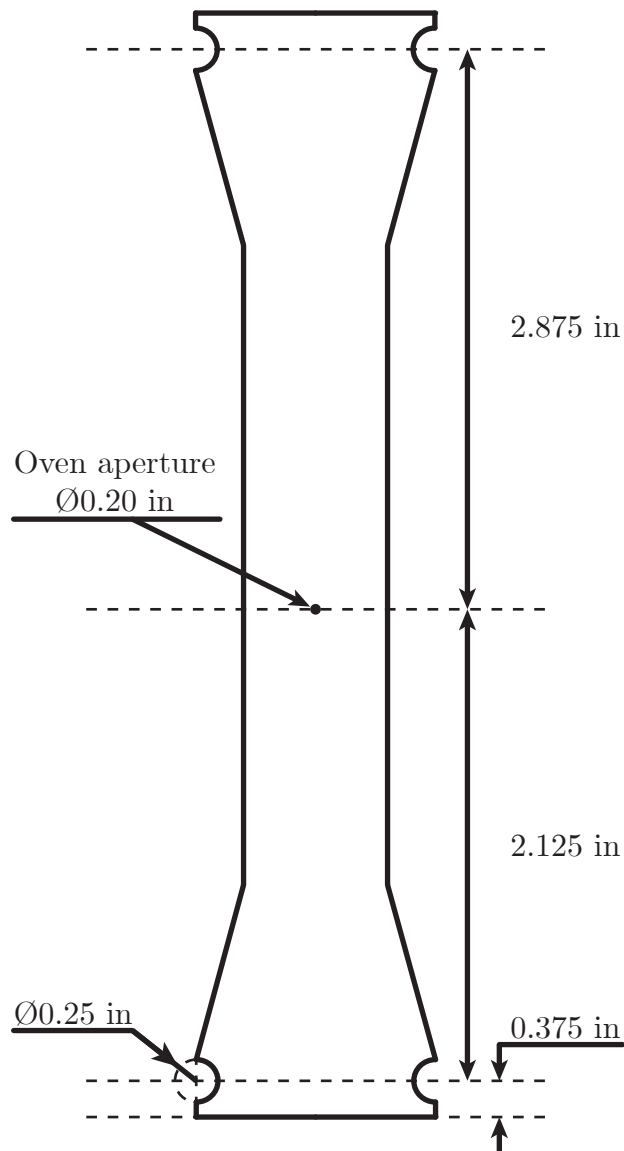


FIGURE 2.5: Rubidium oven schematic to scale. A stainless steel tube with a wall thickness of approximately $1/32 \text{ in}$ is used. Both ends are crimped, folded, and crimped again, with the screw holes drilled for mounting purposes, a Rb ampule contained within, and a hole approximately 0.5 mm in diameter drilled for a vaporized atom beam to be expelled.

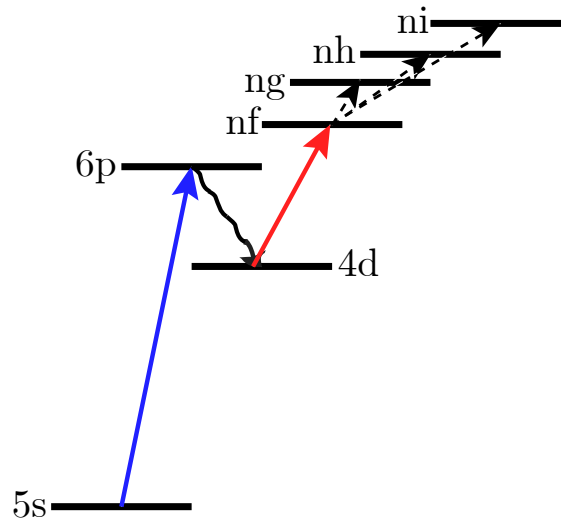


FIGURE 2.6: Atomic states used in this experiment. Rubidium atoms begin in the ground state of $5s$ and are excited to the $6p$ state using a laser pulse. Following this initial laser pulse, sufficient time is allowed for the atoms in this excited state to spontaneously decay to the $4d$ state. Once the atoms are in the $4d$ state, another laser pulse is applied to drive a transition to a nf Rydberg state where $n = 17 - 19$ for this experiment. Subsequent microwave pulses follow to drive higher angular momentum state transitions later in the experiment, denoted here as dotted lines. Fine structure splitting is purposely neglected in this illustration. The $5s_{1/2}$ ground state transition to either $6p_{1/2}$ or $6p_{3/2}$ can be resolved and selected experimentally with the wavelengths for these transitions shown in Table 2.1.

Following the $5s \rightarrow 6p$ laser pulse, a delay is introduced before switching on the $4d \rightarrow nf$ dye laser pulse. This delay is introduced to wait for the time where spontaneous emission allows the Rb atoms to fall to the $4d$ state from the $6p$ state. The lifetime of the $6p$ state is 99.3 ns [4]. Another decay path could be back to the ground state. Per the transition probabilities presented in Ref. [4], approximately 33% of the atoms will decay to the $4d$ state and approximately 66% decay to the ground state. The lifetime of the $4d$ state is 85.0 ns [4]. Knowing that the spontaneous decay rate is increasing the number of atoms to the $4d$ state and the lifetime is decreasing the number of atoms in the $4d$ state, it is experimentally found that a 250 ns delay results in the maximum number of atoms detected in the desired nf states. Thus, the experimental systems must operate with strict timings. Atoms must remain in the experiment interaction region, appropriate timings selected between laser pulses to allow for the spontaneous decay of $6p$ to $4d$, pulse delay and duration of microwaves for higher angular momentum state transitions, and data acquisition timings. Experimental timings are explained in more detail in the *Experiment timing* section later in this chapter.

Fine structure is purposely neglected in this illustration, although the $5s_{1/2}$ ground state transition to either $6p_{1/2}$ or $6p_{3/2}$ can be resolved and selected experimentally. The wavelengths for these transitions are shown in Table 2.1. By exciting to the $6p_{1/2}$ state, the atoms are allowed to decay to the $4d_{3/2}$ state before the second laser pulse excites the atoms to the $nf_{5/2}$ state. Alternatively, tuning the first laser on resonance with the $6p_{3/2}$ state, decay to the $4d_{3/2}$ and $4d_{5/2}$ states are possible. The next laser pulse drives the atoms to both $nf_{5/2}$ and $nf_{7/2}$ with the inability to directly resolve fine structure for higher- ℓ states due to transform broadening of the laser pulse.

Dye lasers are chosen for their excellent wavelength tuning abilities. Dye lasers rely on an organic dye in a solvent to serve as the lasing medium where dye molecules fluoresce in the presence of a pumping light. The pump light is chosen to excite the dye molecules to a state where stimulated emission is possible. Organic dyes have a large absorption range

making the use of an external pump-laser relatively simple [5]. Both laser systems have a large dye solution reservoir to allow for continued operation since the organic dyes will eventually decompose and lose their fluorescence properties [6]. Phosphorescence causes the organic dye to become opaque; therefore, it is beneficial to force the dye to move at a high velocity to allow for the excitation of fresh dye molecules. For this experiment, the dye flows through a spectrometer-grade quartz cuvette with a metal insert glued in with silicone sealant to reduce the cross-sectional area and increase the flow rate where the dye solution interacts with the pump and final lasing light. Light is fed back allowing for multiple passes so maximal output light power can be achieved. To tune the wavelength of the output laser light, multiple configurations can be used to control the feedback light sent back through the dye. These will be discussed more in subsections that follow. Two different configurations are used for each laser system.

2.3.1 $5s \rightarrow 6p$ laser setup

The first laser pulse is chosen to excite the Rb atoms from the $5s_{1/2}$ ground state to either one of the $6p_{1/2}$ or $6p_{3/2}$ excited states. The laser wavelengths required to optically drive this transition are shown in Table 2.1. Stilbene 420 dye is chosen due to maximal absorption at 353 nm with a wide absorptivity range and wide lasing wavelength, around 421 nm. The datasheet for Stilbene 420 is shown in Appendix H.1 and provides lasing wavelengths when pumped by the third harmonic of a Nd:YAG laser. Here, a Quanta-Ray DCR-2A Nd:YAG laser at a repetition rate of 20 Hz is used to optically pump a home-built dye laser with the Stilbene 420 dye solution. The Nd:YAG operates at 1064 nm with the third harmonic being approximately 355 nm. For a target maximal dye laser power at a wavelength of 421 nm, a 5×10^{-4} molar dye solution with an ethanol solvent is used. The laser cavity was initially in a Littrow configuration due to its simplicity. However, lasing was difficult to achieve with this configuration, therefore a change to the Littman-Metcalf configuration was implemented. Both configurations are illustrated in Fig. 2.7. The Littman-Metcalf

Transition	Wavelength (nm)
$5s_{1/2} \rightarrow 6p_{3/2}$	420.2 nm
$5s_{1/2} \rightarrow 6p_{1/2}$	421.5 nm

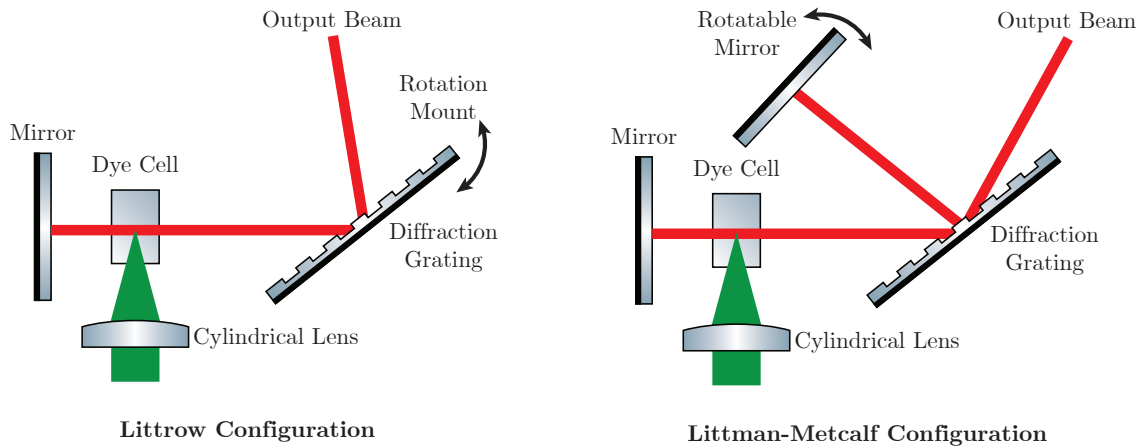
TABLE 2.1: $5s$ to $6p$ transition wavelengths per Ref. [7].

FIGURE 2.7: Littrow and Littman-Metcalf laser configurations. Initially, a Littrow laser configuration was chosen for this laser system due to its simplicity. However, the configuration was changed to a Littman-Metcalf design to offer laser tuning by rotating the mirror without the output beam direction changing. Additionally, laser feedback is improved with two passes across the diffraction grating.

configuration offers a couple of notable advantages over the Littrow configuration when forming a laser cavity. The direction of the output beam remains fixed since the mirror rotates instead of the diffraction grating feeding back to the laser. This is preferable since tuning the laser does not affect the direction of the output beam. Additionally, the output laser light tends to have a smaller linewidth since wavelength-dependent diffraction occurs twice per round trip of the light feeding back to the lasing media, instead of once in the Littrow configuration.

The duration of the laser pulse is approximately 20 ns, set by laser cavity lifetime; thus the pulse-broadened linewidth of the laser is minimally 50 MHz. The p -state fine structure can therefore be optically resolved given the 1.3 nm energy separation between the $6p_{1/2}$ or

Laser Wavelength	Dye	Pump Wavelength	Dye Concentration	Solvent
420 nm	Stilbene 420	355 nm	5.0×10^{-4} M (0.28 g/L)	Ethanol
722 nm	LDS 722	532 nm	2.5×10^{-4} M (0.09g/L)	Methanol

TABLE 2.2: To achieve a lasing wavelength of approximately 420 nm for the $5s \rightarrow 6p$ transition, Stilbene 420 dye is selected. This is pumped with the third harmonic of an Nd:YAG at 355 nm. For the $4d \rightarrow nf$ transition, LDS 722 dye is selected and pumped by the second harmonic of an Nd:YAG at 532 nm.

$6p_{3/2}$ excited states from the $5s_{1/2}$ ground state. Rotating the mirror in the Littman-Metcalf configuration allows for tuning between these wavelengths. The $5s_{1/2} \rightarrow 6p_{1/2}$ transition is chosen for this experiment since resolution of fine structure at the higher n and ℓ states becomes more difficult to resolve due to the nf state fine structure energy splitting being less than the laser linewidth. By exciting to the $6p_{1/2}$ state, it is guaranteed that only the $4_{3/2}$, $nf_{5/2}$, $ng_{7/2}$, $nh_{9/2}$, and $ni_{11/2}$ states are populated. This removes the ambiguity resulting from an experimentally unresolved ng fine structure that would accompany the use of $6p_{3/2}$. Tuning to the higher j -state is still important and designed for in this dye laser system since it is important to compare the fine structure energy level splittings of rubidium to hydrogen to verify that the core polarization model assumptions can still be used. Analysis of fine structure splittings are discussed more in Chapter 3.

2.3.2 $4d \rightarrow nf$ laser setup

A similar setup to the $5s \rightarrow 6p$ is employed for the $4d \rightarrow nf$ laser system. The second harmonic of a Continuum Surelite SLI-20 Nd:YAG pumps another home-built dye laser cavity. In this case, a LDS 722 dye solution with a molar concentration of 2.5×10^{-4} M in a methanol solvent is used. When pumped with the 532 nm second harmonic of the Nd:YAG, the output wavelength can be tuned from approximately 705 to 725 nm. The datasheet for LDS 722 can be found in Appendix H.2. This dye laser cavity is in a single beam expanding prism configuration. An illustration of this system is shown in Figure 2.8.

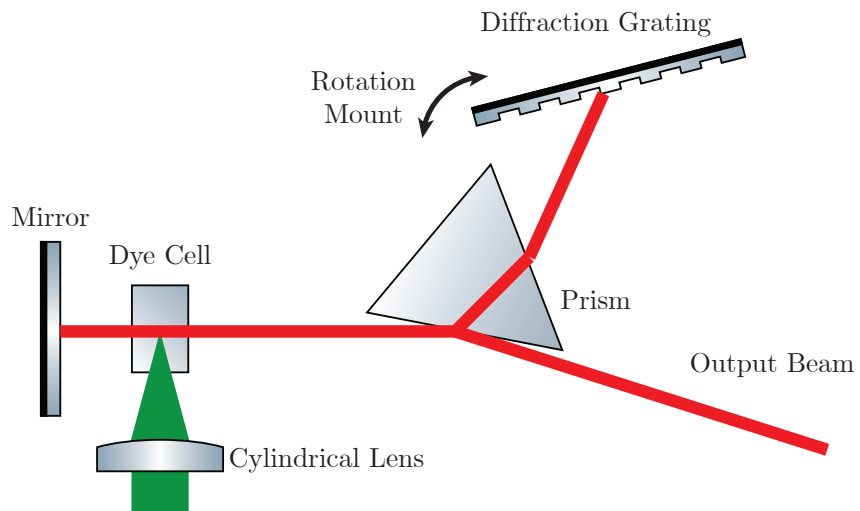


FIGURE 2.8: Dye laser cavity configuration with a single beam expanding prism to drive the $4d \rightarrow nf$ transition. 532 nm pump light is incident on a dye cell containing a solution of LDS 722 in a methanol solvent. The output beam comes from a grazing incidence reflection from the prism, which then gives an expanded beam going through the prism to the grating. The grating is rotatable allowing for laser wavelength tuning, which is fed back to the dye cell.

Transition from $4d \rightarrow nf$	Measured Vacuum Wavelength (nm)	Theoretical Vacuum Wavelength (nm)
$n = 15$	721.7	722.2
$n = 16$	719.4	719.1
$n = 17$	716.5	716.6
$n = 18$	714.6	714.5
$n = 19$	712.8	712.7
$n = 20$	711.4	711.2

TABLE 2.3: Measured laser wavelengths for the $4d_{3/2} \rightarrow nf_{5/2}$ transitions for $n = 15 - 20$. These measured are performed with a monochromator calibrated using Rb $5s_{1/2} \rightarrow 6p_{3/2} = 420.2$ nm transition per Ref. [8]. The purpose of using the monochromator in this system is to provide a tool to differentiate between the different n states. The measured wavelength is correlated to a measured rotation of the diffraction grating mount to make finding atomic resonances easily repeatable.

Using a Heath Company *monochromator* calibrated to the $5s_{1/2} \rightarrow 6p_{3/2} = 420.2$ nm transition per Ref. [8], atomic resonances for the $4d \rightarrow nf$ states are determined. The laser wavelength for $n = 15 - 20$ are shown in Table 2.3. Although the monochromator is calibrated, it is not intended here for precise nor accurate measurements. The monochromator instead acts as a tool to correlate diffraction grating mount rotation with atomic transitions. This therefore makes finding atomic resonances easier and more repeatable.

Outputs of the two laser systems are each fed into their own respective beam expanders where the laser beam is focused at the center of the vacuum chamber with a laser path distance of approximately 2 meters. For diagnostic purposes and timing calibration, laser pulses are monitored using a Thorlabs DET025A high-speed, free space, *photodiode detector*. The bandwidth of this detector is specified to be 2 GHz with rise and fall times on the order of 150 ps. Laser pulse durations are observed to be on the order of the expected 20 ns and detection is used to ensure that the two laser pulses are separated by the 250 ns prescribed earlier.

n	$f \rightarrow g$ (MHz)	$f \rightarrow h$ (MHz)	$f \rightarrow i$ (MHz)
15	24115	29065	30618
16	19867	23946	25226
17	16562	19962	21029
18	13950	16815	17714
19	11860	14296	15060
20	10168	12256	12911

TABLE 2.4: Calculated microwave transition intervals using previous experimental results. Transition frequencies for $f \rightarrow g$, $f \rightarrow h$, and $f \rightarrow i$ are shown for $n = 15 - 20$. These are calculated using previous experimental measurements from Ref. [1].

2.4 Microwave and rf systems

The goal of this work is to measure the energy spacing between high- ℓ states of Rydberg atoms. Precision spectroscopy measurements between the excited Rydberg atoms provide the ability to determine core polarizability, as described in the *Introduction*. For these higher- ℓ states, the transition frequencies are calculated for various n values of interest based on the previous core polarizability experimental results, and the calculated quantum defects for the f , g , h , and i states. The calculated transition intervals for $n = 15 - 20$ $f \rightarrow g$, $f \rightarrow h$, and $f \rightarrow i$ are shown in Table 2.4; microwave frequencies range from approximately 10 GHz to 30 GHz. This table of calculated transition frequencies provides a region for which to start searching for the atomic transition frequencies experimentally. It is evident that these frequencies fall in the microwave frequency range so an appropriate microwave source needs to be used to probe these ℓ states. This section details the use of microwave synthesizers and microwave signal transmission. Additionally, a 1 GHz rf source is applied to help drive the $f \rightarrow i$ transition. The particular details of how the measurements are conducted and the physics of the processes are reserved for discussion in the next chapter.

2.4.1 Synthesizers

Microwaves are produced using an Agilent 83622B synthesized swept-signal generator; this particular model is capable of outputting microwaves up to 20 GHz. Additionally, this synthesizer features externally controlled *pulse modulation* with a pulse generated by a Berkeley Nucleonics Corporation Model 8010 Pulse Generator. Typical pulses have a duration of 1 μs to provide sufficient time for transitions to be driven to the desired state. Per the specifications of the Agilent 83622B, the externally controlled pulse modulation has a minimum pulse duration of 1 μs . A longer pulse duration is programmable with the existing equipment, however a shorter pulse duration would require an external microwave switch following the synthesizer.

A single microwave photon carries only one unit of angular momentum. The $f \rightarrow g$ transition is characterized as a *single-photon transition* whereby one photon is absorbed by the atom. To drive this transition, the microwave frequency equates to the energy difference between the f and g states. To reach the higher- ℓ states, multi-photon transitions are used. The $f \rightarrow h$ transition is a two-photon transition where the microwave frequency is set to one half of the $f \rightarrow h$ transition frequency. For the $f \rightarrow i$ transition, the rf signal is pulsed on at the same time as the microwaves with the rf frequency applied corresponding to the the detuned h -state to i -state transition frequency. The microwave frequency is set to one half of the f -state to detuned h -state transition frequency for this multi-photon process. The rf field is produced by coupling a HP 8673C Signal Generator synthesizer to one of the electric field plates. This synthesizer also has externally controlled pulse modulation capabilities.

2.4.2 Microwave signal transmission

The microwave pulses are transmitted from the Agilent 83622B synthesizer through an SMA cable to a SMA electrical feedthroughs on the vacuum system (depicted in Figure

Waveguide Name	Recommended Frequency (GHz)	Cutoff Frequency (Lowest Order Mode)	Cutoff Frequency (Next Mode)	Dimensions (in)
WR90	8.20 to 12.40 GHz	6.557 GHz	13.114 GHz	0.9 x 0.4 in
WR75	10.00 to 15 GHz	7.869 GHz	15.737 GHz	0.75 x 0.375 in
WR62	12.40 to 18 GHz	9.488 GHz	18.976 GHz	0.622 x 0.311 in
WR51	15.00 to 22 GHz	11.572 GHz	23.143 GHz	0.51 x 0.255 in

TABLE 2.5: Waveguide name and characteristics for WR90, WR75, WR62, and WR51. Two waveguide types and microwave horns are used. Based on cutoff frequencies, WR90 and WR62 are used to provide microwave frequency transmission between approximately 6.6 GHz and 19 GHz.

2.1). The SMA cables selected for duty in this experiment are rated from DC to 26 GHz. A vacuum-compatible SMA cable is connected to the other end of the SMA connector feedthrough. The other end of this SMA cable connects to a Pasternack right angle waveguide adapter, and finally a *microwave horn antenna* directs the microwaves at the atoms inside of vacuum chamber. Placing the microwave horn antenna inside of the vacuum system minimizes microwave scattering [9]. Two different types of waveguides are used to cover the broad range of microwave frequencies needed for this experiment, WR90 and WR62. The specifications for these and other waveguides in these microwave bands are shown in Table 2.5. The use of WR90 and WR62 effectively provides frequency transmission between 6.6 GHz and 19 GHz. Both of these waveguide and horn antennas are present in the chamber and connected via separate SMA vacuum feedthroughs. To switch between the two types of the waveguide and horn antennas in the vacuum chamber, the SMA cable is manually switched between the two SMA vacuum feedthroughs. Only one waveguide is used for a particular experimental data set.

Microwave power is adjusted using the built-in attenuation of the synthesizer and optionally precision attenuators rated for DC to 18 GHz operation. These fixed attenuators are placed at the output of the synthesizer when attenuation beyond the -20 dBm limit of the synthesizer is required. It is difficult to estimate the microwave power directly at

the location of the atoms because there are various losses with each electrical connector and waveguide adapter; additionally, the electric field plates may contribute to scattering of microwaves. For a single photon transition, an electric field of only a few hundred $\mu\text{W}/\text{cm}$ can drive the $nf \rightarrow ng$ transition. Typically, the output power of the microwave synthesizer is set to -20 dBm. Multi-photon transitions rely on varying the microwave power for the measurements, with the microwave power varied between the -20 dB and $+17$ dBm synthesizer limits.

2.4.3 Rf signal application

RF is applied through a SMA feedthrough connector on the vacuum chamber. Similar to the microwave setup, a vacuum compatible SMA cable is attached to the other end of the feedthrough connector. However, the other end of the SMA cable is stripped and the coaxial conductor is attached directly to the electric field plate that does not receive the high voltage field ionization pulse. To avoid capacitive coupling of the high voltage pulse to the rf source across the electric field pulse, a bias tee is used to couple the ac signal generated by the HP 8673C Signal Generator synthesizer to ground, with a wire connecting the dc input to the vacuum chamber. Figure 2.9 shows the bias tee circuit implemented here.

RF power is adjusted using the built-in attenuator of rf generator. Unfortunately, due to poor impedance-matching with the electric field plate, estimation of the power of the rf signal at the atoms is more difficult with this setup when compared to the microwave case. Knowing the absolute power of the rf at the atoms is not necessary, so long as power at the atoms scales with the recorded synthesizer power. Although dependent on the detuning from the atomic resonance, the rf power required to drive these multi-photon transitions is greater than in the single-photon case. Typically the rf power output of the synthesizer is varied between 5 dBm and 13 dBm.

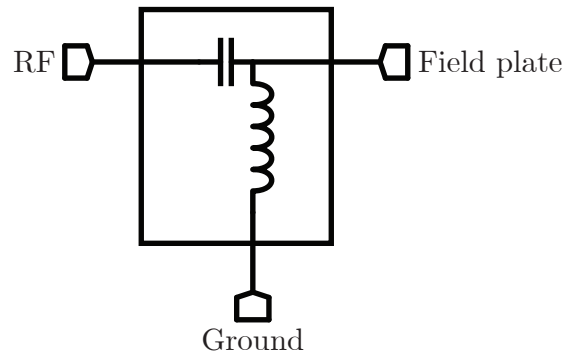


FIGURE 2.9: Bias tee circuit diagram. For the desired configuration, the rf synthesizer should not be connected directly to one of the electric field plates due to the voltage spike induced by the other field plate during the field ionization pulse. Therefore, a bias tee is used to protect the rf synthesizer with the synthesizer connected to the ac input and a ground wire connected to the dc input. Knowing the capacitor value and the voltage spike on the field plates, rf is coupled to the field plate while protecting the rf synthesizer.

For both microwaves and RF, a Narda 4503A crystal detector is used to monitor the pulse timing and duration on an oscilloscope along with the two laser pulses.

2.5 Detection & data acquisition systems

2.5.1 Field ionization

Using the methods described in this chapter, the atoms are now prepared in the correct state and the detection of the Rydberg atoms is possible. Rydberg experiments typically implement a *delayed field ionization (DFI)* or *selective field ionization (SFI)* scheme to detect the Rydberg atoms of interest. In this work, a combination of the two ionization methods are used and a spatially-integrating multi-channel plate (MCP) is used as a detector.

Delayed field ionization relies on the fact that the higher angular momentum states have a longer lifetime than the lower angular momentum states. Using data from Ref. [4], the lifetimes of the Rb $12f$ and $12g$ states and hydrogen $12f$, $12g$, $12h$, and $12i$ states are provided and presented in Table 2.6. Extrapolating to $n = 17$ in Rb, the lifetimes of

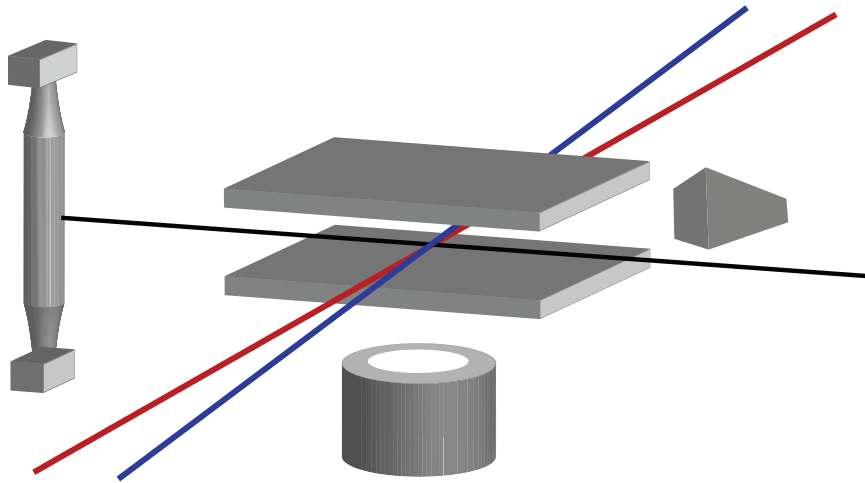


FIGURE 2.10: The experiment setup without the vacuum chamber for increased clarity. For consistency, the label designations remain the same: (a) rubidium oven, (b), field ionization plates, (c) laser beams focused at center of chamber, (d) multi-channel plate (MCP), and (e) microwave horn. This is not to scale and the size of the field plates are exaggerated.

$\ell = 3 - 6$ are shown in Table 2.7. It is evident that higher ℓ states have greater lifetimes. With delayed field ionization, this lifetime property can be experimentally leveraged to provide ℓ state selectivity knowing that the longer lifetime, higher ℓ states will outlive the shorter lifetime, lower ℓ states. Experimentally, field ionization pulses are typically delayed on the scale of the lifetimes of the Rydberg states calculated and shown in Table 2.7. Of particular note, the lifetime of the $12f$ state is significantly different in rubidium and hydrogen. This is the first glimpse in this thesis pointing to the fact that the f state in Rb is not hydrogenic when compared to higher ℓ states; this fact will be further elaborated on in the *Fine Structure* section of the next chapter.

Selective field ionization, on the other hand, relies on the fact that different Rydberg states ionize at different electric field amplitudes and at different times. This effect is illustrated in Figure 2.11 whereby field ionization amplitude is ramped in time and at different field strengths, ionization of different n levels occur. The energy required to ionize a Rydberg

Species	$n\ell$	Lifetime (ns)
Rb	12 <i>f</i>	1190
	12 <i>g</i>	3013
H	12 <i>f</i>	1849
	12 <i>g</i>	3098
	12 <i>h</i>	4699
	12 <i>i</i>	6612

TABLE 2.6: Tabulated lifetimes of H and Rb high- ℓ Rydberg states from data in Ref. [4].

$n\ell$	Lifetime (ns)
17 <i>f</i>	3379
17 <i>g</i>	8557
17 <i>h</i>	13345
17 <i>i</i>	18778

TABLE 2.7: Calculated lifetimes of high- ℓ Rb Rydberg states for $n = 17$ extrapolating from the data shown in Table 2.6 sourced from Ref. [4].

atom is given by

$$E = \frac{1}{16n^4} \quad (2.1)$$

where n is the principal quantum number [3]. Intuitively at higher n , the larger orbital radius of the valence electron results in a lower Coulomb force and a smaller required energy to strip the valence electron from the ionic core. Experimentally, the field required to ionize the Rydberg atom for $n = 16 - 19$ is shown in Table 2.8. Discrimination between the ℓ states is also possible by adjusting the field ionization threshold. As the field required for ionization increases, the spacing between the ℓ states also increases [10]. And, distinguishing between ℓ states is typically on the scale of 10 V/cm. To achieve the greatest signal to noise ratio for the spectroscopy measurements, a combination of selective field ionization and delayed field ionization are leveraged.

The Rydberg atoms are ionized between the field ionization plates. The electric field plates and MCP locations are shown in Figure 2.4, and exaggerated, to be seen more clearly without the vacuum chamber in Figure 2.10. At the center of the electric field ionization

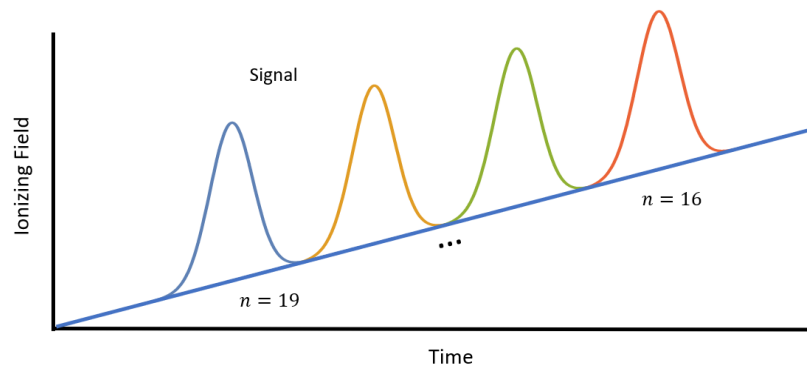


FIGURE 2.11: An illustrative example of field pulse amplitude vs. n , not drawn to scale. This shows a visualization of selective field ionization where the ionizing field amplitude required to ionize a Rydberg atom is lower for higher n .

plates (labeled (b) in Fig. 2.10) and separated by 1.8 cm, the Rydberg atoms must be ionized. To accomplish this, a home-built circuit externally connected to the vacuum chamber with electrical feedthroughs to the inside of the chamber is used.

The field pulse is applied to the lower plate in Figure 2.10 while the upper plate remains grounded. The polarity of the field pulse dictates whether ions or electrons will be accelerated toward the MCP. With this setup, it is therefore possible to detect either electrons or ions following ionization. The field ionization circuit responsible for the electric field pulse is drawn in Figure 2.12. A voltage is supplied to V_{in} of the circuit by a dc Kepco power supply. The circuit first stores energy in a capacitor, then releases that energy into a 1:30 transformer when triggered by a *field effect transistor (FET)*. A static dc voltage bias can be applied to the high voltage electric field plate. This is accomplished by applying a dc voltage bias to the lower magnitude voltage terminal on the output side of the transformer, connected to the electric field plate. The characteristics of this home-built circuit are a rise time on the order of $3 \mu\text{s}$ and a maximum amplitude of just under 7 kV. The maximum pulse amplitude limit is set by the point where high voltage arcing occurs. Figure 2.11 provides an illustrative view showing that as field ionization amplitude is ramped in time,

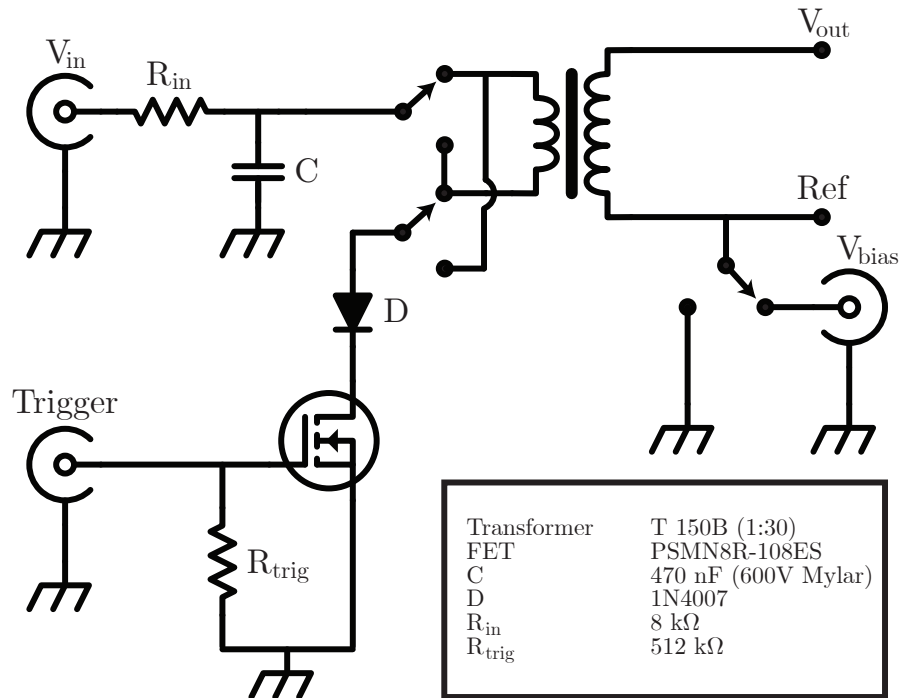


FIGURE 2.12: Home-built field ionization circuit. The circuit first stores energy in a capacitor, then releases that energy into a 1 : 30 transformer when triggered by a field effect transistor (FET). The polarity to dictate the direction to accelerate ions or electrons toward the detector is set with a DPDT switch before the transformer. A bias can be applied to the field pulse, dictated by an applied voltage to a terminal on the output side of the transformer, and enabled with a SPDT switch. The characteristics of this home-built circuit are a rise time on the order of $3 \mu\text{s}$ and a maximum amplitude of just under 7 kV. Specific electronic components used are listed in the legend.

n	Source Voltage (V)	Field (V/cm)
16	195	3900
17	162	3240
18	130	2600
19	96	1920

TABLE 2.8: Experimentally determined selective field ionization pulse amplitude thresholds vs. n for $n = 16 - 19$. The source voltage is listed in the second column, a 1:30 transformer is used, and the field plate separation for this measurement is 1.5 cm. The electric field is computed and listed in the third column.

ionization of lower n levels occurs.

Table 2.8 and Figure 2.13 show the field ionization pulse amplitude where Rydberg atom ionization occurs for $n = 16 - 19$. Unfortunately, the limiting factor for measuring lower n states is the increasing ionization threshold as n decreases. For the electronics and vacuum feedthrough high voltage ratings used in this apparatus, it is impossible to measure $n = 15$ or lower with this setup due to high voltage arcing between the electric field plates in vacuum and voltage limitations of electrical specifications of the components in the circuit.

2.5.2 Signal detection and processing

Signal detection is achieved with a *multi-channel plate (MCP)* in a spatially integrating configuration. A MCP is a glass plate with millions of spatially separated channels that act as electron multipliers. The multiplication process is achieved through an avalanche effect where an ion or electron hits a channel wall and causes a cascade of additional electrons to be emitted and accelerated due to an electric field applied to the MCP. Finally, the cascade of electrons exits the MCP and get accelerated towards a current collector, or *anode*. An illustration of this process is shown in Figure 2.14.

The detector design chosen for this experiment features two MCPs with angled channels rotated at 180 degrees from each other. This dual MCP plate detector design is shown

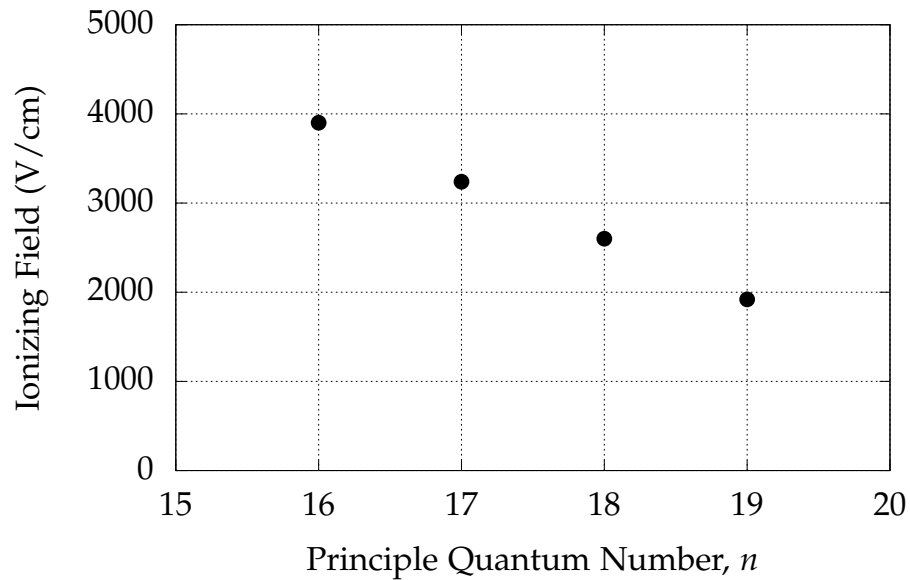


FIGURE 2.13: Measured field ionization pulse amplitude threshold vs. n plotted using data from Table 2.8.

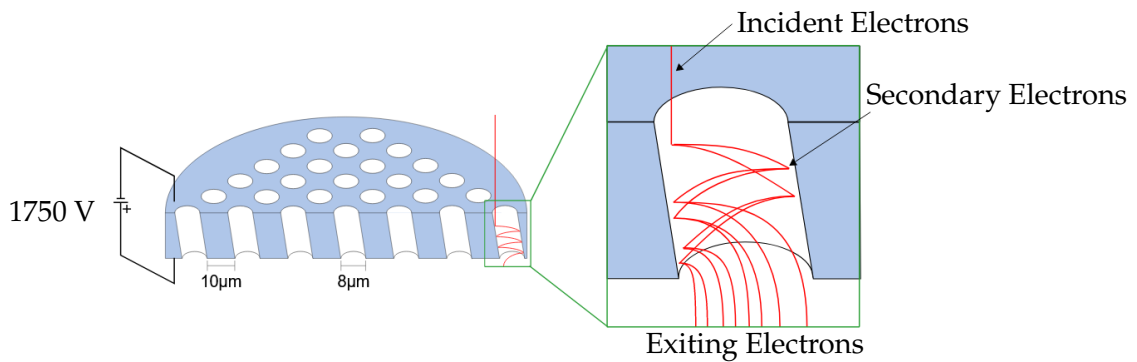


FIGURE 2.14: Illustration of the operation of a multi-channel plate. A MCP is a glass plate with millions of spatially separated channels that act as electron multipliers. An ion or electron hits the wall of a MCP channel and causes a cascading avalanche of additional electrons to be emitted and accelerated due to an electric field applied across the MCP. The cascade of the electrons exits the MCP and gets accelerated towards a current collector, not shown here. Figure adapted from Ref. [11].

in Fig. 2.15. Ions pass through a grounded grid, are incident on the first MCP, then the electrons that exit the first plate cascade into the second and the angle between the channels minimizes feedback while increasing gain. There is a physical separation between the two plates allowing for charge to spread across multiple channels; this significantly increases gain, but reduces spatial resolution. For the purposes of this work, spatial resolution is not of concern and the greater signal is beneficial.

The electronics design implementation for the MCP plates are shown in Figure 2.16. As mentioned in the previous section, the field ionization pulse can either accelerate electrons or ions toward the MCP for detection. Therefore, an important design aspect of this circuit is the ability to accommodate the detection of either ions or electrons. In both of these cases, the MCP voltages must be set so the appropriate charged particle is subject to an attractive potential while bearing in mind that only electrons are produced by an MCP. To detect electrons, approximately +1750 V is applied to the *+HV In* terminal of the MCP circuit in Fig. 2.16 and the *-HV In* terminal is grounded. To detect ions, approximately -1750 V is applied to the *-HV In* terminal of the MCP circuit in Fig. 2.16 and the *+HV In* grounded. For the experimental measurements, the electronics are configured to detect ions.

For signal detection, a higher voltage applied across the MCP results in a greater electric field and thus a greater avalanche effect with more electrons exiting the MCP for detection. This process produces a greater signal; however, the main drawback of the higher applied voltage is the electrical limitations of the MCP. A maximum voltage of approximately 2000 V may be applied across the MCP, otherwise irreversible damage to the detector may occur. Therefore, 1750 V was chosen to provide a relatively high signal without reaching the threshold of damaging the MCP. The signal following the anode is coupled through a 100pF capacitor to a BNC cable, then to the data acquisition equipment.

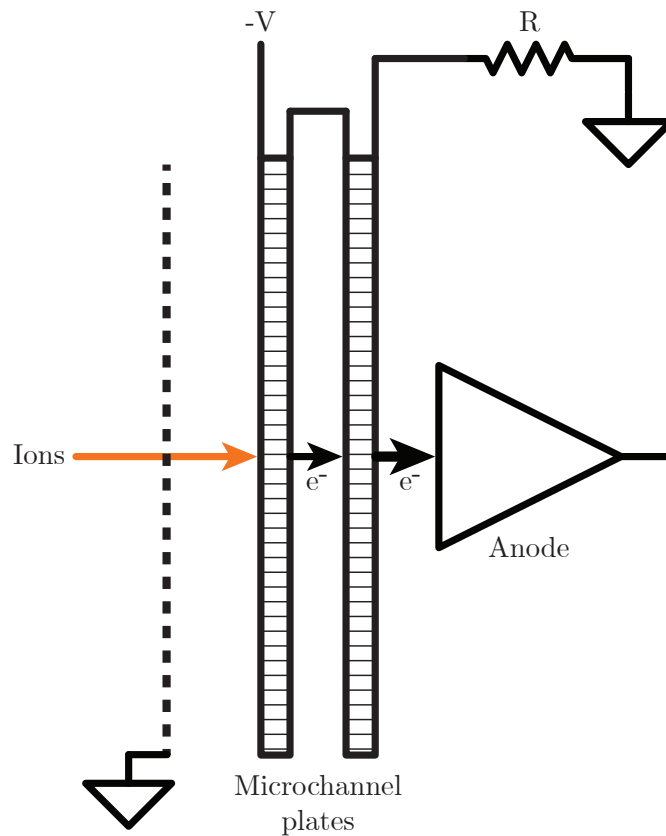


FIGURE 2.15: Dual MCP detector design with angled channels rotated at 180 degrees from each other. Ions pass through a grounded grid, are incident on the first MCP, then the electrons that exit the first plate cascade into the second and the angle between the channels minimizes feedback while increasing gain. There is a physical separation between the two plates allowing for charge to spread across multiple channels; this significantly increases gain, but reduces spatial resolution.

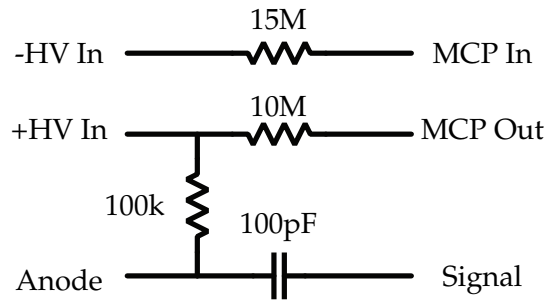


FIGURE 2.16: Multi-channel plate circuit diagram. To accommodate the detection of either electrons or ions depending upon the polarity of the field ionization plates, MCP voltages must be set for the appropriately charged particle to be subject to an attractive potential while bearing in mind that only electrons are produced by an MCP. To detect electrons, approximately +1750 V is applied to the *+HV In* terminal and the *-HV In* terminal is grounded. To detect ions, approximately -1750 V is applied to the *-HV In* terminal and the *+HV In* grounded.

2.6 Experiment timing

All experimental timing is triggered from the Quanta-Ray DCR-2A flashlamp output. The flashlamps in the DCR-2A fire at a repetition rate of 20 Hz defined by a switch setting on the DCR-2A. The DCR-2A flashlamp trigger output feeds into the trigger input of a SRS DG 535 delay generator to then trigger the Q-Switch of the DCR-2A as well as the flashlamps and Q-Switch of the Continuum laser. The Q-Switch of the DCR-2A is triggered approximately $250 \mu\text{s}$ following the flashlamp trigger to allow for sufficient time for population inversion to occur in the Nd:YAG laser cavity for maximum laser power. The SRS delay generator also outputs a trigger for the flashlamps of the Continuum laser. This operation is referred to as *Direct Access Trigger (DAT)* mode in the Continuum laser's user manual. The relevant manual pages are shown in Appendix F. The Continuum's Q-Switch is triggered by an internal digital delay set using the front panel of its respective laser controller. The parameters for the SRS delay generator are shown in Table 2.9 with an intuitive

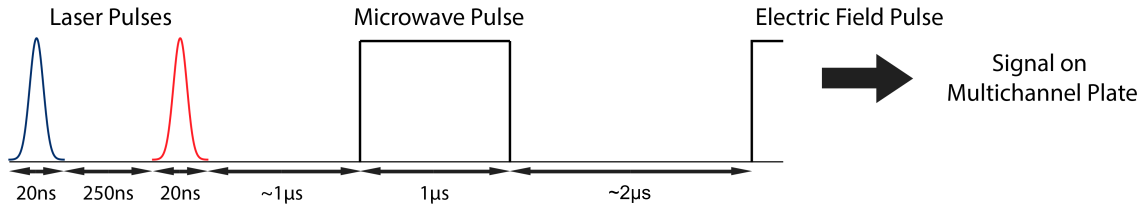


FIGURE 2.17: An illustrative representation of the experiment timing. The first laser pulse drives the $5s \rightarrow 6p$ atomic transition. A delay is introduced to allow the atoms in the $6p$ state to decay to the $4d$ state. The next laser pulse is applied to drive the atoms into the Rydberg nf state. A microwave pulse or combined microwave and rf pulse with a duration of $1 \mu s$ is applied approximately $1 \mu s$ following the second laser pulse. Using delayed field ionization, an electric field pulse is applied. Not pictured here is the timing of the detection process. The field ionization and MCP are configured to detect ions and it takes approximately ten microseconds for the ions to reach the detector. A boxcar integrator integrates the ionization signal and delivers the result to a data acquisition system.

description of the interpretation of these parameters in the table's description. Additionally, the electrical connections are shown in Figure 2.18. The ultimate goal of these efforts is to have the Continuum laser pulse follow the DCR-2A laser pulse by 250 ns, shown in the timing diagram in Figure 2.17. The purpose of this is a maximal atom population in the nf Rydberg states, described earlier in this chapter.

Attention can now be turned to the microwave and rf field pulse generation, followed by the field ionization pulse, and subsequent signal data acquisition. A high-level block diagram of the instruments in this system and their general configuration is shown in Figure 2.19. Following the laser pulses, a Berkeley Nucleonics Corporation Model 8010 Pulse Generator generates the microwave field pulse. This is set to a delay of approximately $1 \mu s$ following the laser pulses with a duration of $1 \mu s$ for the microwave and rf applications. This pulse generator is triggered by the C output of the SRS delay generator. A second Berkeley Nucleonics Corporation Model 8010 Pulse Generator is triggered relative to the microwave pulse and the pulse delay is adjusted for delayed field ionization. This delay is adjusted depending on the ℓ state being measured and experimentally optimized to maximize the signal to noise. The delay of the field ionization pulse is typically set to

Parameter	Equation
A	$T + 95 \mu s$
B	$A + 10 \mu s$
C	$B + 150 \mu s$
D	$C + 7 \mu s$

TABLE 2.9: SRS DG 535 delay generator parameters. Intuitively, the T parameter is the trigger input from the Quanta-Ray DCR-2A flashlamp trigger output. The A parameter determines the amount of time before triggering the flashlamps of the Continuum Surelite SLI-20. The B parameter defines the pulse duration necessary to trigger the flashlamps of the Continuum specified by the operator's manual. The C parameter defines the time after the Continuum flashlamps fire before triggering the DCR-2A Q-Switch; this is to provide sufficient time for population inversion in the Nd:YAG laser cavity. The D parameter defines the pulse duration of the DCR-2A Q-Switch trigger; specified by the DCR-2A operator's manual.

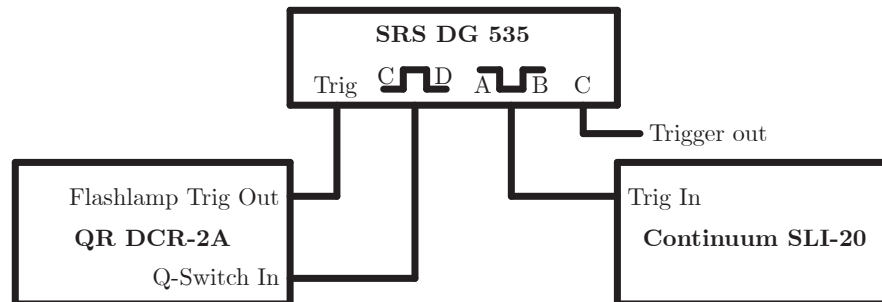


FIGURE 2.18: Electrical connection diagram for the laser triggering system. A SRS 535 DG is responsible for triggering the two laser pulses and the microwave pulse generator. First the flashlamps on the Quanta-Ray DCR-2A Nd:YAG trigger (T) the SRS 535 DG. The SRS 535 DG then provides a negative voltage pulse of duration D to trigger the flash lamps of the Continuum Surelite SLI-20 Nd:YAG. This laser has a digital delay circuit to switch on the Q-Switch at a programmed later time. At time A , a B duration positive voltage pulse triggers the Q-Switch of the DCR-2A. Output C on the delay generator serves as the trigger output to the microwave pulse generator. Timings for delay parameters T , A , B , C , and D are specified in Table 2.9.

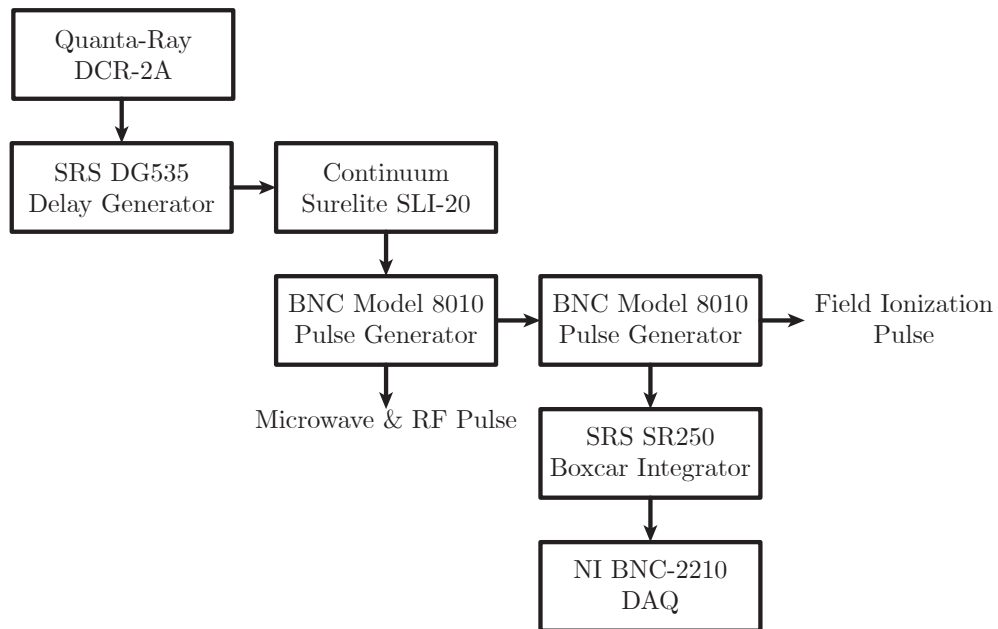


FIGURE 2.19: Experimental timing and control block diagram. The arrows indicate either a trigger or a signal path.

approximately $2 \mu\text{s}$ following the microwave pulse. The duration of the electric field pulse is dictated by the electronics of the field ionization circuit in Figure 2.12, and is approximately $3 \mu\text{s}$.

The boxcar integrator, responsible for integrating the ionization signal, is externally triggered by the field ionization pulse generator. The typical width of the signal to be integrated is $5 \mu\text{s}$ with a relatively sizable delay from the field pulse on the order of ten microseconds being dictated by the speed of the ions being accelerated to the MCP. The Q-Switch of the DCR-2A triggers the acquisition sequence of the NI BNC-2210 to record the output of the boxcar integrator. These systems are shown in the block diagram in Figure 2.19 and an abbreviated timing diagram is shown in Fig. 2.17 depicting the laser pulses, microwave/rf pulse, and electric field pulse.

The experiment data acquisition system consists of a Stanford Research Systems SR250

Boxcar Integrator, National Instruments (NI) BNC-2210 analog input/output data acquisition device, and a Windows computer with LabVIEW™. The analog voltage signal from the detector is fed to the boxcar integrator which integrates the signal in a specified time window (or gate) relative to the trigger. The SR250 has an adjustable delay from a few nanoseconds to 100 ms following an external trigger pulse before an adjustable gate of 2 ns to 15 μ s is used to integrate over an analog signal. Lastly, exponential averaging can be used to reduce noise applying to up to thousands of samples – in this experiment, no exponential averaging is used since microwave frequencies are swept to find an atomic resonance. This feature would skew the results in the direction of the previously applied frequency in the frequency scan.

The output of the boxcar integrator is sent to the National Instruments (NI) BNC-2210 analog input/output device triggered by the DCR-2A. Upon a trigger by the SRS DG 535 delay generator, the voltage on the analog input is recorded by a custom LabVIEW™ program. The LabVIEW™ program interfaces with the microwave and rf synthesizers via GPIB commands to set frequencies and powers. The microwave frequency is swept with the limits, step size, and total number of scans defined by the LabVIEW™ front panel interface. Typically, limits and step sizes are defined to yield 150 microwave frequency steps per scan. For each microwave frequency step, the measurement is repeated 15 times and the average of the 15 signals is recorded. Scanning over the entire frequency range typically takes 3-5 minutes. Each full scan is repeated 10-15 times. Following the data acquisition, the frequency spectrum measurements are averaged. Although data is collected at a rate of 20 Hz, each atomic spectra measurement using this process typically take 10-15 minutes. The LabView custom program interface and block diagram are shown in Appendix G.

References

- [1] Jeonghun Lee, J. Nunkaew, and T. F. Gallagher. “Microwave spectroscopy of the cold rubidium ($n + 1$) $d\ 5 / 2 \rightarrow n\ g$ and $n\ h$ transitions”. en. In: *Physical Review A* 94.2 (Aug. 2016), p. 022505. ISSN: 2469-9926, 2469-9934. DOI: [10.1103/PhysRevA.94.022505](https://doi.org/10.1103/PhysRevA.94.022505). URL: <https://link.aps.org/doi/10.1103/PhysRevA.94.022505> (visited on 05/25/2020).
- [2] Jirakan Nunkaew. “Dielectronic Recombination, Autoionization and Non-Adiabatic Core Polarization of Rydberg Two-Electron Atoms”. PhD thesis. University of Virginia, Dec. 2011. DOI: [10.18130/V3H53T](https://doi.org/10.18130/V3H53T). URL: https://libraetd.lib.virginia.edu/public_view/pc289j378 (visited on 05/26/2020).
- [3] Thomas F. Gallagher. *Rydberg atoms*. Digitally printed 1st pbk. version. Cambridge monographs on atomic, molecular, and chemical physics 3. Cambridge ; New York: Cambridge University Press, 2005. ISBN: 978-0-521-02166-1.
- [4] Anders Lindgård and Svend Erik Nielsen. “Transition probabilities for the alkali isoelectronic sequences Li I, Na I, K I, Rb I, Cs I, Fr I”. en. In: *Atomic Data and Nuclear Data Tables* 19.6 (June 1977), pp. 533–633. ISSN: 0092640X. DOI: [10.1016/0092-640X\(77\)90017-1](https://doi.org/10.1016/0092-640X(77)90017-1). URL: <https://linkinghub.elsevier.com/retrieve/pii/S0092640X77900171> (visited on 06/10/2020).
- [5] Orazio Svelto and David C. Hanna. *Principles of lasers*. eng. 5. ed. OCLC: 699877195. New York, NY: Springer, 2010. ISBN: 978-1-4419-1302-9 978-1-4419-1301-2.
- [6] K. H Drexhage and Fritz Peter Schäfer. *Dye lasers*. English. OCLC: 880598177. Berlin, New York: Springer-Verlag, 1973. ISBN: 978-3-540-06438-1 978-3-662-11579-4 978-3-662-11581-7. URL: <http://link.springer.com/openurl?genre=book&isbn=978-3-540-51558-6> (visited on 06/05/2020).

-
- [7] J. E. Sansonetti and W. C. Martin. “Handbook of Basic Atomic Spectroscopic Data”. en. In: *Journal of Physical and Chemical Reference Data* 34.4 (Dec. 2005), pp. 1559–2259. ISSN: 0047-2689, 1529-7845. DOI: [10.1063/1.1800011](https://doi.org/10.1063/1.1800011). URL: <http://aip.scitation.org/doi/10.1063/1.1800011> (visited on 06/06/2020).
- [8] J. Reader and G.L. Epstein. In: *Natl. Bur. Stan (U.S.) Unpublished* (1980).
- [9] Lauren Levac. “Observation of the Dipole-Dipole Interaction in Dressed State Rydberg Atoms by Microwave Spectroscopy”. English. PhD thesis. Charlottesville, VA: University of Virginia, Department of Physics, MA (Master of Arts), 2013, May 2013. URL: <https://search.lib.virginia.edu/catalog/5h73pw24r>.
- [10] T. F. Gallagher et al. “Field ionization of highly excited states of sodium”. en. In: *Physical Review A* 16.3 (Sept. 1977), pp. 1098–1108. ISSN: 0556-2791. DOI: [10.1103/PhysRevA.16.1098](https://doi.org/10.1103/PhysRevA.16.1098). URL: <https://link.aps.org/doi/10.1103/PhysRevA.16.1098> (visited on 07/24/2020).
- [11] Wikimedia Commons. *File:Mcp-de.svg* — *Wikimedia Commons, the free media repository*. 2020. URL: <https://commons.wikimedia.org/w/index.php?title=File:Mcp-de.svg&oldid=426323292>.

3 | Atomic spectra measurements

3.1 Introduction

Spectroscopy measurements of rubidium $nf \rightarrow ng$, $nf \rightarrow nh$, and $nf \rightarrow ni$ bound Rydberg states provide a useful means for determining core polarizability. The importance of these measurements are explicitly described in the *Introduction* chapter; but to briefly reiterate, accurate electric dipole and quadrupole polarizabilities of the ionic core are useful in calculating atomic dipole matrix elements and PNC effects to aid in theory and future experiments [1, 2]. Spectroscopy of these atomic transitions are achieved by a single-photon transition in the case of $nf \rightarrow ng$, a two-photon transition in the case of $nf \rightarrow nh$, and a three-photon transition in the case of $nf \rightarrow ni$. A single photon transition uses one photon to excite from the initial state to the final state, whereas multi-photon transitions use two or more photons to drive to a virtual state detuned from the resonance of the intermediate energy level and ultimately to the final state.

Spectroscopy of high- ℓ states inherently have many experimental challenges. Signal-to-noise ratio is reduced for high angular momentum states since multi-photon transitions are more difficult to drive. This is mainly a result of the multi-photon transitions exciting to a detuned intermediate virtual state. The transition probability is decreased as detuning from transition resonance is increased. However, spectroscopy of high- ℓ states are desirable given reduced core penetration effects. Core penetration effects are present for $\ell \leq 3$. Some previous experiments were conducted using Rb nf Rydberg states despite this limitation [3, 4]. By design, this experiment is constrained to $\ell > 3$ to minimize core

penetration effects that were present in previous experiments.

Throughout the course of these measurements, systematic effects that limit measurement precision and accuracy are taken into account. These effects include dc Stark shifts, ac Stark shifts, and Zeeman shifts. DC Stark effect shifting of the energy levels occurs with even a modestly small stray electric field. This effect is present for both single and multi-photon transitions and are taken into account in the longitudinal direction of the electric field plates. However, stray electric fields are uncontrolled in the direction transverse to the electric field plates. This results in an unknown frequency shift, which must be accounted for. The ac Stark effect shifts the energy levels as a function of microwave and rf power for multi-photon transitions. This effect can be mitigated by measuring transition frequencies at multiple microwave and rf powers, then extrapolating to zero microwave and rf power. Lastly, Zeeman effects present a source of experimental uncertainty due to energy shifts as a result of a background magnetic field. These systematic effects are taken into account and final spectroscopic results are tabulated.

3.1.1 Fine structure

For the core polarization results obtained from the spectroscopic measurements in this experiment to be accurate, the $n\ell$ state core penetration effects must be negligible. For rubidium, the nf Rydberg state is known to exhibit an inverted fine structure, indicating core penetration effects. Typically for alkali metals, the ℓ state succeeding the one exhibiting an inverted fine structure is non-penetrating [5]. Fine structure measurements of the ng state are made to confirm that this is the case. The spectroscopic measurements are conducted relative to the nf state with measurements to ng , nh , and ni . Relative measurements $ng \rightarrow nh$ and $nh \rightarrow ni$ can thus be determined and are used in the core polarization model analysis. Furthermore, knowledge of fine structure splitting is necessary for determining the center of gravity transition frequencies.

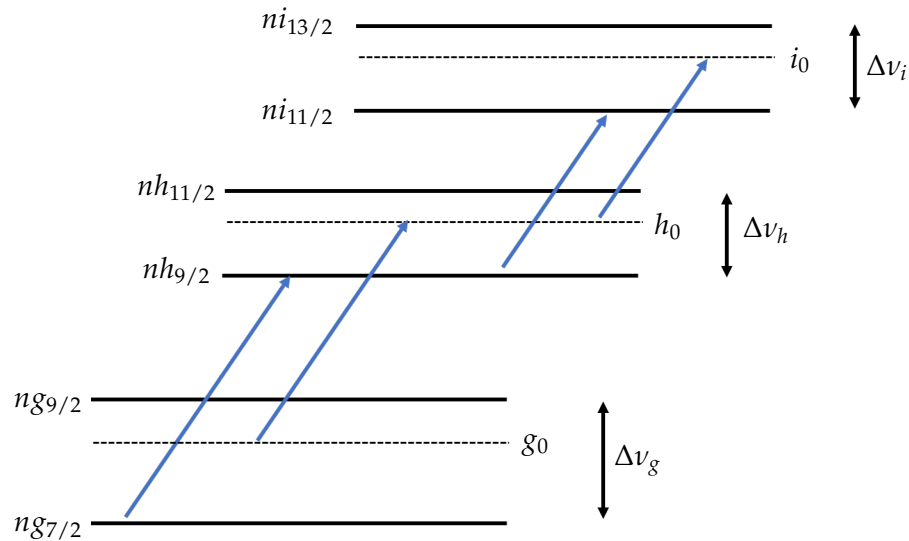


FIGURE 3.1: Doublet fine structure center of gravity. Fine structure splitting for each ℓ state measured in this work is shown on the right side as Δv_g , Δv_h , and Δv_i . Fine structure states are shown on the left hand side of the solid lines. The center of gravity between the fine structure states are depicted as dashed lines. Arrows between the solid line fine structure states show the energies extracted from the measurements in this work. Energies between the doublet center of gravities, denoted as arrows between the dashed lines, are calculated.

Due to the Rydberg electron of Rb for $\ell < 4$ penetrating the ionic core, energy levels are shifted as a result of both core penetration effects and core polarization effects. To measure mainly core polarization effects and neglect core penetration effects per the core polarization model, core penetration of the ng Rydberg electron must be negligible. Core penetration effects impact fine structure since energy levels are shifted due to the Rydberg electron's orbit around the ionic core. As expressed in the previous section, the ng state is expected to be hydrogenic due to the inverted fine structure of the nf state, but also experimentally verified here.

The consideration must also be made for the fact that the core polarization model omits the fine structure. Fine structure shifts are thus removed for the analysis by considering the fine structure doublet center of gravity. Fine structure energy level shifts are due to the

j	E_{FS}	ΔE_{FS}
$\ell + 1/2$	$f_{n\ell}\ell/2$	$(2\ell + 1)f_{n\ell}/2$
$\ell - 1/2$	$-(\ell + 1)f_{n\ell}/2$	

TABLE 3.1: Spin-orbit interaction energies calculated and tabulated per equation (3.1) for $s = 1/2$.

ℓ	$E_{FS,j=\ell+1/2}$	$E_{FS,j=\ell-1/2}$	ΔE_{FS}	$E_{FS,j=\ell+1/2}/\Delta E_{FS}$	$E_{FS,j=\ell-1/2}/\Delta E_{FS}$
4	4/2	-5/2	9/2	4/9	-5/9
5	5/2	-6/2	11/2	5/11	-6/11
6	6/2	-7/2	13/2	6/13	-7/13

TABLE 3.2: Spin-orbit interaction energy ratios for the $4 \leq \ell \leq 6$ states of interest. These ratios are applied to find the center of gravity transition frequencies.

relativistic effects in combination with the valence electron's spin and angular momentum. This effect is known as the *spin-orbit interaction*, with the spin-orbit fine structure energy shift for hydrogen given by

$$E_{FS} = \frac{f_{n\ell}}{2} [j(j+1) - \ell(\ell+1) - s(s+1)] \quad (3.1)$$

where $f_{n\ell}$ is a function of only n and ℓ . The spin quantum number s is set to $s = 1/2$ for the spin-1/2 valence electron. Ratios between the fine structure levels and center of gravity are easily found and calculated (Tables 3.1 and 3.2). A pictorial representation of the center of gravities for the ng , nh , and ni states is shown in Figure 3.1.

Calculation of the center of gravity transition frequencies are

$$\nu_{g_0 \rightarrow h_0} = \nu_{g_{7/2} \rightarrow h_{9/2}} - \frac{5}{9} \Delta \nu_g + \frac{6}{11} \Delta \nu_h \quad (3.2)$$

and

$$\nu_{h_0 \rightarrow i_0} = \nu_{h_{9/2} \rightarrow i_{11/2}} - \frac{6}{11} \Delta \nu_h + \frac{7}{13} \Delta \nu_i \quad (3.3)$$

where $\Delta\nu_g$, $\Delta\nu_h$, and $\Delta\nu_i$ are the fine structure splittings of the ng , nh , and ni states, respectively. Since these states are hydrogenic, hydrogen fine structure splittings are used in this calculation to determine the center of gravity transition frequencies.

3.1.2 Spectral linewidth broadening

Observable linewidth broadening comes from a combination of several effects. The most pronounced effects include *transform broadening* dictated by the microwave pulse duration, Rabi frequency dictated by microwave power, and Zeeman splitting due to external magnetic fields. The microwave pulse duration is $\tau = 1 \mu\text{s}$. Transform broadening limits the minimum spectral linewidth that can be measured to approximately the inverse of the pulse duration, $1/\tau = 1 \text{ MHz}$. In principle, transform broadening can be reduced with a longer microwave pulse, however other sources of error must also be reduced before this would be an advantage.

Next, a consideration must be made for *Rabi frequency*, which is defined as

$$\Omega_{if} = \frac{\mathbf{d}_{if} \cdot \mathcal{E}}{\hbar} \quad (3.4)$$

where \mathbf{d}_{if} is the transition dipole moment and for the initial to final state $i \rightarrow f$ transition; and \mathcal{E} is the microwave electric field. Rabi frequency is the frequency at which Rabi oscillations occur for an atomic transition. Rabi oscillations are the cyclical oscillations between the excited state and non-excited state in the presence of an external ac electric field. The atom will absorb the microwave photons and re-emit them via stimulated emission at the Rabi frequency defined above. The atom populations in each of the two states in this system cyclically fluctuate in time between these two states. Of note, Rabi oscillations are not observed in this data since state detection occurs after the incident microwave and rf fields and pulse duration remains constant.

The requirement is set forth that the Rabi frequency be approximately equivalent to the inverse of the pulse duration, τ .

$$\Omega_{if} \approx 1/\tau \quad (3.5)$$

The Rabi frequency should be less than or equal to the inverse of the duration of the microwave pulse to keep transform broadening below $1/\tau = 1$ MHz. For a Rydberg atom transition for which $n' = n$ and $\ell' = \ell \pm 1$, a small microwave field is required to drive the transition and the time in which the atoms are exposed to microwaves is on the order of a few microseconds, depending upon n since the dipole transition moment \mathbf{d}_{if} with Rabi frequency depends on scales as n^2 . To reduce power broadening where it is no longer a limiting factor, Ω_{if} must also be reduced. This is achieved experimentally by reducing microwave power until a linewidth of 1 MHz is observed.

3.1.3 DC Stark effect

While the linewidth limits the precision with which transition frequency is measured, the accuracy of the measurement is limited by effects that shift the frequency from its nominal value. The most important of these is the *Stark effect* [6]. The *dc Stark effect* is characterized by the shifting of energy levels of an atomic state by an externally applied electric field. The atom's interaction with the external electric field is described by the interaction energy

$$V_{int} = -\mathbf{d} \cdot |\mathcal{E}| \hat{z} \quad (3.6)$$

where \mathbf{d} is the electric dipole moment operator and \mathcal{E} is the interacting electric field along the z -direction. The electric dipole moment scales as n^2 , thus for Rydberg atoms characterized by high- n , the energy shift due to an external static electric field is relatively large. Perturbation theory is applied and to second order, the energy shift of the states are given

by

$$\Delta E = -e^2 |\mathcal{E}|^2 \sum_{n'\ell'j' \neq n\ell j} \frac{|\langle n, \ell, j, m_j | z | n', \ell', j', m'_j \rangle|^2}{E_{n'\ell'j'} - E_{n\ell j}}. \quad (3.7)$$

This shift is known as the *quadratic Stark effect*. The matrix elements are often zero, but non-zero for off-diagonal elements according to the selection rules $m = m'$ and $\ell' = \ell \pm 1$ defined by symmetries of the system.

Expressing this energy shift in terms of polarizability is given by

$$\Delta E = -\frac{1}{2} \alpha \langle \mathcal{E} \rangle^2 \quad (3.8)$$

where polarizability is

$$\alpha = 2e^2 \sum_{n'\ell'j' \neq n\ell j} \frac{|\langle n, \ell, j, m_j | z | n', \ell', j', m'_j \rangle|^2}{E_{n'\ell'j'} - E_{n\ell j}}. \quad (3.9)$$

Due to symmetry, the terms that vary linearly with electric field strength disappear and the only terms that remain are given by the quadratic Stark effect in Eqn. (3.7).

Stark shifts can be computed directly for hydrogen and rubidium, and serve as a means to check the experimental results and implement systematic uncertainties. It is understood that the matrix elements for Rb cannot be computed; therefore, the method to determine the Stark structure for alkali metal atoms presented by Zimmerman, *et al.* is implemented here [7]. For hydrogen, all of the matrix elements are analytically known. To determine energy shifts in the presence of a given external static electric field, the energy matrix is diagonalized and the eigenvalues are the shifted energy values. This calculation is repeated for each electric field of interest. To calculate the Stark shifts for rubidium, hydrogenic wavefunctions are used along with Rb energy shifts including fine structure splitting and quantum defects. It is assumed that the matrix elements are the same as that for hydrogen, but the experimentally determined zero field energy values are used. Once again, the energy matrix is diagonalized and the eigenvalues are the shifted energy values for a

n	α_{fg} (MHz cm ² /V ²)	α_{fh} (MHz cm ² /V ²)	α_{fi} (MHz cm ² /V ²)
17	23.0	75.4	144.8
18	34.5	113.1	217.2
19	50.2	164.4	315.7

TABLE 3.3: DC Stark shift polarizability coefficients for $n = 17 - 19$ $f \rightarrow g$, $f \rightarrow h$, and $f \rightarrow i$ transitions are calculated using the methods described herein and tabulated. The polarizability coefficient is the α_{if} coefficient of the quadratic Stark effect equation $\Delta E = -(1/2)\alpha_{if}\langle\mathcal{E}\rangle^2$.

given external static electric field. The computed Stark maps for both H and Rb are shown in Figures 3.2 and 3.3, respectively. Computation of the Stark shifts are performed in this work by directly diagonalizing the Hamiltonian

$$H = H_0 + V_{int}, \quad (3.10)$$

where H_0 is the unperturbed Hamiltonian. A basis set of the highest allowable ℓ values is used for $n = 17 - 19$.

For the Stark maps in these figures, magnetic quantum number $m_j = 1/2$ and electric fields up to 5000 V/cm are calculated and displayed to exemplify the effects at higher fields. For the purposes of this work, lower electric fields on the order of 1 V/cm are of interest since these lower electric field strengths are applied experimentally. Stark maps for the $n = 17 - 19$ $f \rightarrow g$, $f \rightarrow h$, and $f \rightarrow i$ transitions are calculated for $m_j = 1/2$ at low fields and transition polarizability coefficients α_{if} of Eqn. (3.8) and presented in Table 3.3. The calculated energy shifts for each of these transitions are shown in Figure 3.4 for $n = 17, m_j = 1/2$. These theoretically calculated values are compared to experimental data in the following sections and play a role in determining systematic uncertainty due to uncontrolled stray electric fields.

Knowing that the dc Stark effect is present for the spectroscopic measurements in this work means that it must be accounted for accordingly. The transition frequency at zero static electric field between the atomic states is principally of interest and needs to be

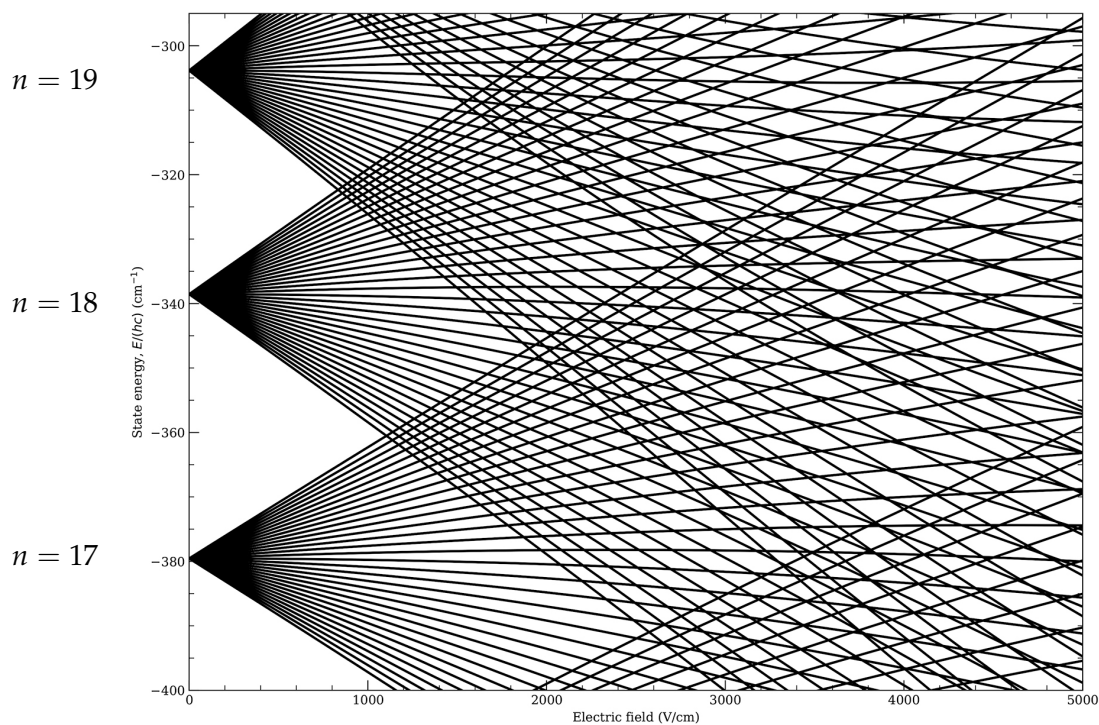


FIGURE 3.2: The hydrogen Stark map is calculated by finding energy eigenstates, diagonalizing the Hamiltonian, then numerically integrating over the radial part of the wavefunction and evaluating the analytical spherical harmonics. This calculation is performed for each static electric field strength. The hydrogen energy levels shown in the plot are centered at $n = 17 - 19$ using $m_j = 1/2$, and an applied static field of $0 - 5000 \text{ V/cm}$ are computed.

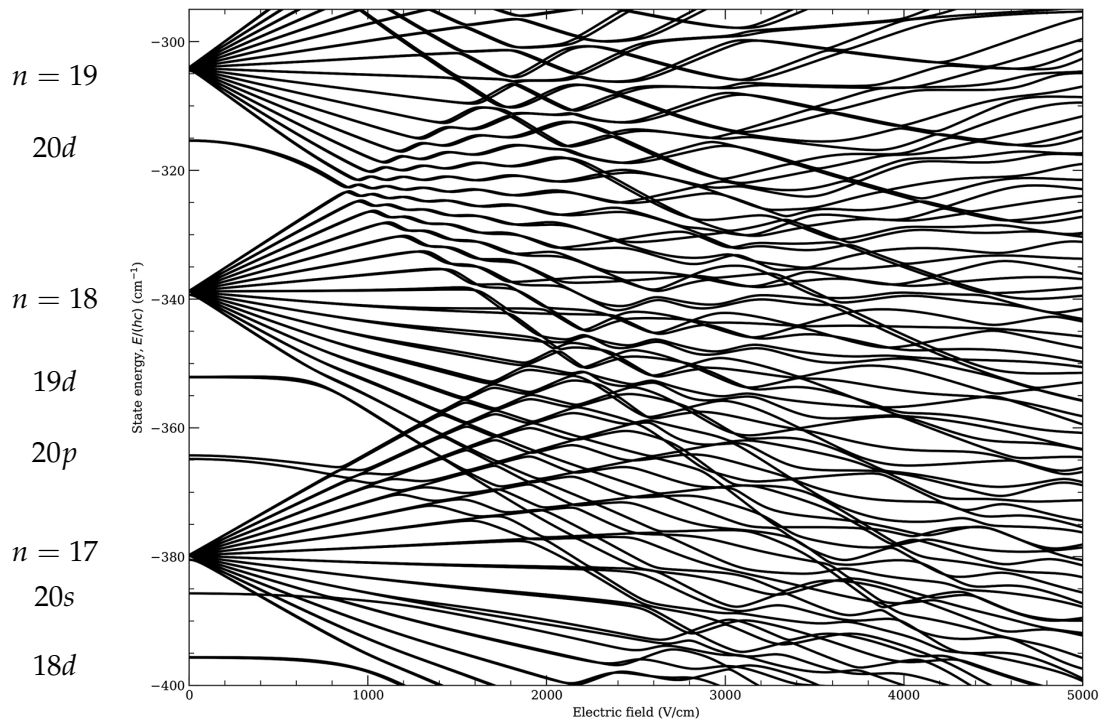


FIGURE 3.3: The rubidium Stark map is calculated in the same fashion as the hydrogen case, but now includes core polarization effects. The scale of energy levels shown in the plot are centered at the Rydberg $n = 17 - 19$ states, with $m_j = 1/2$, and an applied static field of 0 – 5000 V/cm computed.

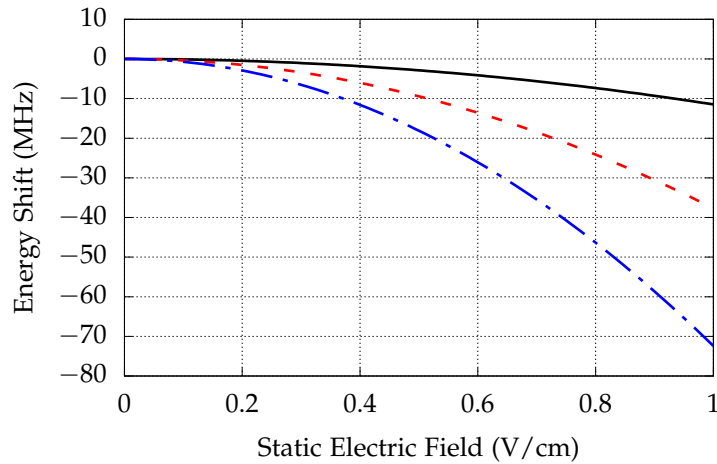


FIGURE 3.4: Calculated Stark shifts for the $f \rightarrow g$, $f \rightarrow h$, and $f \rightarrow i$ transitions are plotted as a difference from their zero field value for $n = 17, m_j = 1/2$. The solid black line corresponds to the $f \rightarrow g$ transition, the dashed red line corresponds to the $f \rightarrow h$ transition, and the dotted dashed blue line corresponds to the $f \rightarrow i$ transition.

known for accurate measurements. Observations of the dc Stark shifts allow for the reduction of this effect by experimentally applying an external static electric field. Unfortunately, stray electric fields limit the accuracy of these measurements, and are present for various reasons. The main reason being due to charge buildup on the surface of the electric field plates. Ultimately, the theoretical calculations and experimental observations of the dc Stark shifts provide the insight into the inclusion of systematic uncertainties due to an unknown stray electric field that affect the experimental results.

3.1.4 AC Stark effect

An additional source of error present for multi-photon transitions is the *ac Stark effect*. Like the static field in the dc Stark effect, the interacting oscillating microwave field induces distortions to the observed atomic spectra due to the ac Stark effect in multi-photon processes. These distortions manifest as energy shifts, energy splitting, and linewidth broadening.

A three-level system with the initial state $|f\rangle$, intermediate state $|m\rangle$, and final state $|r\rangle$

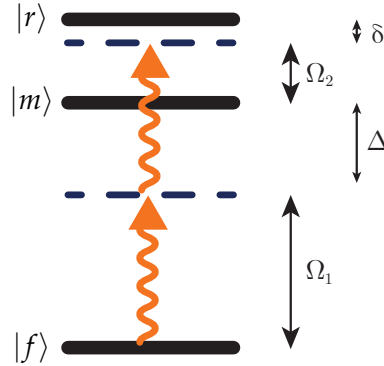


FIGURE 3.5: Illustration of a three-level system and a two-photon transition. The levels of this system include an initial state $|f\rangle$, intermediate state $|m\rangle$, and a final state $|r\rangle$. A photon of energy $E = h\nu$ is absorbed by a virtual state detuned from the $|m\rangle$ intermediate state, and a second photon of energy $E = h\nu$ is absorbed from the virtual state detuned Δ from $|m\rangle$ and driving to the final $|r\rangle$ state. Rabi frequencies Ω_1 and Ω_2 are shown for the $|f\rangle \rightarrow |m\rangle$ and $|m\rangle \rightarrow |r\rangle$ transitions, respectively. Detuning from the $|r\rangle$ state is denoted as δ . Energy level spacing depicted in this figure is not drawn to scale for illustrative purposes.

is considered. A two-photon transition is achieved by first exciting to a virtual intermediate state, which is detuned (Δ) from a real intermediate state $|m\rangle$ and detuned δ from the final state $|r\rangle$. The Hamiltonian of the time-dependent Schrödinger equation for the three-level, single atom for this case in the *rotating wave approximation (RWA)* is given by

$$\mathcal{H} = \begin{pmatrix} 0 & \frac{\Omega_1}{2} & 0 \\ \frac{\Omega_1}{2} & -\Delta & \frac{\Omega_2}{2} \\ 0 & \frac{\Omega_2}{2} & \delta \end{pmatrix} \quad (3.11)$$

where Ω_1 and Ω_2 are the Rabi frequencies for the $|f\rangle \rightarrow |m\rangle$ and $|m\rangle \rightarrow |r\rangle$ transitions, respectively. Detuning from the $|r\rangle$ state is denoted as δ , and is small compared to the detuning of the intermediate state. For this two-photon excitation, the microwaves are far off-resonance from the $|m\rangle$ intermediate state, but close to resonant with the final $|r\rangle$ state.

To provide energy scales for this experiment, the energy separation between the nf

initial state and ng intermediate state is between 11.5 – 17 GHz and the energy separation between the ng and nh final states is between 2.5 – 3.5 GHz, dependent upon n . The detuning from the intermediate ng state for the $nf \rightarrow nh$ transition is between 4 and 6 GHz, also dependent upon n . The two-photon transition for the three-level system in this experiment is depicted in Figure 3.5 with incident photons of energy $E = h\nu$, where h is Planck's constant and ν is the frequency of the applied microwaves.

This three-level system can be reduced to a two-level system using adiabatic elimination where the $|f\rangle$ and $|r\rangle$ states are coupled by an effective off-resonant Rabi frequency (Ω_{eff}), and the $|m\rangle$ state omitted. The effective Rabi frequency is given by

$$\Omega_{eff} = \frac{\Omega_1\Omega_2}{2|\Delta|} \quad (3.12)$$

and can be rewritten in terms of dipole transition matrix elements and the applied microwave electric field [8]. This expression is given by

$$\frac{d_1d_2\mathcal{E}^2}{2\Delta} = \Omega_{eff} \quad (3.13)$$

where d_i are the the dipole transition matrix elements corresponding to the two transitions $|f\rangle \rightarrow |m\rangle$ and $|m\rangle \rightarrow |r\rangle$. The Rabi frequency in Eqn. (3.13) is effectively the two-photon analogy to the single photon case shown in Eqn. (3.4) with the ac Stark shift given by

$$\Delta\omega_{AC} = \frac{\Omega_{eff}^2}{\Delta}. \quad (3.14)$$

The measured frequency ac Stark shift is based on the effective Rabi frequency and the effective detuning from resonance.

Experimentally, the ac Stark shift is observed as a shift in the measured transition frequency as a function of microwave power. To determine the intrinsic transition frequency with no Stark shift, an extrapolation to zero power is performed. Since the power of an

electromagnetic wave scales as \mathcal{E}^2 , extrapolating to zero microwave power is performed by plotting the measured transition frequencies versus applied microwave power and carrying out a least squares linear fit of the data. The y-intercept is thus the extrapolated to zero power intrinsic transition frequency.

3.1.5 Zeeman effect

Another systematic effect and source of uncertainty is considered. The *Zeeman effect* is the splitting and shifting of atomic spectral lines based on an external magnetic field [10]. Considerations for the Zeeman effect must therefore be made to assess the precision and accuracy of spectroscopy measurements. A sufficiently large magnetic field can broaden the observed linewidth of the spectroscopic measurements and limit precision. Additionally, the observed energy levels between atomic states will shift, thus limiting accuracy. Ultimately, the final goal is to attain precise and accurate $ng \rightarrow nh$ and ni spectroscopic measurements for the core polarization calculations.

The predominant magnetic field present in this experimental setup is the Earth's field with a magnitude of approximately 0.5 Gauss. A measurement of the magnetic field at the location of the atoms has been measured with a magnetometer to account for the structural steel of the building. The magnitude of the magnetic field is measured to be 0.4 Gauss. For the purposes of this work, Earth's magnetic field on the order of 0.5 Gauss is considered and accounted for as a systematic uncertainty. Attempts to null this field can be explored in more detail in future work to minimize the Zeeman shifts.

As mentioned previously, the spectral lines are broadened and shifted based on an applied external magnetic field. The energy shift induced by a weak magnetic field is given by the *Landé formula*

$$\Delta E_{nljm_j} = \mu_B B m_j g_j \quad (3.15)$$

where μ_B is the *Bohr magnetron*, B is the applied magnetic field, m_j is the magnetic sublevel quantum number, and g_j is Landé g-factor of the the atom. The *Landé g-factor* is given by

$$g_j = g_\ell \frac{j(j+1) - s(s+1) + \ell(\ell+1)}{2j(j+1)} + g_s \frac{j(j+1) + s(s+1) - \ell(\ell+1)}{2j(j+1)} \quad (3.16)$$

where $g_\ell = 1$ and the *gyromagnetic ratio* of the electron $g_s \approx 2$ [11, 12]. For the higher angular momentum states of interest in this work, the Zeeman shifts are found to be on the energy scales of the fine structure splitting. Therefore this energy scale cannot be regarded as the weak field, and Eqn. (3.15) cannot be accurately used. Instead, experimental measurements of the shifts are performed and used to estimate the systematic uncertainties. These measurements are shown in *Section 3.2.2*.

3.1.6 Lineshape analysis

Observed linewidths are mainly dictated by *transform broadening* due to the microwave field pulse and Zeeman shifts. These effects lead to a lineshape that is not easily characterized. Although this is the case, the lineshapes resemble a Lorentzian and thus for the sake of simplicity, the ionization signal versus frequency-swept microwave pulses is fit to a Lorentzian. Assuming the lineshape is symmetric, this should give an accurate line center which corresponds to the transition frequency between the atomic states. However, there are potential sources of asymmetries, such as the Stark effect and quadratic Zeeman effect. These effects are expected to be less than 10% of the broadening, thus the line center is constrained to be no less than 10% of the linewidth. For the Zeeman effect, the broadening is calculated to be 0.07 MHz for the $f \rightarrow g$ transition, 0.11 MHz for the $f \rightarrow h$ transition, and 0.14 MHz for the $f \rightarrow i$ transition for Earth's magnetic field. For each line center measurement, the uncertainty used is either the statistical line center uncertainty or 10% of the linewidth, whichever is greater. Typically, statistical linewidths are on the order of 10%

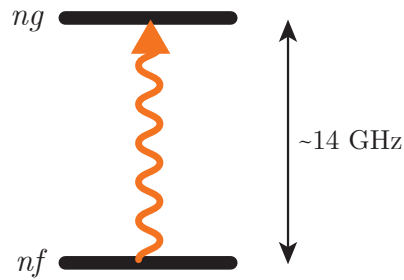


FIGURE 3.6: Illustration of a single photon transition for $nf \rightarrow ng$. A photon of energy $h\nu$ is absorbed driving a transition from the initial bound nf state to the bound ng state.

of the linewidth, with observed linewidths being approximately 1.0 MHz for the $f \rightarrow g$ transition, 1.2 MHz for the $f \rightarrow h$ transition, and 1.5 MHz for the $f \rightarrow i$ transition.

3.2 Single-photon transition

The atomic electronic transition of the nf Rydberg bound state energy level to the ng bound state energy level is characterized as a single photon energy level transition in a two-level system, depicted in Fig. 3.6 with energy

$$\Delta E = h\nu. \quad (3.17)$$

When a microwave field at the resonant frequency ν is applied, the transition is driven and results can be detected using selective and delayed field ionization. Knowing that the initial and final states of the microwave transition have different lifetimes, adjusting delay of the field ionization pulse results in discrimination between the $n\ell$ states. Ionization signals are recorded for $n = 17 - 19 f_{5/2} \rightarrow g_{7/2}$. The typical ionization signals seen for these single-photon transitions are shown in Figure 3.7.

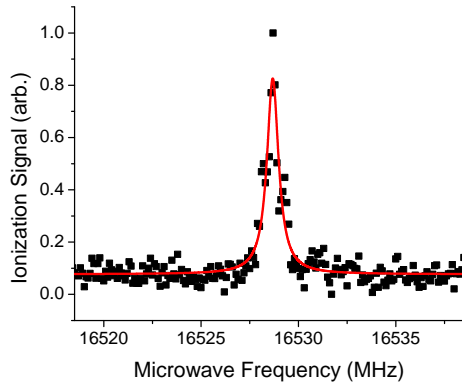
The goal is to achieve accurate and precise measurements of the energy difference between the $nf_{5/2}$ and $ng_{7/2}$ states. To find this transition resonant frequency, the ionization signal amplitude is plotted as a function of microwave frequency. These data are fit to a Lorentzian lineshape, which provides a statistical least squares fit value for the center frequency, full width at half maximum, and amplitude of the signal. Ultimately, the goal is to determine the center frequency as precisely and accurately as possible. Signal-to-noise ratios are approximately 10 for the typical single photon measurement. Lorentzian statistical fits typically yield center frequency uncertainties of 0.05 – 0.1 MHz.

Additional factors must be taken into account when assessing precision and accuracy of these frequency measurements: primarily spectroscopic linewidth broadening and frequency shifts. To account for spectroscopic linewidth broadening due to the Rabi frequency, the microwave power is reduced to where the linewidth is 1 MHz, limited by transform broadening defined by the microwave pulse duration. Frequency shifts are due to the dc Stark effect and Zeeman effect, discussed in the following subsections.

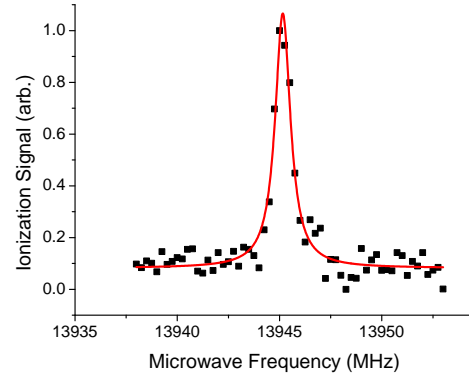
3.2.1 DC Stark shift

Frequency shifts due to the dc Stark effect are minimized by reducing external stray electric fields. Experimentally, this stray electric field is minimized by applying a voltage bias across the electric field plates. As bias voltage of the ionizing electric field is adjusted, an energy shift is observed. A typical dc Stark shift measurement is shown in Figure 3.8 for the $17f_{5/2} \rightarrow 17g_{7/2}$ transition. For this data set, the bias voltage is set to 0.15 V by finding the vertex of the parabola fit; subsequently, the microwave transition frequency at the vertex is 16528.7 MHz.

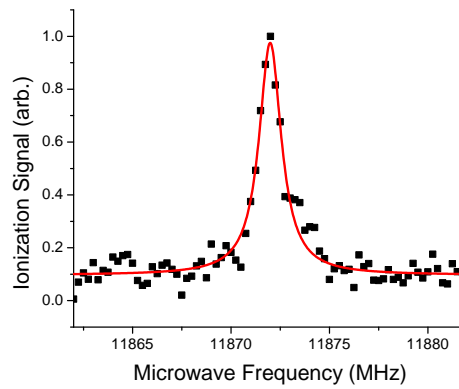
Long-term drifts in the stray electric fields are observed. Time-dependent variations in stray electric fields are considered due to charge buildup on the electric field plates. As a result, dc Stark measurements are conducted at least once per day to account for long-term drifts. Day-to-day drifts are typically 0.25 V/cm corresponding to Stark shifts of the



(A) Typical $17f_{5/2} \rightarrow 17g_{7/2}$ ionization signal centered at 16528 MHz.



(B) Typical $18f_{5/2} \rightarrow 18g_{7/2}$ ionization signal centered at 13945 MHz.



(C) Typical $19f_{5/2} \rightarrow 19g_{7/2}$ ionization signal centered at 11872 MHz.

FIGURE 3.7: Microwaves are swept across atomic resonance and the spectroscopy line profiles are recorded. Shown in these plots are typical ionization signals for $n = 17 - 19 f_{5/2} \rightarrow g_{7/2}$ single photon transitions.

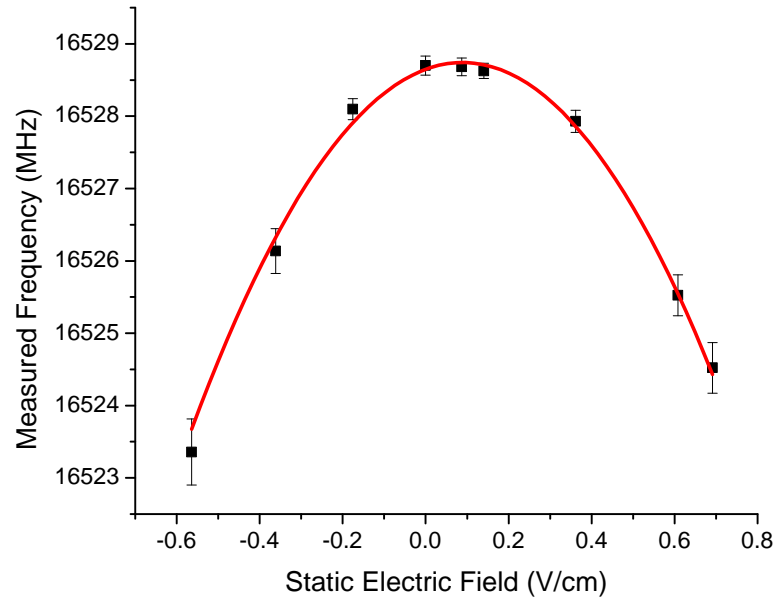


FIGURE 3.8: The dc Stark shift for $17f_{5/2} \rightarrow 17g_{7/2}$ single photon transition in the low electric field regime. A bias voltage is applied to one of the electric field plates corresponding to a static electric field between the plates separated by 1.8 cm. Varying the static electric field amplitude yields a shift in measured transition frequency. The bias field voltage is adjusted to minimize the energy level shift. For this data set, the bias voltage is set to 0.15 V by finding the vertex of the parabola fit; subsequently, the microwave transition frequency at the vertex is 16528.7 MHz.

n	Frequency shift (MHz)
17	0.12
18	0.17
19	0.25

TABLE 3.4: DC Stark shifts are calculated for $n = 17 - 19 f_{5/2} \rightarrow 19g_{7/2}$ with a 0.1 V/cm external electric field. These calculated values correspond to the systematic uncertainty of the dc Stark effect for this experimental apparatus.

$nf \rightarrow ng$ transition on the order of 0.5 MHz.

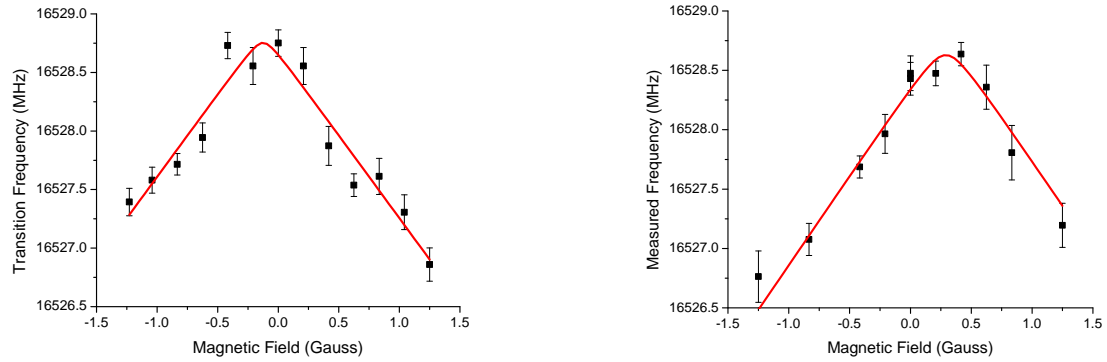
As previously discussed, only control over the longitudinal direction between the electric field plates is possible and transverse fields cannot be compensated. However, previous experiments show that transverse fields are typically below 0.1 V/cm, which corresponds to a shift on the order of the measured statistical uncertainty for each measurement. To account for the systematic uncertainty due to the dc Stark effect, shifts are calculated for the uncontrolled 0.1 V/cm electric field.

The theoretically calculated values are suitable to use in determining systematic uncertainties, when compared to the experimental measurements. The transition polarizability coefficient introduced earlier is determined by the curvature of the parabolic plot fit in Fig. 3.8 relating to the Stark effect equation $\Delta E = -(1/2)\alpha_{fg}\langle\mathcal{E}\rangle^2$. The experimentally determined Stark shift for the $17f_{5/2} \rightarrow 17g_{7/2}$ transition has a transition polarizability coefficient α_{fg} of 23.7 ± 1.2 MHz cm²/V². The lower principal quantum number $n = 17$ was used in these measurements to achieve a lower relative uncertainty since the measurement resolution remains consistent while the energy spacing between these states decreases as n increases. The theoretically calculated value for the transition polarizability coefficient is found to be 23.0 MHz cm²/V². Both the experimental value and the theoretical value agree to within one standard deviation. The calculated values are then used to determine systematic uncertainties. Calculated frequency shifts corresponding to a 0.1 V/cm electric field are shown in Table 3.4.

3.2.2 Zeeman shift

Measurements of Zeeman shifts are performed to determine the systematic uncertainty due to Earth's magnetic field. An external magnetic field is experimentally applied along the axis of the laser beams (X) and perpendicular to the laser beams intersecting at the center of the chamber (Y). Coil forms were designed and 3D printed to slip around and secure to the 8 inch vacuum chamber conflat flanges. The coil form *computer aided design* (CAD) drawing is shown in Appendix E. The magnetic field at the atoms due to the current through the coils is measured with a magnetometer to be 0.42 Gauss/A. The coils are wound to 250 turns, have a radius of approximately 10 cm, and the current through the loop of wire can be varied between 0 A to ± 3 A. This current limit is present due to the bench power supply used. The distance between the coil and the atoms is approximately 30 cm along the X and Y axes. The magnetic field in the X and Y directions can be varied up to approximately 1.25 Gauss, above the 0.5 Gauss magnetic field of Earth. By varying the magnetic field in each of these directions, the significance of the Zeeman effect in this experiment can be deduced.

Measurements of the energy shifts due to the Zeeman effect are performed for the $nf_{5/2} \rightarrow ng_{7/2}$ transition because measurement fidelity is the greatest for this transition compared to the multi-photon transitions. Experimental results for the Zeeman effect are shown in Figure 3.9, with the applied magnetic field along the X direction and along the Y direction in the subplots. A reliable Zeeman shift measurement in the Z direction is not possible with the current apparatus due to the geometry of the vacuum system. Nonetheless, these measurements serve to understand the impact of an observed energy shift as a result of Earth's magnetic field. A frequency shift at no experimentally applied external magnetic field is measured to be approximately 0.1 MHz from the maximal transition frequency, thereby showing that the effect is minimal. This 0.1 MHz frequency shift is thus taken into account and applied as a systematic uncertainty to all of the measurements.



(A) Zeeman shift measurement in the X direction; performed at $n = 17$ for $f_{5/2} \rightarrow g_{7/2}$.

(B) Zeeman shift measurement in the Y direction; performed at $n = 17$ for $f_{5/2} \rightarrow g_{7/2}$.

FIGURE 3.9: Experimental measurements of Zeeman shifts along the X and Y axes for the $17f_{5/2} \rightarrow 17g_{7/2}$ transition. The magnetic fields are produced using a coil of wire along each of the axes: along the axis of the laser beams (X) and perpendicular to the laser beams intersecting at the center of the chamber (Y). The radius of the coil of wire, around the 3D-printed coil form shown in Appendix E, is approximately 10 cm, wound to 250 turns, and the current is varied between 0 A to ± 3 A. Along the X and Y axes, the distance of the coils to the atoms are approximately 30 cm. To determine the nominal shift from no experimentally applied external magnetic field to the maximum transition frequency measured, each of the data in these plots are fit to a function of the form $y = A + B\sqrt{(x - x_0)^2 + a^2}$. A frequency shift at no experimentally applied external magnetic field is measured to be approximately 0.1 MHz from the maximal transition frequency per the fit. Therefore, a 0.1 MHz frequency shift is taken into account and applied as a systematic uncertainty to all of the measurements.

Transition	Measured Transition Frequency (MHz)
$17f_{5/2} \rightarrow 17g_{7/2}$	16528.65 ± 0.03
$17f_{7/2} \rightarrow 17g_{9/2}$	16561.27 ± 0.02

TABLE 3.5: Measured transition frequencies for $17f_{5/2} \rightarrow 17g_{7/2}$ and $17f_{7/2} \rightarrow 17g_{9/2}$ for determination of the fine structure splitting of the $17g_{7/2} - 17g_{9/2}$ states.

3.2.3 Fine structure

Knowledge of the fine structure splittings are necessary to determine whether the ng state is hydrogenic. To determine whether the ng state fine structure of rubidium is hydrogenic, a comparison to the hydrogen fine structure energy splittings is made. In principle, a direct measurement is possible by tuning the first laser pulse to be on resonance with the $5s_{1/2} \rightarrow 6p_{3/2}$ transition. This allows the atoms to decay to the $4d_{3/2}$ and $4d_{5/2}$ states where the next laser pulse drives the atoms to both the $nf_{5/2}$ and $nf_{7/2}$ states since the linewidth of the laser is too broad to resolve fine structure. From here, microwaves can be used to drive the $nf_{7/2} \rightarrow ng_{7/2}$ and $nf_{7/2} \rightarrow ng_{9/2}$ transitions. Using this method and simply calculating the difference between these two measured spectral lines of $ng_{7/2}$ and $ng_{9/2}$ would yield the fine structure splitting and allow for comparison to hydrogen. Unfortunately, a direct measurement of the ng state fine structure splitting is impractical since small Clebsch-Gordan coefficients suppress the $nf_{7/2} \rightarrow ng_{7/2}$ transition compared to the $nf_{7/2} \rightarrow ng_{9/2}$ transition, below an observable level for this experimental setup. Instead an indirect measurement is performed by making a measurement of the $nf_{5/2} \rightarrow ng_{7/2}$ transition followed by the $nf_{7/2} \rightarrow ng_{9/2}$ transition. The measured transition frequencies for $n = 17$ are shown in Table 3.5, with $n = 17$ chosen since the fine structure splitting is the greatest at lower n and will yield the lowest relative uncertainty.

The nf fine structure is known and calculated based on experimental results obtained by Han, *et al.* [3]. Using the extrapolation presented therein, it is found that the nf state fine structure splitting is $17f_{5/2} - 17f_{7/2} = 30.83 \pm 0.02$ MHz. Subtracting this from the

difference between the measurements above yields the fine structure splitting of the g state,

$$E_{g_{7/2} \rightarrow g_{9/2}} = E_{f_{7/2} \rightarrow g_{9/2}} - E_{f_{5/2} \rightarrow g_{7/2}} - E_{f_{5/2} \rightarrow f_{7/2}}.$$

The experimental finding of the fine structure splitting of the $17g$ state is 1.83 ± 0.06 MHz.

Hydrogen fine structure energy shifts are given by

$$\Delta E_{n,\ell,j} = E_0 \frac{\alpha^2}{n^4} \left(\frac{n}{j+1/2} - \frac{3}{4} \right) \quad (3.18)$$

where E_0 is the ground state energy of the hydrogen atom, $\alpha \approx 1/137$ is the fine structure constant, and implementing the fact that $j = \ell \pm 1/2$ for a hydrogen atom. Fine structure splitting for the hydrogen $17g$ state is calculated to be 1.78 MHz. Errors are determined by assigning a 10% uncertainty to the calculated hydrogen fine structure splitting values. Given the measurement of the $17g$ fine structure state above, this estimate should be suitable.

Both the experimental Rb measurement of the ng state fine structure splitting and analytically calculated H ng fine structure splitting are in agreement. Therefore, the rubidium ng state can be regarded as hydrogenic and the spectroscopic measurements of this state subsequently used in the core polarization model.

3.2.4 Spectroscopy results

Upon minimizing the dc Stark shifts, measurements of the $n = 17 - 19$ $f_{5/2} \rightarrow g_{7/2}$ transition frequencies are conducted. The dc Stark effect measurements are plotted and fit to a parabola. The vertex of the parabola is determined corresponding to the static bias voltage set to maximize transition frequency. These measurements are conducted over two days to partially account for systematic effects that take place over a long period of time. Once

n	Measured $nf_{5/2} \rightarrow ng_{7/2}$ Transition Frequency (MHz)
17	16528.66 ± 0.03
18	13945.16 ± 0.09
19	11872.26 ± 0.06

TABLE 3.6: Measured transition frequencies for $n = 17 - 19$ $f_{5/2} \rightarrow g_{7/2}$. Values and errors reported here are from the statistical Lorentzian fits applied to the data sets. Multiple measurements were taken on multiple days and dc Stark shifts minimized for each measurement.

n	Measured $nf_{5/2} \rightarrow ng_{7/2}$ Transition Frequency (MHz)
17	16528.66 ± 0.16
18	13945.16 ± 0.22
19	11872.26 ± 0.28

TABLE 3.7: Measured transitions frequencies for $n = 17 - 19$ $f_{5/2} \rightarrow g_{7/2}$. Values and errors reported here take into account both statistical and systematic uncertainties.

the bias voltage is set corresponding to the vertex of the parabola on a given day, the measurement is repeated at least three times to reduce statistical uncertainty. The final values reported are displayed in Table 3.6.

Error bars are determined by averaging the 5 to 10 measurements in total for each transition gathered on at least two separate days. For each individual measurement, if the measured transition frequency uncertainty is less than 10% of the linewidth per the Lorentzian fit, 10% of the linewidth is assigned as the uncertainty. Additionally, systematic uncertainties from Table 3.4 are applied to account for the dc Stark shift as a result of the unknown 0.1 V/cm electric field in the transverse direction of the electric field plates. The 0.1 MHz Zeeman effect systematic uncertainty is also applied. Measurement results including these systematic uncertainties are shown in Table 3.7.

3.3 Two-photon transition

The atomic electronic transition of the nf Rydberg bound state energy level to the nh bound state energy levels is characterized as a two-photon energy level transition in a multi-level

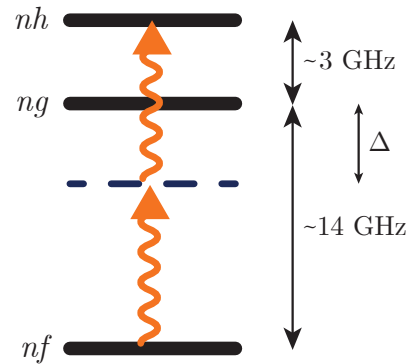


FIGURE 3.10: Illustration of a two-photon transition for $nf \rightarrow nh$. A photon of energy $h\nu$ is absorbed by a virtual state detuned from the ng intermediate state, and a second photon of $h\nu$ being absorbed from the virtual state detuned Δ from ng and driving to the final nh state. Energy level spacing depicted in this figure is not drawn to scale for illustrative purposes.

system, depicted in Fig. 3.10. Shown in the illustration, photons of energy

$$E = h\nu \quad (3.19)$$

are absorbed by a virtual state detuned Δ from the ng intermediate state, and a second photon with energy $E = h\nu$ is absorbed driving to the final nh state.

Detection of the transitions are accomplished through the same process in the single-photon case through selective field ionization. However with the higher- ℓ states, delayed field ionization techniques are also implemented to leverage the longer lifetimes of these states for better experimental signal-to-noise ratios. Discrimination between the $n\ell$ states is achieved through a combination of selective and delayed field ionization techniques.

Just as with the single-photon measurement, the microwave frequency is swept and the ionization signal is recorded for $n = 17 - 19 f_{5/2} \rightarrow h_{9/2}$. A typical ionization signal for the two-photon transition is shown in Figure 3.11. The microwave power is reduced to where the linewidth is $1/\tau = 1$ MHz, limited by the pulse-broadening dictated by microwave pulse duration $\tau = 1 \mu\text{s}$. Observed linewidths are typically near 1 MHz, as expected, upon

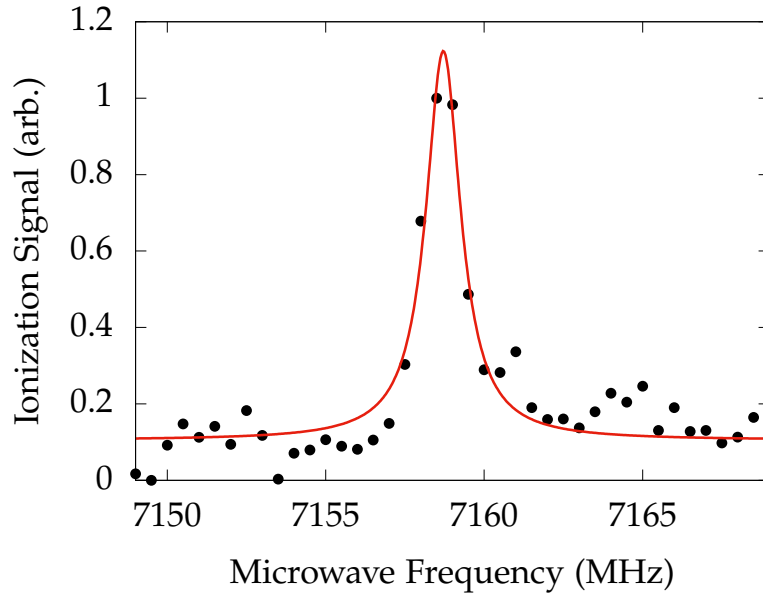


FIGURE 3.11: Typical ionization signal versus microwave frequency for the $19f_{5/2} \rightarrow 19h_{9/2}$ two-photon transition. The microwave field is swept across a range of frequencies and power is set to a value that minimizes spectral linewidth to approximately 1 MHz, like in the single-photon case. However, for $19f_{5/2} \rightarrow 19h_{9/2}$, the applied microwave frequency is half of the transition frequency to facilitate the two photon transition.

reducing microwave power.

3.3.1 DC Stark shift

The dc Stark shifts for multi-photon transitions are measured in the same fashion as in the single-photon case by varying the electric field bias and observing a shift in the energy level of the atomic states. For the higher- ℓ states, dc Stark shifts are more pronounced, as seen in Table 3.3 and Figure 3.4. DC Stark shift measurements were conducted for the $17f_{5/2} \rightarrow 17h_{9/2}$ transition and the results are plotted in Figure 3.12.

Once again, the Stark shift transition polarizability coefficient α_{fh} for $17f_{5/2} \rightarrow 17h_{9/2}$ is compared between the experiment and theory. Upon fitting the parabola in Figure 3.12, the transition polarizability coefficient α_{fh} is experimentally found to be $80 \pm 2 \text{ MHz cm}^2/\text{V}^2$

n	Frequency shift (MHz)
17	0.38
18	0.57
19	0.82

TABLE 3.8: DC Stark shifts are calculated for $n = 17 - 19 f_{5/2} \rightarrow 19h_{9/2}$ with a 0.1 V/cm external electric field. These calculated values correspond to the systematic uncertainty of the dc Stark effect for this experimental apparatus.

with the uncertainty being statistical from the least squares parabolic fit. This is approximately 3 standard deviations larger than the calculated value of $75.4 \text{ MHz cm}^2/\text{V}^2$. This difference can be explained by the fact that additional systematic uncertainties are not considered in this data set. Typically, the bias field minimizing the dc Stark shift is set using measurements of the $nf \rightarrow ng$ transition and data is not typically obtained for $nf \rightarrow nh$. Therefore, the experimentally measured transition polarizability coefficient may not be an accurate representation of the effect for the multi-photon transitions. These values are still close to the calculated values, and the calculated values remain a reasonable representation for determining the systematic uncertainties.

The systematic uncertainties due to the dc Stark effect are handled similarly to the single-photon case with dc Stark shifts calculated for the $n = 17 - 19 nf_{5/2} \rightarrow nh_{9/2}$ transitions at a 0.1 V/cm electric field. The systematic uncertainties as a result of this calculation are tabulated in Table 3.8.

3.3.2 AC Stark shift and spectroscopy results

Upon considering the dc Stark shifts, ac Stark shifts, and spectral distortions, measurements of $n = 17 - 19 f_{5/2} \rightarrow h_{9/2}$ transition frequencies are conducted. The dc Stark effect is taken into account in the same manner as with the single-photon transition. Once dc Stark shifts are minimized, ac Stark shifts are also minimized. Five to ten measurements are conducted at differing microwave powers to perform a least squares linear fit to extrapolate to zero microwave power. A typical ac Stark shift measurement for $19f_{5/2} \rightarrow 19h_{9/2}$

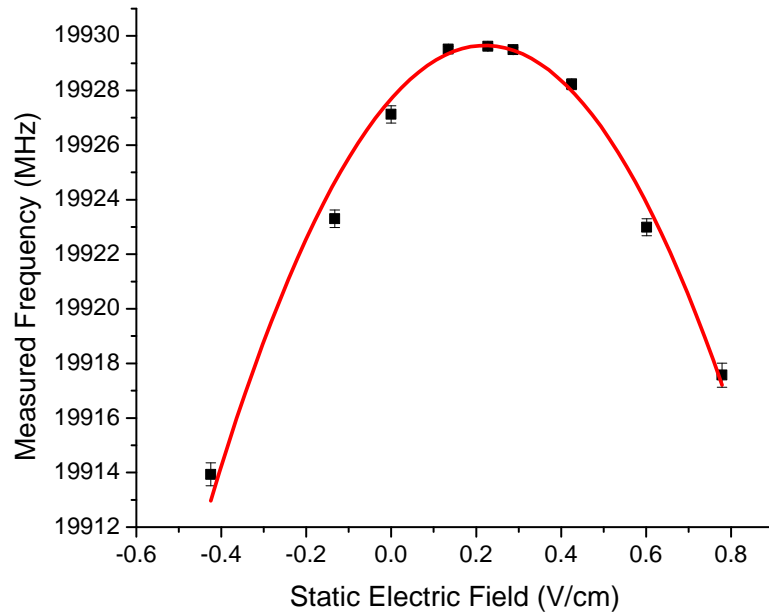


FIGURE 3.12: The dc Stark shift for $17f_{5/2} \rightarrow 17h_{9/2}$ two-photon transition in the low electric field regime. A bias voltage is applied to one of the electric field plates corresponding to a static electric field between the plates separated by 1.8 cm. Varying the static electric field amplitude yields a shift in measured transition frequency. The bias field voltage is adjusted to minimize the energy level shift. For this data set, the bias voltage is set to 0.22 V by finding the vertex of the parabola fit; subsequently, the microwave transition frequency at the vertex is 19929.7 MHz.

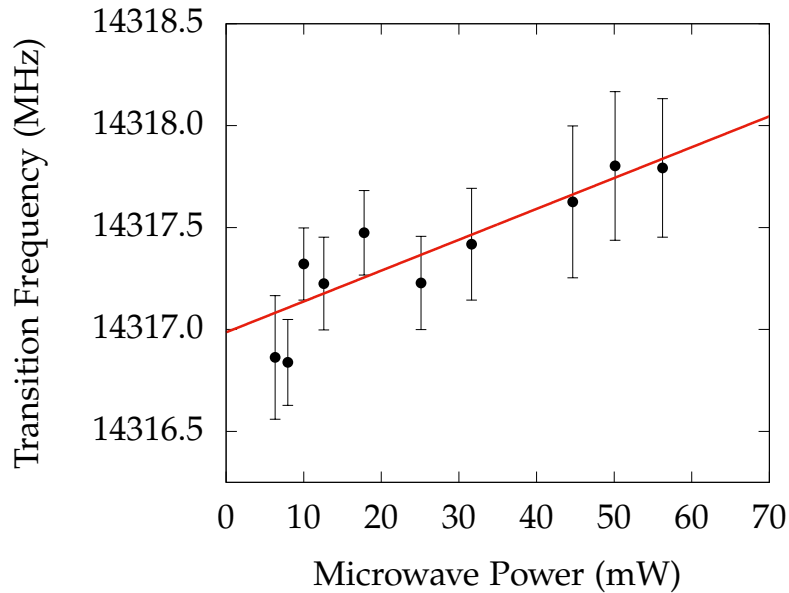


FIGURE 3.13: Typical ac Stark shift measurement for $19f_{5/2} \rightarrow 19h_{9/2}$. An ac Stark shift is observed as a function of microwave power. An extrapolation to zero field is performed to determine the transition frequency with no Stark shift. Since the power of an electromagnetic wave scales as \mathcal{E}^2 , extrapolating to zero field is simply a matter of fitting the measured transition frequency versus microwave power data points to a line and determining the y-intercept. These data are collected for $n = 19$, but the same treatment may apply to $n = 17$ and $n = 18$.

is shown in Figure 3.13.

Uncertainties are determined in a similar manner to the single-photon transition with as little as 10% linewidth uncertainties for each measurement at a given microwave power. The entire data set is fit to a line and a statistical uncertainty is obtained for the y-intercept. Measurement results with statistical uncertainties are presented in Table 3.9. Statistical uncertainties are then added in quadrature with the estimated 0.1 V/cm transverse dc Stark shifts in Table 3.8 and a Zeeman shift of 0.1 MHz. The measurement is typically repeated on a different day to account for slowly-varying effects. The spectroscopic measurements and reported errors are shown and displayed in Table 3.10.

n	Measured $nf_{5/2} \rightarrow nh_{9/2}$ Transition Frequency (MHz)
17	19929.54 ± 0.26
18	16815.55 ± 0.14
19	14316.99 ± 0.13

TABLE 3.9: Measured transition frequencies for $n = 17 - 19$ $f_{5/2} \rightarrow h_{7/2}$. Transition frequencies and errors reported here are due to the statistical Lorentzian fits applied to the data sets. Multiple measurements were taken on multiple days and the dc Stark shifts minimized.

n	Measured $nf_{5/2} \rightarrow nh_{9/2}$ Transition Frequency (MHz)
17	19929.54 ± 0.47
18	16815.55 ± 0.59
19	14316.99 ± 0.84

TABLE 3.10: Measured transitions frequencies for $n = 17 - 19$ $f_{5/2} \rightarrow h_{9/2}$. Values and errors reported here take into account both statistical and systematic uncertainties.

3.4 Three-photon transition

The approach for the four-level $nf \rightarrow ni$ three-photon transition is similar to the $nf \rightarrow nh$ two-photon transition. For this case, there are two virtual intermediate states, each detuned from the real intermediate ng and nh states, with a final rf field applied on resonance with the ni transition. An illustration of this is shown in Figure 3.14. The ac Stark shift follows a similar approach to the two photon description above. With the additional interacting field added to the Hamiltonian, the ac Stark shifts are also additive for both microwave and rf power. Therefore, the the ac Stark shift applied to the measured microwave frequency for the $nf_{5/2} \rightarrow ni_{11/2}$ transition is also fit to a line and shown in Figure 3.17 for $n = 19$. Just as before, this applies to $n = 17$ and $n = 18$ in the same fashion.

Notably, a difference between the two and three-photon cases is the detuning from the nh state. The detuning from the nh state is much less than the detuning from the ng state and an rf signal is applied to excite from the virtual detuned nh state to the ni state. Equations (3.13) and (3.14) show that the ac Stark shift is inversely proportional to

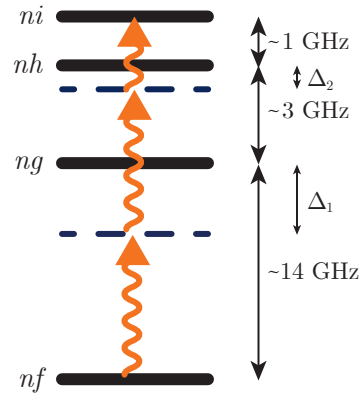


FIGURE 3.14: Illustration of a three-photon transition for $nf \rightarrow ni$. A photon of energy $h\nu$ is absorbed by a virtual state detuned from the ng intermediate state, and a second photon with energy $h\nu$ excites to another virtual intermediate state detuned from nh . Finally, the applied rf field drives the transition from the virtual state detuned from nh to the final ni state. The dashed lines in the illustration depict virtual states. Energy level spacings depicted in this figure are not drawn to scale for illustrative purposes, but labeled to express energy scales.

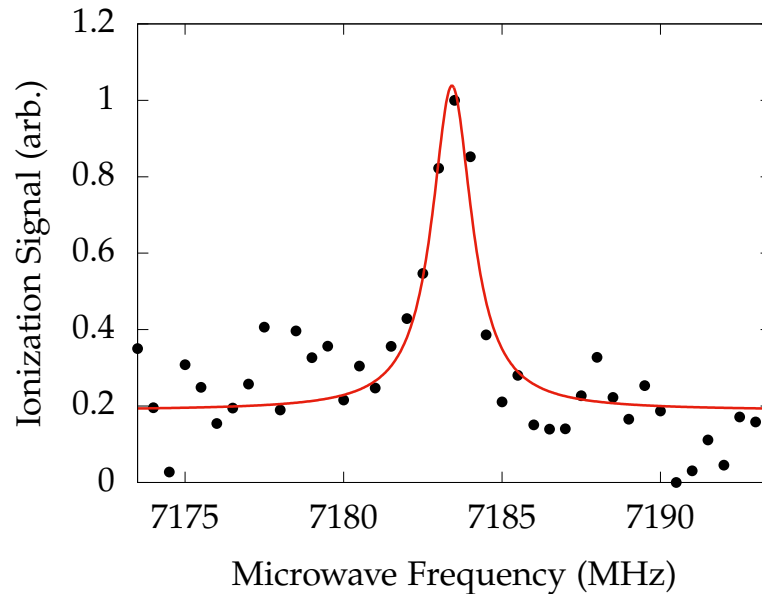


FIGURE 3.15: Typical ionization signal versus microwave frequency for a $19f_{5/2} \rightarrow 19i_{11/2}$ three-photon transition. Applied microwave frequency is half of the transition frequency detuned from the $19h_{9/2}$ virtual state with a constant rf field at 1015 Mhz.

detuning, with the three-photon energy shift given by

$$\Delta\omega_{AC} = \frac{\Omega_1^2}{\Delta_1} + \frac{\Omega_2^2}{\Delta_2} \quad (3.20)$$

where the 1 subscript denotes the effective Rabi frequency and detuning corresponding to the microwave driven nf to detuned nh virtual state, and the 2 subscript denotes the effective Rabi frequency and detuning corresponding to the rf driven detuned nh to resonant ni state. These ac Stark shifts are additive since each field Hamiltonian component is treated separately and added. Due to the detuning from the nh state being much less than the detuning from the ng state, the ac Stark shift measurements are more pronounced for an applied rf power compared to microwave power. This effect can be readily seen by comparing the two plots in Figure 3.17.

The $nf \rightarrow ni$ spectroscopy measurement is typically repeated four times, with two measurements taken for detunings on either side of the nh state resonance. For a single measurement, the rf frequency remains constant corresponding to the detuned nh virtual state to the target ni state and the microwave frequency is swept with a resonance measured at half of the frequency of the two-photon nf to nh detuned virtual state. Each measurement is taken at a detuning of at least ± 50 MHz from the nh state to avoid the effects of measurements on-resonance. Extrapolations to zero microwave and rf power are performed for each of these measurements to determine the true transition frequency. Another methodology can be employed where the microwave frequency remains constant and the rf frequency is swept. However, given the poor impedance matching of the rf output to the electric field plate in the current experimental setup, the rf power at the atoms may fluctuate as the rf frequency is varied leading to an uncertainty. Therefore, the microwave frequency is varied as the rf frequency remains constant for these measurements.

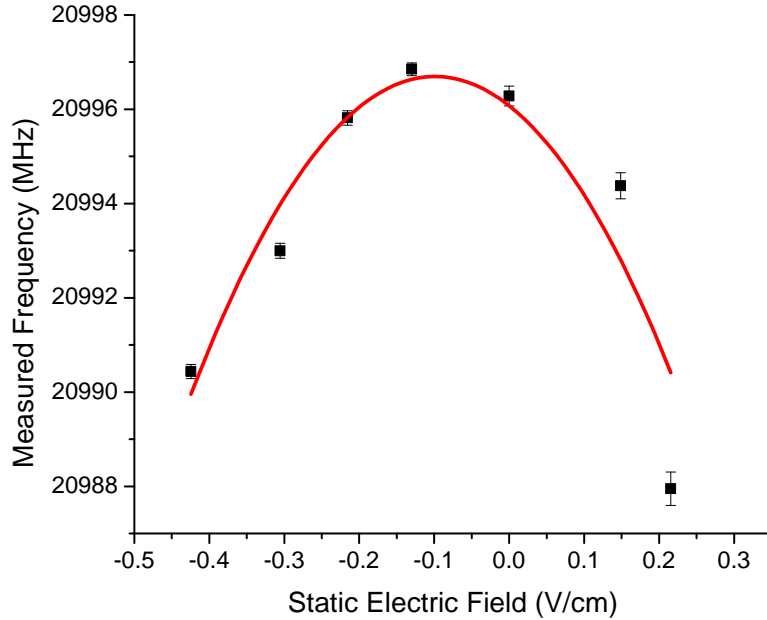


FIGURE 3.16: The dc Stark shift for $17f_{5/2} \rightarrow 17i_{11/2}$ three-photon transition in the low electric field regime. A bias voltage is applied to one of the electric field plates corresponding to a static electric field between the plates separated by 1.8 cm. Varying the static electric field amplitude yields a shift in measured transition frequency. The bias field voltage is adjusted to minimize the energy level shift. For this data set, the bias voltage is set to -0.15 V by finding the vertex of the parabola fit; subsequently, the microwave transition frequency at the vertex is 20997.0 MHz.

3.4.1 DC Stark shift

Similar to the single and two-photon transition cases, dc Stark shift measurements were conducted for the $17f_{5/2} \rightarrow 17i_{11/2}$ transition and the results are plotted in Figure 3.16. Systematic uncertainties due to the dc Stark effect are handled similarly to the single and two-photon cases with dc Stark shifts calculated for the $n = 17 - 19$ $nf_{5/2} \rightarrow ni_{11/2}$ transitions at a 0.1 V/cm electric field. The results of this calculation are tabulated in Table 3.11.

Once again, the Stark shift transition polarizability coefficient α_{fi} for the $17f_{5/2} \rightarrow$

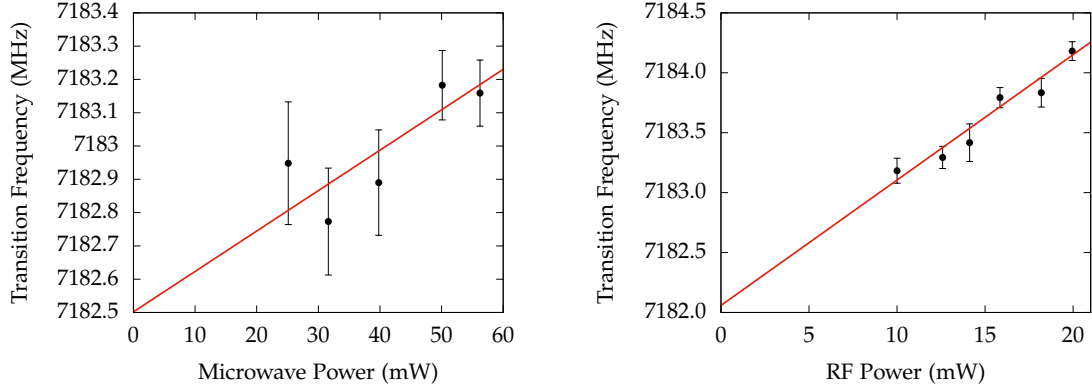
n	Frequency shift (MHz)
17	0.72
18	1.09
19	1.58

TABLE 3.11: DC Stark shifts are calculated for $n = 17 - 19 f_{5/2} \rightarrow 19i_{9/2}$ with a 0.1 V/cm external electric field. These calculated values correspond to the systematic uncertainty of the dc Stark effect for this experimental apparatus.

$17i_{11/2}$ transition is compared between the experiment and theory. Upon fitting the parabola in Figure 3.16, the transition α_{fi} is experimentally found to be $130 \pm 4 \text{ MHz cm}^2/\text{V}^2$. This measurement is found to be just below 4 standard deviations of the calculated value of $145 \text{ MHz cm}^2/\text{V}^2$. Systematic uncertainties are not accounted for in this measurement, and dc Stark shift measurements are not typically performed for multi-photon transitions. Nevertheless, since the $17f_{5/2} \rightarrow 17g_{7/2}$, $17f_{5/2} \rightarrow 17h_{9/2}$, and $17f_{5/2} \rightarrow 17i_{11/2}$ are reasonably close to the theoretical calculations, it can be concluded that calculated dc Stark shifts are sufficient to estimate the systematic uncertainties for each of these transitions. The calculated systematic uncertainties as a result of a 0.1 V/cm dc Stark shift are shown in Table 3.11.

3.4.2 AC Stark shift and spectroscopy results

Similar considerations for $nf_{5/2} \rightarrow ni_{11/2}$ are made as with $nf_{5/2} \rightarrow nh_{9/2}$. However, there are now two ac Stark shifts – one from each detuned virtual state. Measurements are taken on at least two separate days with dc Stark shifts minimized on each day. Typically two measurements are conducted with detunings on either side of the nh resonance, totaling four separate measurements. Uncertainties are determined in a similar fashion to the two-photon case with the linear fit extrapolations to zero microwave and rf power, and adding the error of a possible transverse electric field of 0.1 V/cm corresponding dc Stark shifts. The spectroscopic measurements with statistical uncertainties are reported and displayed in Table 3.12 and measurements with systematic uncertainties shown in Table 3.13.



(A) Typical ac Stark shift measurement for $19f_{5/2} \rightarrow 19i_{11/2}$. The ac Stark shift is measured as a function of microwave power with rf power left at a constant 20 mW. The fit y-intercept is 7182.5 ± 0.1 MHz and the fit slope is 0.012 ± 0.005 MHz/mW.

(B) Typical ac Stark shift measurement for $19f_{5/2} \rightarrow 19i_{11/2}$. The ac Stark shift is measured as a function of rf power with microwave power left at a constant 50 mW. The fit y-intercept is 7182.1 ± 0.2 MHz and the fit slope is 0.10 ± 0.01 MHz/mW.

FIGURE 3.17: Typical ac Stark shift measurements for $19f_{5/2} \rightarrow 19i_{11/2}$ with respect to microwave and rf power. An extrapolation to microwave and rf power are performed to determine the transition frequency with no Stark shift. As with the microwave case, rf power scales as \mathcal{E}^2 so an extrapolation to a zero power is accomplished through a linear fit and finding the y-intercept. These data are collected for $n = 19$, but the same treatment may apply to $n = 17$ and $n = 18$. Due to the detuning from the nh state being much less than the detuning from the ng state, the ac Stark shift is more pronounced for the applied rf field.

n	Measured $nf_{5/2} \rightarrow ni_{11/2}$ Transition Frequency (MHz)
17	20992.54 ± 0.62
18	17713.23 ± 0.56
19	15082.91 ± 0.84

TABLE 3.12: Measured transitions frequencies for $n = 17 - 19 f_{5/2} \rightarrow i_{7/2}$. Values and errors reported here are on the statistical Lorentzian fits applied to the data sets, followed by the ac Stark shift measurements and an extrapolation to zero microwave power and zero rf power. Measurements are taken on at least two separate days with dc Stark shifts minimized on each day. Typically two measurements are conducted with detunings of at least 50 MHz on either side of the nh resonance, totaling four separate measurements.

n	Measured $n f_{5/2} \rightarrow n i_{11/2}$ Transition Frequency (MHz)
17	20992.5 ± 1.0
18	17713.2 ± 1.2
19	15082.9 ± 1.8

TABLE 3.13: Measured transitions frequencies for $n = 17 - 19$ $f_{5/2} \rightarrow i_{11/2}$. Values and errors reported here take into account both statistical and systematic uncertainties.

n	$f_{5/2} \rightarrow g_{7/2}$	$f_{cg} \rightarrow g_{cg}$	$f_{5/2} \rightarrow h_{9/2}$	$f_{cg} \rightarrow h_{cg}$	$f_{5/2} \rightarrow i_{11/2}$	$f_{cg} \rightarrow i_{cg}$
17	16528.66(3)	16547.27(7)	19929.5(3)	19947.8(3)	20992.5(6)	21010.6(6)
18	13945.16(9)	13960.90(10)	16815.6(1)	16831.0(2)	17713.2(6)	17728.5(6)
19	11872.25(6)	11885.69(7)	14317.0(1)	14330.2(1)	15082.9(8)	15096.0(8)

TABLE 3.14: Measured transition frequencies for the measured $f_{5/2} \rightarrow g_{7/2}$, $f_{5/2} \rightarrow h_{9/2}$, and $f_{5/2} \rightarrow i_{11/2}$ transitions are tabulated, along with the the frequencies referenced to the center of gravity of the fine structure doublet with the "cg" notation. Transition frequencies shown here are in MHz. Uncertainties are statistical and cg calculations include the uncertainties pertaining to knowledge of fine structure splittings [3].

3.5 Summary of results

Measured transition frequencies are summarized, along with center of gravity calculations and systematic uncertainties. Center of gravity transition frequencies are used in the core polarizability analysis, as described earlier. Shown in Table 3.14 are the measured transition frequencies for $n = 17 - 19$ $f_{5/2} \rightarrow g_{7/2}$, $f_{5/2} \rightarrow h_{9/2}$, and $f_{5/2} \rightarrow g_{11/2}$ and the calculated center of gravity transition frequencies $f_{cg} \rightarrow g_{cg}$, $f_{cg} \rightarrow h_{cg}$, and $f_{cg} \rightarrow i_{cg}$. Center of gravity transition frequencies after taking into account systematic uncertainties due to the dc Stark effect and Zeeman effect are shown in Table 3.15. These transition frequencies are used in the core polarization model analysis with systematic uncertainties considered.

n	$f_{cg} \rightarrow g_{cg}$	$f_{cg} \rightarrow h_{cg}$	$f_{cg} \rightarrow i_{cg}$
17	16547.3(2)	19947.8(5)	21010.6(10)
18	13960.9(2)	16831.0(6)	17728.5(12)
19	11885.7(3)	14330.2(8)	15096.0(18)

TABLE 3.15: Transition frequencies calculated for the center of gravity of the fine-structure doublet with the "cg" notation. Systematic uncertainties are considered, for use in the core polarization model. Transition frequencies shown here are in MHz for $n = 17 - 19$, $f_{cg} \rightarrow g_{cg}$, $f_{cg} \rightarrow h_{cg}$, and $f_{cg} \rightarrow i_{cg}$.

References

- [1] M. S. Safronova, W. R. Johnson, and A. Derevianko. "Relativistic many-body calculations of energy levels, hyperfine constants, electric-dipole matrix elements, and static polarizabilities for alkali-metal atoms". en. In: *Physical Review A* 60.6 (Dec. 1999), pp. 4476–4487. ISSN: 1050-2947, 1094-1622. DOI: [10.1103/PhysRevA.60.4476](https://doi.org/10.1103/PhysRevA.60.4476). URL: <https://link.aps.org/doi/10.1103/PhysRevA.60.4476> (visited on 06/02/2020).
- [2] V. A. Dzuba et al. "Revisiting Parity Nonconservation in Cesium". en. In: *Physical Review Letters* 109.20 (Nov. 2012), p. 203003. ISSN: 0031-9007, 1079-7114. DOI: [10.1103/PhysRevLett.109.203003](https://doi.org/10.1103/PhysRevLett.109.203003). URL: <https://link.aps.org/doi/10.1103/PhysRevLett.109.203003> (visited on 06/08/2020).
- [3] Jianing Han et al. "Rb n f quantum defects from millimeter-wave spectroscopy of cold Rb 85 Rydberg atoms". en. In: *Physical Review A* 74.5 (Nov. 2006), p. 054502. ISSN: 1050-2947, 1094-1622. DOI: [10.1103/PhysRevA.74.054502](https://doi.org/10.1103/PhysRevA.74.054502). URL: <https://link.aps.org/doi/10.1103/PhysRevA.74.054502> (visited on 06/03/2020).
- [4] L. A. M. Johnson. "Precision laser spectroscopy of rubidium with a frequency comb". In: 2011.
- [5] R. M. Sternheimer, J. E. Rodgers, and T. P. Das. "Effect of the atomic core on the fine-structure splitting for excited nd and nf states of the alkali-metal atoms". en. In: *Physical Review A* 17.2 (Feb. 1978), pp. 505–512. ISSN: 0556-2791. DOI: [10.1103/PhysRevA.17.2](https://doi.org/10.1103/PhysRevA.17.2)

- [PhysRevA.17.505](https://link.aps.org/doi/10.1103/PhysRevA.17.505). URL: <https://link.aps.org/doi/10.1103/PhysRevA.17.505> (visited on 06/15/2020).
- [6] J Stark. “Beobachtungen uber den Effekt des elektrischen Feldes auf Spektrallinien i. Quereffekt”. In: *Annalen der Physik* 50.489 (1914).
- [7] Myron L. Zimmerman et al. “Stark structure of the Rydberg states of alkali-metal atoms”. en. In: *Physical Review A* 20.6 (Dec. 1979), pp. 2251–2275. ISSN: 0556-2791. DOI: [10.1103/PhysRevA.20.2251](https://doi.org/10.1103/PhysRevA.20.2251). URL: <https://link.aps.org/doi/10.1103/PhysRevA.20.2251> (visited on 06/18/2020).
- [8] Thomas F. Gallagher. *Rydberg atoms*. Digitally printed 1st pbk. version. Cambridge monographs on atomic, molecular, and chemical physics 3. Cambridge ; New York: Cambridge University Press, 2005. ISBN: 978-0-521-02166-1.
- [9] NCEI Geomagnetic Modeling Team and British Geological Survey. *World Magnetic Model 2020*. NOAA National Centers for Environmental Information, 2019. DOI: [10.25921/11V3-DA71](https://doi.org/10.25921/11V3-DA71). URL: <https://www.ncei.noaa.gov/metadata/geoportal/rest/metadata/item/gov.noaa.ngdc:WMM2020/html>.
- [10] Pieter Zeeman. “Verhandlungen der Physikalischen Gesellschaft zu Berlin”. de. In: *Annalen der Physik* 284.1 (1893), A773–A784. ISSN: 00033804, 15213889. DOI: [10.1002/andp.18922840119](https://doi.org/10.1002/andp.18922840119). URL: <http://doi.wiley.com/10.1002/andp.18922840119> (visited on 06/21/2020).
- [11] A. Lande. “Uber den anomalen Zeemaneffekt (Teil I)”. de. In: *Zeitschrift fur Physik* 5.4 (July 1921), pp. 231–241. ISSN: 1434-6001, 1434-601X. DOI: [10.1007/BF01335014](https://doi.org/10.1007/BF01335014). URL: <http://link.springer.com/10.1007/BF01335014> (visited on 06/21/2020).
- [12] Stefan Procopiu. “Sur les elements d’energie”. In: *Annales scientifiques de l’Universite de Jassy* 7.280 (1911).

4 | Ionic dipole and quadrupole core polarizabilities

4.1 Core polarization model

Improved spectroscopic measurements between high-lying ℓ states has been achieved compared to previous work. These spectroscopic measurements are relative to the $nf_{5/2}$ state, and thus these measurements cannot be used to calculate the absolute energy of the state relative to the ionization energy. If absolute energies of the states were known, polarizability could be determined using the ideas presented in the Introduction. Previously determined state energies for the nf states can be used to calculate core polarizability, with a similar approach seen in Ref. [1]. The energy shifts in Eqn. (4.2) correspond to the energy shift from hydrogen due to core polarization and are related to quantum defects and absolute energy level values compared to hydrogen. In the absence of core penetration and core polarization, the Rydberg energies are the same as hydrogen, up to a small mass correction. Unfortunately, sufficiently accurate energy measurements of the nf states are not available, thus a comparison to hydrogenic values is not possible. A second, more self-contained approach is taken here whereby relative spectroscopic results are used to calculate core polarization, and quantum defects are then extracted from the core polarizability results.

4.1.1 Theory

Reiterated from the Introduction, applying the core polarization model first introduced by Born, a Rydberg electron with sufficiently high- ℓ orbiting an alkali metal atom ionic core exhibits minimal core penetration allowing for core polarization to be measured [2, 3]. The electrostatic interaction between the Rydberg electron and the alkali metal atom ionic core exhibits mainly the core polarization effect due to the field of the valence electron polarizing the ionic core, leading to an energy shift. The resulting energy shift is a reduction of the observed energy spectrum when compared to hydrogen

$$W_{n\ell} = -\frac{1}{2n^2} + W_{pol}, \quad (4.1)$$

expressed in atomic units. In this model, the energy level for a given $n\ell$ state can be expressed in terms of the hydrogen energy level $-1/(2n^2)$ and the core polarization effect shift to the hydrogen energy level

$$W_{pol} = -\frac{\alpha_d}{2} \langle r^{-4} \rangle_{n\ell} - \frac{\alpha_q}{2} \langle r^{-6} \rangle_{n\ell}. \quad (4.2)$$

Using the relative energy difference between two states of an alkali metal atom with different angular momentum and a given principal quantum number, $n\ell$ and $n\ell'$, the polarization energy difference can be expressed as

$$\Delta W_{n\ell\ell'} = W_{pol_{n\ell'}} - W_{pol_{n\ell}}. \quad (4.3)$$

The approach presented by Edlén in Ref [4] is followed to evaluate dipole and quadrupole polarizability terms, α_d and α_q . The expectation values $\langle r^{-4} \rangle_{n\ell}$ and $\langle r^{-6} \rangle_{n\ell}$ correspond to the hydrogen wavefunction, dependent on n and ℓ . The hydrogen wavefunction is used to approximate these expectation values since the states investigated are non-penetrating.

The analytical expressions to these expectation values are given by

$$\langle r^{-4} \rangle = G_4(n, \ell) [3n^2 - f_1(\ell)] \quad (4.4)$$

and

$$\langle r^{-6} \rangle = 3G_6(n, \ell) \left\{ \frac{35}{3}n^4 - 10n^2 \left[f_1(\ell) - \frac{5}{6} \right] + f_2(\ell) \right\} \quad (4.5)$$

where $G_P(n, \ell)$ and $f_r(\ell)$ are

$$G_P(n, \ell) = \frac{2^P Z^P (2\ell - P + 2)!}{n^{P+1} (2\ell + P - 1)!} \quad (4.6)$$

and

$$f_r(\ell) = \frac{(\ell + r)!}{(\ell - r)!} \quad (4.7)$$

with Z being the nuclear charge; and for hydrogen, $Z = 1$. These analytical solutions are presented in Ref. [5] with additional analytical expressions for expectation values $\langle r^s \rangle$ shown in Appendix C.

By introducing two new variables dependent the expectation values, polarizability can be expressed in terms of a line. These variables are defined as

$$P_{n\ell} = \langle r^{-4} \rangle_{n\ell} \quad (4.8)$$

and

$$Q_{n\ell} = \frac{\langle r^{-6} \rangle_{n\ell}}{\langle r^{-4} \rangle_{n\ell}}. \quad (4.9)$$

Substituting these values into Eqn. (4.2) yields the following equation

$$\Delta W = \alpha_d (P_{n\ell} - P_{n\ell'}) + \alpha_q (P_{n\ell} Q_{n\ell} - P_{n\ell'} Q_{n\ell'}) \quad (4.10)$$

which can then be expressed in a more compact fashion following the presentation by Safinya, *et al.* in Ref [6], as

$$\Delta W = \alpha_d \Delta_d + \alpha_q \Delta_q \quad (4.11)$$

where

$$\Delta_d = P_{n\ell} - P_{n\ell'} \quad (4.12)$$

and

$$\Delta_q = P_{n\ell} Q_{n\ell} - P_{n\ell'} Q_{n\ell'}. \quad (4.13)$$

Using hydrogen wavefunctions and analytically calculated expectation values, both Δ_d and Δ_q are known. The resulting expression takes the form of a line when dividing each side of Eqn. (4.11) by Δ_d .

$$\frac{\Delta W}{\Delta_d} = \alpha_d + \alpha_q \frac{\Delta_q}{\Delta_d} \quad (4.14)$$

The polarization energy, ΔW is obtained through spectroscopic measurements corresponding to the center of gravity transition frequencies shown in Table 3.14. Therefore, with two ΔW measurements, this becomes a matter of solving the two equations for the two unknowns α_d and α_q .

4.1.2 Results and analysis

Given Eqn. (4.14), just two pairs of $n\ell \rightarrow n\ell'$ state spectroscopic measurements are necessary to fit to a line. Once the data points are fit to a line, dipole and quadrupole polarizabilities are the intercept and slope of the resulting fit. For this, the observed difference in the $n\ell \rightarrow n\ell'$ energy levels in this analysis are $ng_{cg} \rightarrow nh_{cg}$ and $nh_{cg} \rightarrow ni_{cg}$ are used since core penetration effects are minimal and core polarization effects are dominant for $\ell \geq 4$. As a reminder, transition frequencies involving nf states cannot be used since core penetration effects are present and thus non-hydrogenic. These two pairs of $n\ell \rightarrow n\ell'$ transitions are plotted and shown in Figure 4.1, with the data points listed in Table 4.1. Upon plotting,

n	Transition	$\Delta_q/\Delta_d (\times 10^{-2})$	$2\Delta W/\Delta_d$
$n = 17$	$g \rightarrow h$	1.28587	9.3046(7)
	$h \rightarrow i$	0.52185	9.159(5)
$n = 18$	$g \rightarrow h$	1.29104	9.3053(10)
	$h \rightarrow i$	0.52508	9.157(7)
$n = 19$	$g \rightarrow h$	1.29540	9.3067(17)
	$h \rightarrow i$	0.52781	9.168(12)

TABLE 4.1: Determination of core polarizabilities in the adiabatic approximation. In the main plot, ΔW is the measured energy interval between states $n\ell$ and $n\ell'$. The parameters Δ_d and Δ_q depend on n, ℓ and ℓ' , and are given by Eqns. (4.12) and (4.13). The side plots show expanded views of the data for the (a) $g - h$ and (b) $h - i$ transitions. The line is an error-weighted best fit, with intercept and slope corresponding to α_d and α_q , respectively. The present values are $\alpha_d = 9.059(6) a_0^3$ and $\alpha_q = 19.1(5) a_0^5$.

these data are fit to a line using the least squares method. The resulting intercept and slope of the fit to the line are $\alpha_d = 9.059(6) a_0^3$ and $\alpha_q = 19.1(5) a_0^5$, respectively. Uncertainties reported here are a result of the statistical fit of the line best fit to the data with errors weighted. Systematic uncertainties, such as lineshape of the spectrum, are accounted for prior to plotting the data. This analysis neglects the non-adiabatic correction that plays an important role in accurate polarizability results, and that will be discussed later in this chapter.

4.1.3 Comparison to previous work

The polarizability measurements here are in reasonable agreement with previous experimental work. Previous measurements yielded dipole and quadrupole polarizabilities of $\alpha_d = 9.12(2) a_0^3$ and $\alpha_q = 14(3) a_0^5$ [1], with the core polarizability plot provided in the reference shown in Figure 4.2. The dipole polarizability results agree to within three standard deviations with the previous measurement and quadrupole polarizabilities agree within two standard deviations. However, results reported here are approximately 6 times more precise for the dipole polarizability term and an order of magnitude more precise for the quadrupole polarizability term.

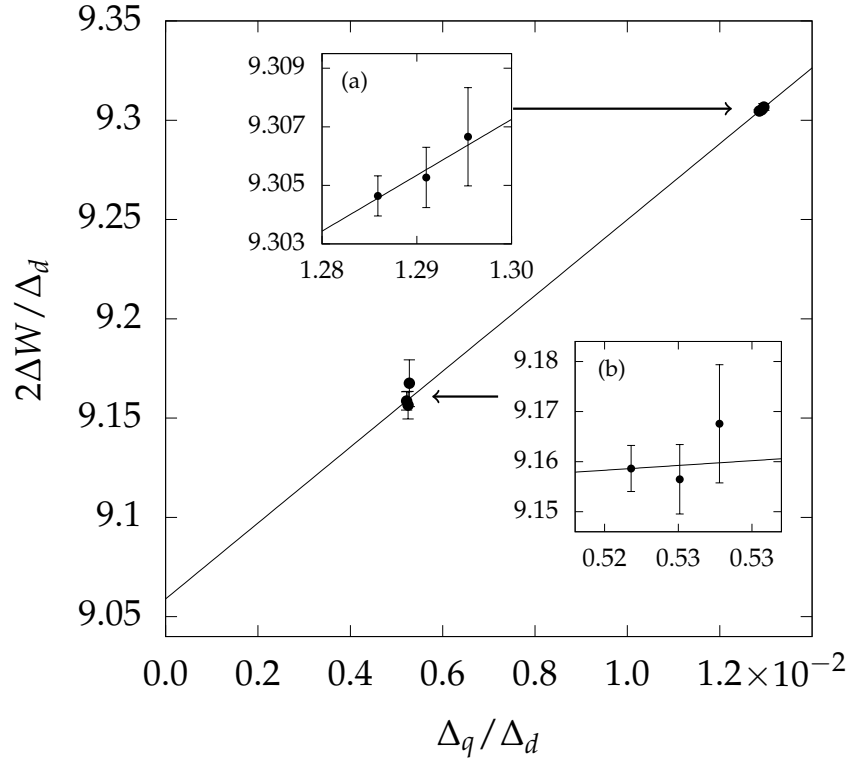


FIGURE 4.1: Determination of core polarizabilities in the adiabatic approximation. In the main plot, ΔW is the measured energy interval between states $n\ell$ and $n\ell'$. The parameters Δ_d and Δ_q depend on n , ℓ and ℓ' , and are given by Eqs. (4.12) and (4.13). The side plots show expanded views of the data for the (a) $g-h$ and (b) $h-i$ transitions. For the inset plots, the horizontal axis is more expanded than the vertical axis to better show the different n measurements and uncertainties. As drawn, this difference in scales leads to an apparent change in slope. The line is an error-weighted best fit, with intercept and slope corresponding to α_d and α_q , respectively. The present values are $\alpha_d = 9.059(6) a_0^3$ and $\alpha_q^{(a)} = 19.1(5) a_0^5$.

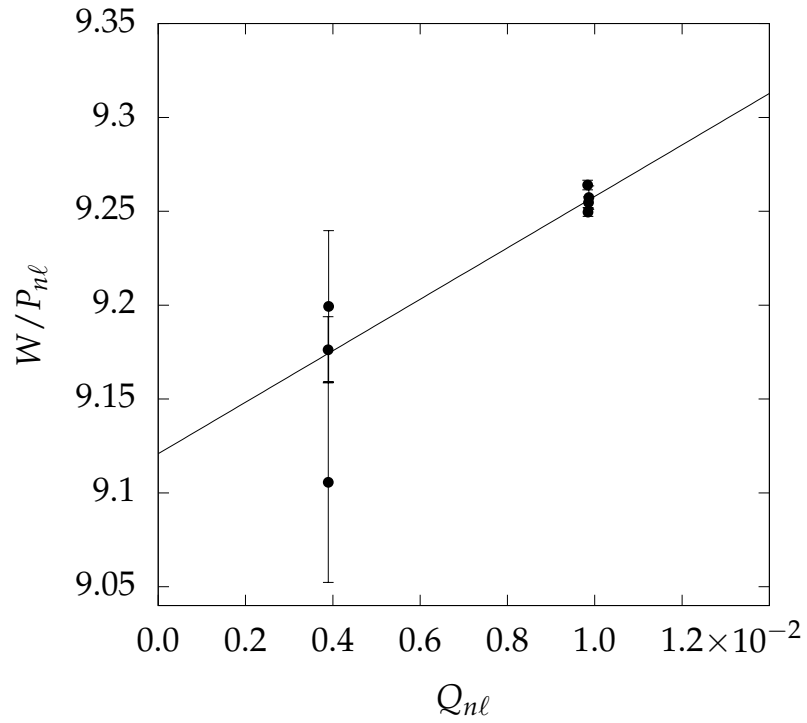


FIGURE 4.2: Previous core polarizability measurement reported by Lee, *et al.* in Ref [1]. Therein, measurements of $(n+1)d_{5/2} \rightarrow nf, ng$ are performed for $n = 27 - 30$. Core polarizability is extracted from the quantum defects reported and plot, then fit to a line with least squares. The resulting fit parameters are $\alpha_d = 9.12(2) a_0^3$ and $\alpha_q = 14(3) a_0^5$.

When considering theory, dipole and quadrupole polarizabilities are calculated to be $\alpha_d = 9.1 a_0^3$ and $\alpha_q = 34 a_0^5$ [7]. No error bars are provided by the theory calculation, but the dipole polarizability appears to be within reasonable agreement with this and the previous experiment. However, a large discrepancy is present for the quadrupole polarizability term when comparing these theoretical values to the experimental results found here. This discrepancy has been previously noted by Lee, *et al.* as a motivation for future work [1]. And, this discrepancy has been resolved by considering non-adiabatic effects.

4.2 Non-adiabatic core polarization model

The core polarizability analysis presented earlier uses the adiabatic approximation. The polarization energy in the adiabatic approximation does not account for the motion of the valence electron, and an associated polarization energy shift. In an effort to resolve the quadrupole polarizability value discrepancy between experiment and theory and to obtain the most best value for the dipole polarizability, a non-adiabatic effect is applied to the core polarization model. This approach has been used previously for alkaline earth atoms, but was not thought to be necessary for alkali atoms. To the contrary, however, it is found in this work that the non-adiabatic correction is quite significant for Rb.

4.2.1 Theory

The core polarization model presented by Mayer and Mayer derives the energy shift from the polarization of the atom core for an alkali metal atom using perturbation theory [3]. However, the *non-adiabatic effect* due to the motion of the valence electron is not considered. In the treatment by van Vleck and Whitelaw that is followed here [8, 9, 10, 11], an energy correction due to possible excitation of the core electrons is included in the derivation of polarization energy using perturbation theory. The second-order correction to the polarization energy involves a sum over all states including the core, Rydberg bound states, and

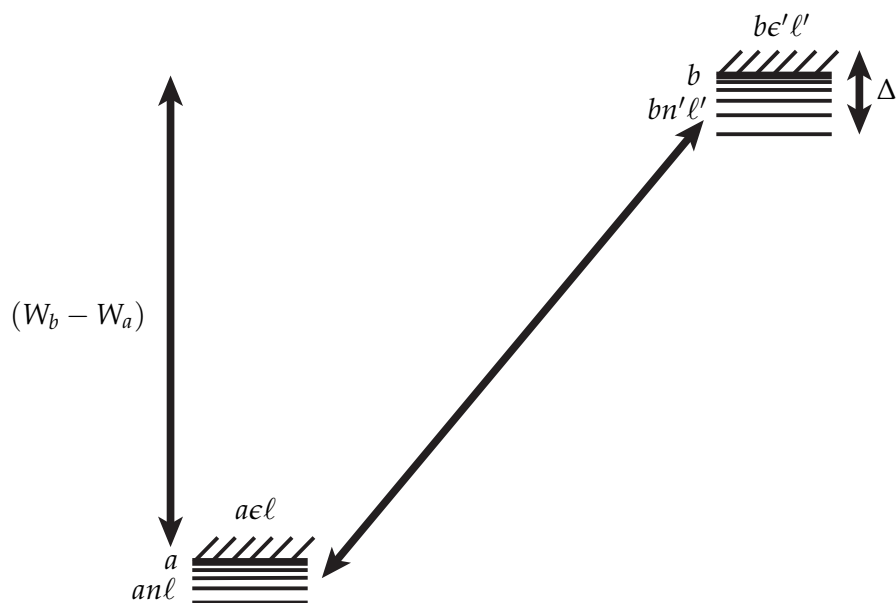


FIGURE 4.3: Energy level diagram showing ion states a and b , Rydberg bound states (denoted by horizontal solid lines $-$) for the ion ground state $an\ell$ and the ion excited state $bn'\ell'$, and respective continua $a\epsilon\ell'$ and $b\epsilon'\ell'$ (denoted by the slashed lines $///$). For dynamic polarization of the core to be negligible, and hence an adiabatic approximation to be sufficient, energy spacing over the Rydberg bound states and continuum must be very small compared to the ionic core energy levels, $\Delta \ll (W_b - W_a)$.

the continua. In the adiabatic limit, it is assumed that the Bohr frequencies of the ionic core are very large compared to the Bohr frequencies associated with transitions of the Rydberg atom [8].

Non-adiabatic effects must therefore be taken into account if the energy spacing between the ionic energy level separation ($W_b - W_a$) is not much larger than the Rydberg state energies Δ . Figure 4.3 shows an energy level diagram with two ionic core states labeled as a and b . The Rydberg atom states with a ground-state core are labeled $an\ell$, while Rydberg states with an excited core are $bn'\ell'$. The respective continua states corresponding to each of the core states are labeled as $a\epsilon\ell$ and $b\epsilon'\ell'$. The atom is prepared in a particular $an\ell$ state, but the Coulomb interaction with the core electrons can virtually drive a transition to a $bn'\ell'$ or $b\epsilon'\ell'$ state. The range of valence electron energies that can be accessed via this transition is labeled Δ . In the adiabatic approximation, Δ is supposed to be negligible compared to $(W_b - W_a)$. This is reasonable since the spacing between nearby Rydberg levels is often many orders of magnitude smaller than the core excitation energy. However, it is found in this work that the energy range Δ is not limited to nearby Rydberg states, but in fact extends over an energy range that is only somewhat smaller than $(W_b - W_a)$. We deal with this by including the effect of a non-zero Δ to first order in the perturbation theory expansion.

The details of this calculation are presented below, following Refs. [8, 12]. The final result is that the polarization energy of Equation (4.2) becomes

$$W_{pol,n\ell} = -\frac{1}{2}k_{d,n\ell}\alpha_d\langle r^{-4} \rangle_{n\ell} - \frac{1}{2}k_{q,n\ell}\alpha_q\langle r^{-6} \rangle_{n\ell} \quad (4.15)$$

where non-adiabatic correction factors to the core polarizability $k_{d,n\ell}$ and $k_{q,n\ell}$ for the dipole and quadrupole polarizability terms are introduced. In the adiabatic approximation, $k_{d,n\ell} = 1$ and $k_{q,n\ell} = 1$. The dipole and quadrupole polarization energy contributions, $W_{d,n\ell}$ and

$W_{q,n\ell}$, are separately considered

$$W_{pol,n\ell} = W_{d,n\ell} + W_{q,n\ell}. \quad (4.16)$$

First the dipole polarization energy term is considered. The non-adiabatic correction to the dipole term arises from the polarization shift of the rubidium $n\ell$ state due to the dipole polarization energy contribution $W_{d,n\ell}$ [8, 13]. To develop this model, the Rb^+ core is treated as if it has one electron. This consideration is reasonable since the distribution of the oscillator strengths from the ground state is of primary interest. The Hamiltonian for the ionic core electron and the Rydberg electron is given by

$$H = - \left[\frac{\nabla_1^2}{2} + \frac{\nabla_2^2}{2} + f(r_1) + f(r_2) - \frac{1}{r_{12}} \right] \quad (4.17)$$

where $-f(r)$ is the Coulombic potential of an electron at a distance of r from the remaining Rb^{++} ionic core and r_{12} is the distance between the core electron (denoted as electron 1) and Rydberg valence electron (denoted as electron 2). This Hamiltonian can be separated into two parts

$$H = H_0 + H_1 \quad (4.18)$$

where

$$H_0 = - \left[\frac{\nabla_1^2}{2} + \frac{\nabla_2^2}{2} + f(r_1) + \frac{1}{r_2} \right] \quad (4.19)$$

and

$$H_1 = -f(r_2) + \frac{1}{r_2} + \frac{1}{r_{12}}. \quad (4.20)$$

Conceptually, H_0 is the time-independent unperturbed Hamiltonian and the Hamiltonian H_1 is a perturbation on H_0 due to the Rydberg electron's interaction with the core electron. The electron interaction term $1/r_{12}$ is then expanded in terms of r_1 and r_2 and *Legendre polynomials*. For high- ℓ , $r_2 \gg r_1$ so the potential $f(r_2) \rightarrow 2/r_2$. The Hamiltonian H_1 is then

rewritten as

$$H_1 = -\frac{2}{r_2} + \frac{1}{r_2} + \left[\frac{1}{r_2} + \frac{r_1}{r_2^2} P_1(\cos \theta_{12}) + \frac{r_1^2}{r_2^3} P_2(\cos \theta_{12}) + \dots \right] \quad (4.21)$$

with the $1/r_{12}$ expansion in the brackets. Simplifying this expression,

$$H_1 = \frac{r_1}{r_2^2} P_1(\cos \theta_{12}) + \frac{r_1^2}{r_2^3} P_2(\cos \theta_{12}) + \dots \quad (4.22)$$

where θ_{12} is the angle between \mathbf{r}_1 and \mathbf{r}_2 , the two electrons to the core. The Legendre polynomials in terms of spherical harmonics are

$$P_\ell(\cos \theta_{12}) = \frac{4\pi}{2\ell + 1} \sum_m Y_{\ell m}^*(\theta_1, \phi_1) Y_{\ell m}(\theta_2, \phi_2) \quad (4.23)$$

where θ_i and ϕ_i are the angular coordinates of electron 1 to electron 2 relative to the Rb^+ core.

Applying the time-independent Schrödinger equation to Hamiltonian H_0 yields

$$-\left[\frac{\nabla_1^2}{2} + f(r_1) + \frac{\nabla_2^2}{2} + \frac{1}{r_2} \right] \Psi(\mathbf{r}_1, \mathbf{r}_2) = W\Psi(\mathbf{r}_1, \mathbf{r}_2) \quad (4.24)$$

where \mathbf{r}_1 is the vector of the core electron in relation to the core center of mass and \mathbf{r}_2 is the vector of the valence electron to the Rb^+ core center of mass. Equation (4.24) can be separated into two independent equations, one for the core electron wavefunction

$$-\left[\frac{\nabla_1^2}{2} + f(r_1) \right] \psi_1(\mathbf{r}_1) = W_1 \psi_1(\mathbf{r}_1) \quad (4.25)$$

and one for the Rydberg electron wavefunction

$$-\left[\frac{\nabla_2^2}{2} + \frac{1}{r_2} \right] \psi_2(\mathbf{r}_2) = W_2 \psi_2(\mathbf{r}_2). \quad (4.26)$$

It follows that the atom wavefunction is a direct product between the ion wavefunction $\psi_1(\mathbf{r})$ and the hydrogenic wavefunction $\psi_2(\mathbf{r})$ for the Rydberg electron.

$$\Psi(\mathbf{r}_2, \mathbf{r}_1) = \psi_1(\mathbf{r}_1)\psi_2(\mathbf{r}_2) \quad (4.27)$$

The total energy is therefore the sum of these energies

$$W = W_1 + W_2, \quad (4.28)$$

where W_1 is the ionic core energy and W_2 is the Rydberg electron energy.

The solution to the core electron wavefunction from equation (4.25) is $\phi_{n'\ell'm'}(\mathbf{r}_1)$, which is difficult to calculate since $f(r)$ is unknown. The solution to the hydrogenic wavefunction for the Rydberg electron from equation (4.26) is $u_{n\ell m}(\mathbf{r}_2)$, which is able to be analytically calculated. Equation (4.27) becomes

$$\Psi(\mathbf{r}_1, \mathbf{r}_2) = \phi_{n'\ell'm'}(\mathbf{r}_1)u_{n\ell m}(\mathbf{r}_2) \quad (4.29)$$

and equation (4.28) is then expressed as

$$W = W_{n'\ell'} - \frac{1}{2n^2} \quad (4.30)$$

where $W_{n'\ell'}$ is the energy of the $\text{Rb}^+ n'\ell'$ state with respect to the Rb^+ ionization limit.

For the actual Rb atom, the Rydberg electron interacts with all 36 electrons in the core. To account for this, the single electron core state ψ_1 is replaced by a multielectron state. The ground state of the core has the $4p^6$ configuration and is labeled as state a . In this calculation, an arbitrary excited state of the core is considered and labeled as b . The corresponding Rydberg states are therefore labeled as $an\ell$ and $bn'\ell'$, according to the state of the Rydberg electron.

The second-order energy correction to the Rb $an\ell$ state is evaluated first. The generic formula for a second-order energy shift in perturbation theory is given by

$$W_i^{(2)} = \sum_{i' \neq i} \frac{|\langle \Psi_{i'}^0 | H_1 | \Psi_i^0 \rangle|^2}{E_i^0 - E_{i'}^0} \quad (4.31)$$

with a sum over all linear combinations of orthonormal states i and i' . The superscript 0 denotes the unperturbed values. Dipole and quadrupole second-order corrected energy terms can also be separated

$$W_{n\ell}^{(2)} = W_{d,n\ell} + W_{q,n\ell} \quad (4.32)$$

along with the dipole (r_2^{-2}) and quadrupole (r_2^{-3}) components of H_1 in Eqn. (4.22). Eigenfunctions of the wavefunction in Eqn. (4.29) are spherical harmonics. Therefore, diagonal matrix elements of H_1 vanish for the Rb⁺ $4p^6$ states with no first order correction. The dipole second-order energy correction is thus

$$W_{d,n\ell} = \sum_{b,n'\ell'} \frac{\langle a | r_1 | b \rangle^2 \langle n\ell | r_2^{-2} P_1(\cos \theta_{12}) | n'\ell' \rangle^2}{(W_{an\ell} - W_{bn'\ell'})} \quad (4.33)$$

The matrix elements with the Legendre polynomials are found by evaluating the spherical harmonic scalar products of the tensor operators using the methods in Ref. [14] and applying the selection rule $\ell' = \ell \pm 1$. Upon this evaluation, the second-order dipole energy correction expression becomes

$$W_{d,n\ell} = \frac{1}{3} \sum_{b,n'} \langle a | r_1 | b \rangle^2 \left[\frac{\ell \langle n\ell | r_2^{-2} | n'(\ell-1) \rangle^2}{(2\ell+1)(W_{an\ell} - W_{bn'(\ell-1)})} + \frac{(\ell+1) \langle n\ell | r_2^{-2} | n'(\ell+1) \rangle^2}{(2\ell+1)(W_{an\ell} - W_{bn'(\ell+1)})} \right] \quad (4.34)$$

where the matrix elements $\langle n\ell | r_2^{-2} | n'(\ell-1) \rangle$ and $\langle n\ell | r_2^{-2} | n'(\ell+1) \rangle$ matrix elements are hydrogen radial dipole matrix elements.

Excited states of the ion that are dipole coupled to the ground state are first considered with the $an\ell$ state coupled to the $bn'\ell'$ state as well as the non-negligible continua states

$b\ell'$. The dipole energy term $W_{d,n\ell}$ correcting for the energies of the $\text{Rb}^+ 4p^6$ state (denoted as $an\ell$) expressed in Eqn. (4.34) contains the summation over n' which includes the continua above the Rydberg and ionization limits. Although the r^{-2} matrix elements are over hydrogenic states, they are not analytically known, and therefore computed numerically using Numerov's method. Accuracy of the obtained values are verified using the sum rule [8].

$$\sum_{n'} \langle n\ell | r^s | n'\ell' \rangle^2 = \langle n\ell | r^{2s} | n\ell \rangle \quad (4.35)$$

To evaluate Eqn. (4.34), all of the core energies W_b and matrix elements $\langle a|r|b \rangle$ need to be known. Unfortunately, these are not available, so an approximation is used to simplify the sum over b with a single effective excited state. This approximation is supported given that the non-adiabatic correction is small and Rydberg energies are small compared to the ion energies. To achieve this simplified expression, the denominator of Equation (4.34) is expressed as

$$W_{an\ell} - W_{bn'\ell'} = W_a - W_b + W_{n\ell} - W_{n'\ell'} \quad (4.36)$$

In further accordance with finding a simplified expression for Eqn. (4.34) by finding an effective excited ion state, a *Taylor expansion* is performed by treating $(W_{n\ell} - W_{n'\ell'}) / (W_a - W_b)$ as a small parameter. The Taylor expansion of Eqn. (4.34) is explicitly carried out as

$$W_{d,n\ell} = \sum_b \frac{\langle a|r_1|b \rangle^2}{3(W_a - W_b)} \sum_{n'} \left[\frac{\ell \langle n\ell | r_2^{-2} | n'(\ell-1) \rangle^2}{(2\ell+1)} \left(1 - \frac{W_{n\ell} - W_{n'(\ell-1)}}{W_a - W_b} \right) + \frac{(\ell+1) \langle n\ell | r_2^{-2} | n'(\ell+1) \rangle^2}{(2\ell+1)} \left(1 - \frac{W_{n\ell} - W_{n'(\ell+1)}}{W_a - W_b} \right) \right]. \quad (4.37)$$

Combining this with the sum rule in Eqn. (4.35), Eqn. (4.37) is rewritten as

$$W_{d,n\ell} = \sum_b \frac{\langle a|r_1|b\rangle^2}{3(W_a - W_b)} \left[\langle n\ell|r_2^{-4}|n\ell\rangle - \sum_{n'} \left(\frac{\ell(W_{n\ell} - W_{n'(\ell-1)})\langle n\ell|r_2^{-2}|n'(\ell-1)\rangle^2}{(2\ell+1)(W_a - W_b)} + \frac{(\ell+1)(W_{n\ell} - W_{n'(\ell+1)})\langle n\ell|r_2^{-2}|n'(\ell+1)\rangle^2}{(2\ell+1)(W_a - W_b)} \right) \right]. \quad (4.38)$$

The common denominator $(W_a - W_b)$ can be treated as a weighting factor in the n' sum.

This yields a center of mass of the Rydberg matrix elements

$$W_{cg,n\ell} = \frac{1}{\langle n\ell|r_2^{-4}|n\ell\rangle} \sum_{n'} \left[\frac{\ell(W_{n\ell} - W_{n'(\ell-1)})\langle n\ell|r_2^{-2}|n'(\ell-1)\rangle^2}{(2\ell+1)} + \frac{(\ell+1)(W_{n\ell} - W_{n'(\ell+1)})\langle n\ell|r_2^{-2}|n'(\ell+1)\rangle^2}{(2\ell+1)} \right] \quad (4.39)$$

which has no excited ion state b dependence. Rewriting Eqn. (4.38) in terms of Eqn. (4.39) yields the simplified expression

$$W_{d,n\ell} = \sum_b \frac{\langle a|r_1|b\rangle^2 \langle n\ell|r_2^{-4}|n\ell\rangle}{3(W_a - W_b)} \left[1 - \frac{W_{cg,n\ell}}{W_a - W_b} \right]. \quad (4.40)$$

The polarizability α_d in terms of dipole matrix elements is known to be

$$\alpha_d = - \sum_b \frac{\langle a|r_1|b\rangle^2}{6(W_a - W_b)}. \quad (4.41)$$

Using this definition of α_d , allows Eqn. (4.40) to be expressed as

$$W_{d,n\ell} = - \frac{\alpha_d}{2} \langle n\ell|r_2^{-4}|n\ell\rangle (1 - \chi_{n\ell}) \quad (4.42)$$

where $\chi_{n\ell}$ is introduced as

$$\chi_{n\ell} = \frac{\sum_b \frac{\langle a|r_1|b\rangle^2}{(W_a - W_b)^2} W_{cg,n\ell}}{\sum_b \frac{\langle a|r_1|b\rangle^2}{W_a - W_b}}. \quad (4.43)$$

In the adiabatic limit, $W_{n\ell} - W_{n'\ell'} \rightarrow 0$ and is negligible compared to $W_a - W_b$. For $W_{n\ell} - W_{n'\ell'} \rightarrow 0$, $W_{cg,n\ell} \rightarrow 0$ and $\chi_{n\ell} \rightarrow 0$. For this case, the energy shift from the core electron is regarded as negligible and with the energy expression above, core polarizability reduces to the adiabatic expression shown in Equation (4.2).

To determine whether the second-order, non-adiabatic effects need to be considered, the energy distribution of the Rydberg atom is calculated. This calculated energy distribution is plotted versus the $\langle 18g|r_2^{-2}|n'\ell\rangle$ Rydberg squared matrix elements and shown in Figure 4.4. These axes are chosen to better correspond with the traditional convention of an energy level diagram and Fig. 4.3. The Rydberg bound states $bn\ell'$ and continuum $be\ell'$ span a range of energies Δ that are not very small compared to the energy difference between the ground state and excited state of the ion ($W_b - W_a$). The energy spacing between the ground state and first-excited $4p^55s$ state of the Rb^+ ion is $(W_b - W_a) = 16.5$ eV, compared to $\Delta = 2.5$ eV calculated for $n = 18$. For the energies calculated for $n = 18$, Δ spans an energy range approximately 15% that of $(W_b - W_a)$. Given the fact that Δ is not negligible compared to $(W_b - W_a)$, non-adiabatic effects are non-negligible and must be accounted for to derive accurate core polarizability results.

The expressions for dipole polarizability energy in Eqns. (4.15), (4.16), and (4.42) are set equal to each other giving

$$W_{d,n\ell} = -\frac{1}{2}k_{d,n\ell}\alpha_d\langle r^{-4}\rangle_{n\ell} = -\frac{1}{2}\alpha_d\langle r^{-4}\rangle_{n\ell}(1 - \chi_{n\ell}); \quad (4.44)$$

and therefore,

$$k_{d,n\ell} = 1 - \chi_{n\ell}. \quad (4.45)$$

In an effort to simplify the sum over all of the ion states b , a single effective ion state energy W_{Id} is introduced. The single effective ion state energy W_{Id} is defined as the energy above

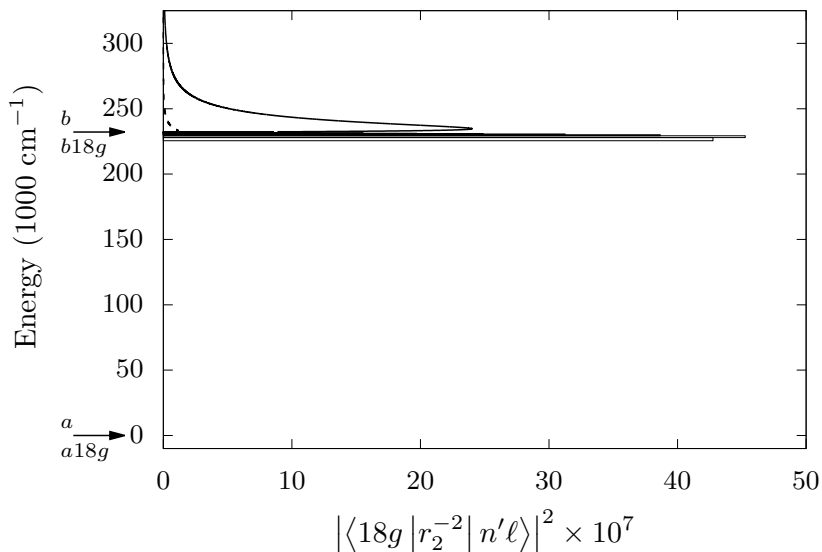


FIGURE 4.4: Energy distribution of the $\langle 18g|r_2^{-2}|n'\ell\rangle^2$ Rydberg matrix elements calculated for the non-adiabatic corrections factors. The vertical axis is the energy of the Rydberg atom, with the core ion ground state a and excited state b indicated by arrows. The energies for matrix elements $\langle 18g|r_2^{-2}|n'(\ell-1)\rangle^2$ and $\langle 18g|r_2^{-2}|n'(\ell+1)\rangle^2$ bound states are plotted as boxes. A dashed line is used to show the normalized energies for the matrix elements for the continuum state $b\epsilon(\ell-1)$ and a solid line for the normalized energies for the matrix elements for the continuum state $b\epsilon(\ell+1)$. The continuum states are normalized per unit energy. Ultimately, the energy range over which the matrix elements remains appreciable Δ is approximately 15% of the energy difference between $(W_b - W_a)$. Although small, dynamic core polarizability is not negligible. For clarity, the difference between the a and $a18g$ coupled state is omitted on this plot. The energies are too close to distinguish on the plot.

the ground state and subject to a weighted average of $1/(W_a - W_b)$.

$$\frac{1}{W_{Id}} = \frac{\sum_b \frac{\langle a|r_1|b\rangle^2}{(W_a - W_b)^2}}{\sum_b \frac{\langle a|r_1|b\rangle^2}{W_a - W_b}}, \quad (4.46)$$

The sum over all ion states b is replaced with this single excited state ion energy W_{Id} and it follows from Eqn. (4.40) that the non-adiabatic energy shift is

$$\Delta W_{d,n\ell} = \frac{1}{3} \langle a|r_1|I\rangle^2 \sum_{n'} \left[\frac{\ell \langle n\ell|r_2^{-2}|n'(\ell-1)\rangle^2}{(2\ell+1)(W_{an\ell} - W_{In'(\ell-1)})} + \frac{(\ell+1) \langle n\ell|r_2^{-2}|n'(\ell+1)\rangle^2}{(2\ell+1)(W_{an\ell} - W_{In'(\ell+1)})} \right] \quad (4.47)$$

where I is the single ion state and $\langle a|r_1|I\rangle$ is the matrix element corresponding to the single effective ion state, replacing the sum over all b excited states. The expression relating dipole polarizability to dipole matrix elements is given by

$$\langle a|r_1|I\rangle^2/3 = 2\alpha_d W_{Id}. \quad (4.48)$$

Because of the relationship in Eqn. (4.48), the direct evaluation of $\langle a|r_1|I\rangle$ is not necessary for determining the non-adiabatic energy shift. Instead, the value for the effective ion excitation energy W_{Id} needs to be determined. This is done by an empirical estimate, as opposed to a theory calculation. Empirical values for low-lying W_b states are available from ion spectroscopy. In this empirical estimate, the method prescribed here introduces *oscillator strengths* which describes the total oscillating potential of an atomic transition [15], defined as

$$f_{a \rightarrow b} = \frac{2}{3} (W_b - W_a) |\langle a|r_1|b\rangle|^2. \quad (4.49)$$

It follows from Eqn. (4.46) with W_{Id} in terms of oscillator strength $f_{a \rightarrow b}$ between ion states a and b that

$$\frac{1}{W_{Id}} = \frac{\sum_b \frac{f_{a \rightarrow b}}{(W_a - W_b)^3}}{\sum_b \frac{f_{a \rightarrow b}}{(W_a - W_b)^2}}. \quad (4.50)$$

If the oscillator strength distribution for Rb^+ is known, $k_{d,n\ell}$ is solved for by using Eqn. (4.44) and Eqn. (4.48).

$$k_{d,n\ell} = \frac{W_{Id}}{\langle n\ell | r_2^{-4} | n\ell \rangle} \sum_{n'} \left[\frac{\ell \langle n\ell | r_2^{-2} | n'(\ell-1) \rangle^2}{(2\ell+1)(W_{an\ell} - W_{In'(\ell-1)})} + \frac{(\ell+1) \langle n\ell | r_2^{-2} | n'(\ell+1) \rangle^2}{(2\ell+1)(W_{an\ell} - W_{In'(\ell+1)})} \right] \quad (4.51)$$

Experimental data for the oscillator strength distribution of Rb^+ is not well known. Therefore, to determine oscillator strengths, comparing *photoionization cross-section* which is well known for rubidium to another atom where both oscillator strengths and photoionization cross-section are well known can be used to extrapolate Rb^+ oscillator strengths. Photoionization cross-section is introduced as σ_{PI} where the cross-section for exciting to above the ionizing limit is

$$\sigma_{PI} = \frac{2\pi^2}{c^2} \frac{df_{a \rightarrow b}}{dW} \quad (4.52)$$

Consequently, photoionization cross-section is proportional to $df_{a \rightarrow b}/dW$, following Eqn. (4.49).

An atom identified to have well known photoionization cross-sections and oscillator strengths with a closed $4p^6$ atomic orbital shell, like the Rb^+ ionic core, is isoelectronic neutral krypton. Photoionization cross-sections for isoelectronic neutral Kr are determined and compared to the Rb^+ ion and found to be similar per References [16, 17]. Oscillator strengths for Kr are known for both the bound states and the continuum, found in Ref. [18]. To make a comparison between Kr and the ionic core of Rb, known energies between each must be considered. One of these quantities is the first ionization limit, or the amount of energy required to remove the most loosely bound electron from the atom. The first

Species	Ionization Limit (cm ⁻¹)	First Excited State Energy (cm ⁻¹)	Ref.
H	109 700	82 260	
Kr	112 900	80 500	[19, 21]
Rb ⁺	220 100	134 000	[20]

TABLE 4.2: Ionization limits and first excited state energies for H, Kr, and Rb⁺.

ionization limit of Kr is approximately 112 900 cm⁻¹ [19]. Using the oscillator strengths of Kr from these references and using Eqn. (4.50), W_{Id} for Kr is found to be 119 700 cm⁻¹, approximately 6% larger than the first ionization limit. This result is applied to Rb⁺ to estimate the value of W_{Id} . It is estimated to be 6% larger than the first ionization limit at $W_{Id} = 232\,300$ cm⁻¹ where the first ionization limit of Rb⁺ is 220 100 cm⁻¹ [20].

This calculation of the Rb⁺ oscillator strengths serves as an estimate, and is thus uncertain. To estimate the uncertainty, comparisons between oscillator strength distributions and ionization limits between H, Rb⁺, and Kr are performed. Oscillator strengths for hydrogen can be calculated, and W_{Id} can be determined directly. Calculating W_{Id} in atomic hydrogen yields a value just above the lowest $1s \rightarrow 2p$ transition energy, indicating that the lower-lying transitions contribute greatly to the total oscillator strength distribution. Unlike H, the isoelectronic neutral Kr oscillator strength distribution is disproportionately biased above the ionization limit. Oscillator strengths for the bound states are approximately 6 times less when compared to the continua for the first 160 000 cm⁻¹ above the ionization limit [18]. This provides a rationale for why W_{Id} for Rb may be more comparable to the ionization limit for Kr, when compared to H.

The single effective ion state energy W_{Id} for Kr is 6% above the ionization limit, while W_{Id} for H is 25% below. The reasonable energy scale of variation for W_{Id} is therefore approximately 50% of the ionization energy. Since it is reasonable to assume that Kr is a more accurate analog for Rb than H, the scale factor is reduced by a factor of approximately 2.5, and an estimate for the uncertainty is $\pm 10\%$. This scale is determined by comparing the first excited state transition energy to W_{Id} , with the first excited state energy of Rb⁺ at

134 000 cm⁻¹ [20]. This $\pm 10\%$ uncertainty applied to W_{Id} correlates to a $\pm 10\%$ uncertainty in $(1 - k_{d,n\ell})$, per Eqns. (4.44) and (4.45). It is understood that this is an *ad hoc* approach and there is a need for a more justified calculation of W_{Id} and related uncertainties. This will hopefully provide motivation for future work.

Attention is now turned to the quadrupole term, following the dipole polarizability non-adiabatic correction considered earlier. The treatment for the quadrupole non-adiabatic correction factor $k_{q,n\ell}$ is very similar to the approach for $k_{d,n\ell}$, however the $\langle n\ell|r_2^{-3}|n'\ell'\rangle$ matrix elements are required for quadrupole correction calculation, as opposed to the $\langle n\ell|r_2^{-2}|n'\ell'\rangle$ matrix elements for the dipole correction. These quadrupole matrix elements are calculated numerically in a similar way to the dipole matrix elements using hydrogen wavefunctions. Applying the same treatment as above, an equivalent expression to Eqn. (4.51) for $k_{q,n\ell}$ is [13].

$$k_{q,n\ell} = \frac{W_{Iq}}{\langle n\ell|r_2^{-6}|n\ell\rangle} \frac{3(2\ell+1)(\ell+1)(\ell+2)}{10(4\ell^2-1)(2\ell+3)} \left[\sum_{n'} \frac{\langle n\ell-2|r_2^{-3}|n\ell\rangle^2}{W_{a,n\ell} - W_{Iq,n'(\ell-2)}} \right. \\ \left. + \frac{2(\ell^2+\ell)(2\ell+1)}{3} \sum_{n'} \frac{\langle n\ell|r_2^{-3}|n\ell\rangle^2}{W_{a,n\ell} - W_{Iq,n'\ell}} (2\ell+3)(\ell^2-\ell) \sum_{n'} \frac{\langle n\ell+2|r_2^{-3}|n\ell\rangle^2}{W_{a,n\ell} - W_{Iq,(n'\ell+2)}} \right] \quad (4.53)$$

where the effective quadrupole excited state ion energy is

$$\frac{1}{W_{Iq}} = \frac{\sum_b \frac{\langle a|r_1^2|b\rangle^2}{(W_a - W_b)^2}}{\sum_b \frac{\langle a|r_1^2|b\rangle^2}{W_a - W_b}}. \quad (4.54)$$

Unfortunately for the quadrupole non-adiabatic correction, knowledge of the Rb⁺ ion state quadrupole energy W_{Iq} is less straight-forward. This is because an analogy cannot be made using oscillator strengths and photoionization cross-section, given the $\langle a|r_1^2|b\rangle$ matrix elements in Eqn (4.54). Therefore, an estimation is performed based on a comparison

n	k_d			k_q		
	$\ell = 4$	5	6	4	5	6
17-19	0.978(2)	0.990(1)	0.994(1)	0.919(15)	0.966(7)	0.984(3)
27-30	0.977(2)	0.990(1)		0.919(15)	0.966(7)	

TABLE 4.3: Non-adiabatic correction factors, calculated as in Eqn. (4.51). The lower- n values are relevant to the data taken here, and the higher- n values are for the data of Ref. [1].

to hydrogen. Since the quadrupole oscillator strength distribution for H is not as heavily concentrated to a single state transition, this treatment is suitable. For hydrogen, W_{Iq} is calculated to be $112\,465\text{ cm}^{-1}$, approximately 12% above the ionization limit. Applying the same ratio to the Rb^+ ion, W_{Iq} is evaluated to be $248\,000\text{ cm}^{-1}$. No comparison to the Kr oscillator strengths can be made in this case, so a $\pm 20\%$ uncertainty is applied to W_{Iq} according to the 50% energy range discussed previously. This $\pm 20\%$ uncertainty directly corresponds to a $\pm 20\%$ uncertainty in $(1 - k_{q,n\ell})$.

4.2.2 Non-adiabatic corrected results

Upon calculating dipole and quadrupole matrix elements, the dipole and quadrupole non-adiabatic correction factors $k_{d,n\ell}$ and $k_{q,n\ell}$ are calculated, respectively. These correction factors are calculated for $n = 17 - 19$, $\ell = 4 - 6$, commensurate with this experiment. Additionally, k_d and k_q are calculated for $n = 27 - 30$ to use in conjunction with previous work by Lee, *et al.* [1]. The calculated k_d and k_q correction factors corresponding to these $n\ell$ states are shown in Table 4.3.

The measured energy differences between the $n\ell$ states remains ΔW , and Eqn. (4.11) remains true, now with $k_{d,n\ell}$ and $k_{q,n\ell}$ correction factors applied to Δ_d and Δ_q , respectively. Redefining Δ_d and Δ_q with these correction factors yield

$$\Delta_d = \frac{1}{2}k_{d,n\ell}\langle r^{-4} \rangle_{n\ell} - \frac{1}{2}k_{d,n\ell'}\langle r^{-4} \rangle_{n\ell'} \quad (4.55)$$

and

$$\Delta_q = \frac{1}{2}k_{q,n\ell}\langle r^{-6}\rangle_{n\ell} - \frac{1}{2}k_{q,n\ell'}\langle r^{-6}\rangle_{n\ell'} \quad (4.56)$$

between $n\ell$ and $n\ell'$ states. Just as applied before the non-adiabatic correction, ΔW is the fine structure corrected transition frequencies shown in Table 3.14. Plotted in Figure 4.5 is $2\Delta W/\Delta_d$ vs. Δ_q/Δ_d with the $n = 17 - 19 g \rightarrow h$ and $h \rightarrow i$ measured transitions from this work along with the results of Lee, *et al.* with $n = 27 - 30 d \rightarrow g$ and $d \rightarrow h$ [1]. The data collected in this experiment are plotted as dots and data collected in the previous experiment are plotted as circles. Upon fitting the data points, which do not take into account uncertainty in $k_{d,n\ell}$ and $k_{q,n\ell}$, the linear least squares fit y-intercept is found to be $\alpha_d = 9.068(6) a_0^3$ and the slope to be $\alpha_q = 42.2(5) a_0^5$.

Uncertainties for the non-adiabatic correction factors $k_{d,n\ell}$ and $k_{q,n\ell}$ must be incorporated. The usual approach of adding a horizontal error bar to the data points, then reanalyzing does not work here since the y-intercept and slope of the least squares linear fit are not mutually exclusive of a change in the non-adiabatic correction factors. Instead, to take these into account, W_{Id} and W_{Iq} are varied by their respective uncertainties of $\pm 10\%$ and $\pm 20\%$. A $\pm 10\%$ change in W_{Id} leads to a $\pm 0.004 a_0^3$ change in α_d and a $\pm 1.7 a_0^5$ change in α_q . A $\pm 20\%$ change in W_{Iq} leads to a $\mp 0.003 a_0^3$ change in α_d and a $\pm 1.0 a_0^5$ change in α_q . Adding the changes in α_d and α_q in quadrature with the statistical fit uncertainties yields the following dipole and quadrupole core polarizability values: $\alpha_d = 9.068(8) a_0^3$ and $\alpha_q = 42(2) a_0^5$. The gray band in the plot of Figure 4.5 graphically shows how the intercept α_d and slope α_q change as W_{Id} and W_{Iq} are varied by their uncertainties.

The adiabatic approximation core polarizability results are compared to the non-adiabatic corrected values. The dipole polarizability α_d is increased by $0.004 a_0^3$ and the uncertainty is more than doubled, remaining in agreement with α_d found in the adiabatic approximation. A significant change is seen in the quadrupole polarizability α_q , which is more than double when factoring in the non-adiabatic correction. Uncertainty for the quadrupole

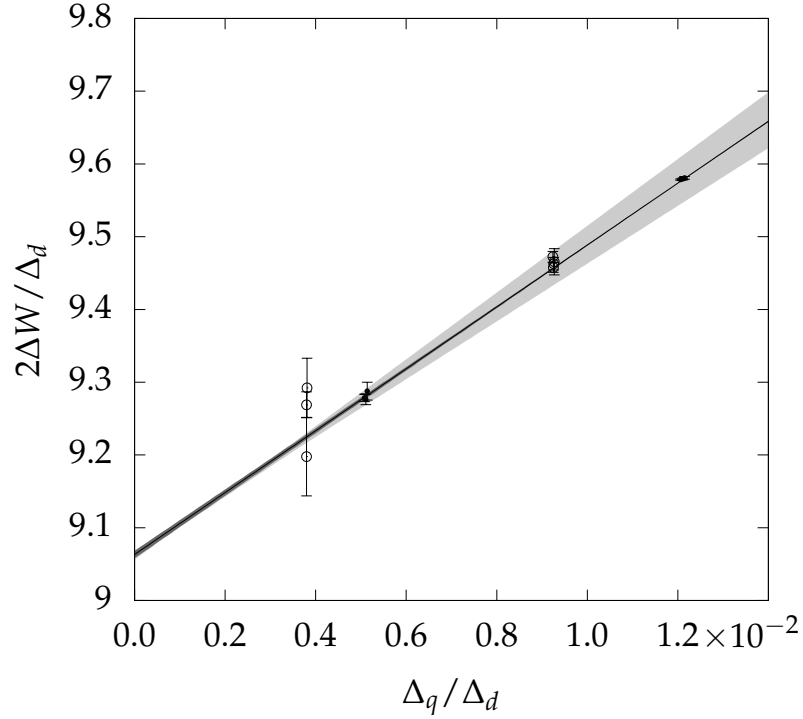


FIGURE 4.5: Core polarizability with non-adiabatic correction factors k_d and k_q . Both data acquired in this experiment are plotted and fit along with the data of the previous experiment in Ref. [1]. The data in this experiment are plotted as dots and previous experiment plotted as circles. Note that the previous work reports quantum defects from which core polarization energies are determined. Therefore, polarization energies are plotted for each state, not the difference between states as is done here. This is seen in Figure 4.2. Upon accounting for the non-adiabatic correction factors, the intercept and slope of the statistical fit of the line are $\alpha_d = 9.068(6) a_0^3$ and $\alpha_q = 42.2(5) a_0^5$, respectively. These statistical uncertainties do not take into account the uncertainties of W_{Id} and W_{Iq} , $\pm 10\%$ and $\pm 20\%$, respectively. The gray band on this plot shows the range of values that are encompassed by varying W_{Id} and W_{Iq} by their uncertainties. The intercept α_d is slightly affected, but the slope α_q is mostly effected. Upon updating the uncertainties by adding the change in α_d and α_q as a result of varying W_{Id} and W_{Iq} in quadrature, the core polarizability results are: $\alpha_d = 9.068(8) a_0^3$ and $\alpha_q = 42(2) a_0^5$.

term is also increased by a factor of 6. The large increase in uncertainties stem from the relatively high uncertainties for W_{Id} and W_{Iq} .

4.2.3 Comparison to theory

Comparisons between these experimental results and theoretically calculated dipole and quadrupole polarizabilities can be made. The dipole polarizability remains within reasonable agreement with theoretical calculations ($9.076 a_0^3 < \alpha_d < 9.11 a_0^3$) [7, 22, 23]. And, the inclusion of a non-adiabatic correction leads to a quadrupole polarizability result which are in reasonable agreement with theoretically calculated values ($35.41 a_0^5 < \alpha_q < 38.37 a_0^5$), to within approximately two standard deviations [7, 22, 24]. By including the non-adiabatic correction to the core polarization model for the measurements made in this experiment, the discrepancy with theoretical calculations have been resolved.

4.3 Quantum defects

As introduced earlier, the *quantum defect* is the bound state energy level difference between a hydrogen atom and the bound state energy level for a hydrogen-like Rydberg atom. Quantum defects are calculated with knowledge of the core polarization energies for alkali metals. This energy of a $n\ell$ state is given by the Rydberg formula

$$W_{n\ell} = -\frac{1}{2(n - \delta_\ell)^2} \quad (4.57)$$

where n is the principal quantum number and δ_ℓ is the quantum defect. The quantum defects reduces the energy levels of the hydrogen-like atom compared to hydrogen for a given angular momentum state, ℓ .

Using quantum defect theory, a direct comparison of the reduction in energy levels due to core polarization effects can be similarly expressed. The energy of an $n\ell$ state in the core

polarization model is given by

$$W_{n\ell} = -\frac{1}{2n^2} + W_{pol} \quad (4.58)$$

with W_{pol} being the polarization energy expressed in Eqn. (4.2). Calculating quantum defects is now simply a matter of setting Equations (4.57) and (4.58) equal to each other then solving for δ_ℓ . Sparing algebraic steps, the expression for quantum defect in terms of the polarizability energy is found to be

$$\delta_\ell = n - \sqrt{\frac{n^2}{1 - 2n^2W_{pol}}}. \quad (4.59)$$

The linear least squares fit parameters α_d and α_q from the adiabatic approximation are used to find the polarization energy using Eqn. (4.2) with hydrogenic expectation values for the $n = 17 - 19$ $g, h,$ and i states. Quantum defects are then calculated and tabulated in Table 4.4. Notably, the states presented in the table reflect the same states for which experimental measurements were performed. In theory, quantum defects for other hydrogenic $n\ell$ states can be calculated in this manner. Quantum defects for additional n and ℓ states are shown in Appendix D.

Furthermore, this method uses the core polarizability determined with the adiabatic approximation. The reason for this is that the spectroscopic measurements made in this experiment correspond to relative measurements of the polarization energy W_{pol} , defined in Eqns. (4.2) and (4.3). Since a measured quantity is used in this analysis, applying the non-adiabatic corrected polarizabilities would introduce an unnecessary uncertainty to quantum defect results.

The quantum defect has a n dependence that is introduced to account for the motion of the Rydberg electron. Solving for the eigenvalues of a Hamiltonian with a Coulombic

	$n\ell$	δ
$n = 17$	g	0.003908(2)
	h	0.0013697(5)
	i	0.0005762(2)
$n = 18$	g	0.003918(2)
	h	0.0013750(5)
	i	0.0005794(2)
$n = 19$	g	0.003927(2)
	h	0.0013794(5)
	i	0.0005821(2)

TABLE 4.4: Quantum defects for $n = 17$ to 19 g , h , and i states

potential and a short-range spherically symmetric correction, results in Equation (4.57) exactly with an introduction of even power harmonic terms of $1/(n - \delta)$. These energy terms were first described by Ritz [25], and it was later applied using older quantum theory by Sommerfeld [26], then Hartree [27] using wave mechanics [28]. This expansion is known as the Ritz expansion described by Equation (4.60) with Ritz coefficients $\delta_0, \delta_2, \delta_4, \delta_6$, etc.

$$\delta_{n\ell} = \delta_0 + \frac{\delta_2}{(n - \delta_0)^2} + \frac{\delta_4}{(n - \delta_0)^4} + \frac{\delta_6}{(n - \delta_0)^6} + \dots \quad (4.60)$$

The Ritz coefficients are determined by fitting the results in Table 4.4 using least squares to the Ritz formula in Eqn. (4.60). Ritz coefficients are reported for δ_0 and δ_2 since higher order terms in the Ritz expansion are negligible for higher ℓ states given the n and δ_0 dependence. The Ritz coefficients δ_0 and δ_2 are calculated by fitting the quantum defects for $n = 17 - 19$ reported in Table 4.4 and quantum defects for $n = 27 - 30$ reported in Ref. [1] to this form. Ritz coefficients per this least squares fit are reported in Table 4.5.

4.3.1 Comparison to previous work

Quantum defect Ritz expansion terms reported in the previous work for the Rb g state are in agreement with the calculated values here. Notably for the Rb g state, δ_0 reported in this work is approximately 20 times more precise and δ_2 reported in this work is approximately

Ritz Coefficient	ℓ	Value
δ_0	g	0.004011(1)
	h	0.001424(3)
	i	0.000606(1)
δ_2	g	-0.0299(6)
	h	-0.0156(8)
	i	-0.0086(4)

TABLE 4.5: Quantum defect Ritz expansion coefficients of Eqn. (4.60) per the polarization energies calculated, plotted, and fit using least squares to the Ritz formula.

25 times more precise. Quantum defect Ritz expansion parameters for the Rb h state are not reported in Ref. [1]; however, quantum defects for $n = 28 - 30$ nh states are provided. Upon fitting these to the Ritz expansion, Ritz expansion parameters for the Rb h state are found to be $\delta_0 = 0.00143(5)$ and $\delta_2 = 0.02(4)$ for the previous work. Ritz expansion terms calculated in this work for nh are consistent with the previous experimental values, but are approximately 17 times more precise for δ_0 and approximately 50 times more precise for δ_2 .

References

- [1] Jeonghun Lee, J. Nunakaew, and T. F. Gallagher. “Microwave spectroscopy of the cold rubidium ($n + 1$) $d_{5/2} \rightarrow n g$ and $n h$ transitions”. en. In: *Physical Review A* 94.2 (Aug. 2016), p. 022505. ISSN: 2469-9926, 2469-9934. DOI: [10.1103/PhysRevA.94.022505](https://doi.org/10.1103/PhysRevA.94.022505). URL: <https://link.aps.org/doi/10.1103/PhysRevA.94.022505> (visited on 05/25/2020).
- [2] M. Born and W. Heisenberg. “Über den Einfluss der Deformierbarkeit der Ionen auf optische und chemische Konstanten. I”. de. In: *Zeitschrift für Physik* 23.1 (Dec. 1924), pp. 388–410. ISSN: 1434-6001, 1434-601X. DOI: [10.1007/BF01327603](https://doi.org/10.1007/BF01327603). URL: <http://link.springer.com/10.1007/BF01327603> (visited on 07/16/2020).
- [3] Joseph E. Mayer and Maria Goeppert Mayer. “The Polarizabilities of Ions from Spectra”. en. In: *Physical Review* 43.8 (Apr. 1933), pp. 605–611. ISSN: 0031-899X. DOI: [10.1103/PhysRev.43.605](https://doi.org/10.1103/PhysRev.43.605). URL: <https://link.aps.org/doi/10.1103/PhysRev.43.605> (visited on 05/21/2020).
- [4] Bengt Edlen. “Atomic Spectra”. In: *Spectroscopy I / Spektroskopie I*. Ed. by S. Flugge. Vol. 5 / 27. Series Title: Encyclopedia of Physics / Handbuch der Physik. Berlin, Heidelberg: Springer Berlin Heidelberg, 1964, pp. 80–220. ISBN: 978-3-662-35392-9 978-3-662-35391-2. DOI: [10.1007/978-3-662-35391-2_2](https://doi.org/10.1007/978-3-662-35391-2_2). URL: http://link.springer.com/10.1007/978-3-662-35391-2_2 (visited on 06/24/2020).
- [5] G. W. F. Drake and R. A. Swainson. “Expectation values of r^p for arbitrary hydrogenic states”. en. In: *Physical Review A* 42.3 (Aug. 1990), pp. 1123–1126. ISSN: 1050-2947, 1094-1622. DOI: [10.1103/PhysRevA.42.1123](https://doi.org/10.1103/PhysRevA.42.1123). URL: <https://link.aps.org/doi/10.1103/PhysRevA.42.1123> (visited on 05/21/2020).
- [6] K. A. Safinya, T. F. Gallagher, and W. Sandner. “Resonance measurements of f - h and f - i intervals in cesium using selective and delayed field ionization”. en. In: *Physical*

- Review A* 22.6 (Dec. 1980), pp. 2672–2678. ISSN: 0556-2791. DOI: [10.1103/PhysRevA.22.2672](https://doi.org/10.1103/PhysRevA.22.2672). URL: <https://link.aps.org/doi/10.1103/PhysRevA.22.2672> (visited on 06/24/2020).
- [7] M. S. Safronova and U. I. Safronova. “Critically evaluated theoretical energies, lifetimes, hyperfine constants, and multipole polarizabilities in Rb 87”. en. In: *Physical Review A* 83.5 (May 2011), p. 052508. ISSN: 1050-2947, 1094-1622. DOI: [10.1103/PhysRevA.83.052508](https://doi.org/10.1103/PhysRevA.83.052508). URL: <https://link.aps.org/doi/10.1103/PhysRevA.83.052508> (visited on 06/06/2020).
- [8] J. H. Van Vleck and N. G. Whitelaw. “The Quantum Defect of Nonpenetrating Orbits, with Special Application to Al II”. en. In: *Physical Review* 44.7 (Oct. 1933), pp. 551–569. ISSN: 0031-899X. DOI: [10.1103/PhysRev.44.551](https://doi.org/10.1103/PhysRev.44.551). URL: <https://link.aps.org/doi/10.1103/PhysRev.44.551> (visited on 05/22/2020).
- [9] H Eissa and U Öpik. “The polarization of a closed-shell core of an atomic system by an outer electron I. A correction to the adiabatic approximation”. In: *Proceedings of the Physical Society* 92.3 (Nov. 1967), pp. 556–565. ISSN: 0370-1328. DOI: [10.1088/0370-1328/92/3/307](https://doi.org/10.1088/0370-1328/92/3/307). URL: <https://iopscience.iop.org/article/10.1088/0370-1328/92/3/307> (visited on 06/26/2020).
- [10] Richard J. Drachman. “Rydberg states of helium: An optical-potential analysis”. en. In: *Physical Review A* 26.3 (Sept. 1982), pp. 1228–1238. ISSN: 0556-2791. DOI: [10.1103/PhysRevA.26.1228](https://doi.org/10.1103/PhysRevA.26.1228). URL: <https://link.aps.org/doi/10.1103/PhysRevA.26.1228> (visited on 06/16/2020).
- [11] E. L. Snow et al. “Determination of dipole and quadrupole polarizabilities of Ba + by measurement of the fine structure of high- $L n = 9$ and 10 Rydberg states of barium”. en. In: *Physical Review A* 71.2 (Feb. 2005), p. 022510. ISSN: 1050-2947, 1094-1622. DOI: [10.1103/PhysRevA.71.022510](https://doi.org/10.1103/PhysRevA.71.022510). URL: <https://link.aps.org/doi/10.1103/PhysRevA.71.022510> (visited on 06/16/2020).

- [12] Thomas F. Gallagher. *Rydberg atoms*. Digitally printed 1st pbk. version. Cambridge monographs on atomic, molecular, and chemical physics 3. Cambridge ; New York: Cambridge University Press, 2005. ISBN: 978-0-521-02166-1.
- [13] T. F. Gallagher, R. Kachru, and N. H. Tran. "Radio frequency resonance measurements of the $Ba\ 6s\ n\ g - 6s\ n\ h - 6s\ n\ i - 6s\ n\ k$ intervals: An investigation of the nonadiabatic effects in core polarization". en. In: *Physical Review A* 26.5 (Nov. 1982), pp. 2611–2622. ISSN: 0556-2791. DOI: [10.1103/PhysRevA.26.2611](https://doi.org/10.1103/PhysRevA.26.2611). URL: <https://link.aps.org/doi/10.1103/PhysRevA.26.2611> (visited on 06/26/2020).
- [14] Alan R Edmonds. *Angular momentum in quantum mechanics*. Tech. rep. CERN, 1955.
- [15] Werner Kuhn. "Über das Absorptionsspektrum der Polyene". en. In: *Helvetica Chimica Acta* 31.6 (1948), pp. 1780–1799. ISSN: 0018019X. DOI: [10.1002/hlca.19480310644](https://doi.org/10.1002/hlca.19480310644). URL: <http://doi.wiley.com/10.1002/hlca.19480310644> (visited on 07/11/2020).
- [16] James A.R. Samson. "The Measurement of the Photoionization Cross Sections of the Atomic Gases". en. In: *Advances in Atomic and Molecular Physics*. Vol. 2. Elsevier, 1966, pp. 177–261. ISBN: 978-0-12-003802-2. DOI: [10.1016/S0065-2199\(08\)60219-5](https://doi.org/10.1016/S0065-2199(08)60219-5). URL: <https://linkinghub.elsevier.com/retrieve/pii/S0065219908602195> (visited on 06/27/2020).
- [17] Brendan M McLaughlin and James F Babb. "Single photoionization of the Kr-like Rb ii ion in the photon energy range 22–46.0 eV". en. In: *Monthly Notices of the Royal Astronomical Society* 486.1 (June 2019), pp. 245–250. ISSN: 0035-8711, 1365-2966. DOI: [10.1093/mnras/stz790](https://doi.org/10.1093/mnras/stz790). URL: <https://academic.oup.com/mnras/article/486/1/245/5382061> (visited on 06/27/2020).
- [18] Joseph Berkowitz. "TOTAL PHOTOABSORPTION AND PHOTOIONIZATION CROSS SECTIONS FOR SELECTED MOLECULES". en. In: *Photoabsorption, Photoionization, and Photoelectron Spectroscopy*. Elsevier, 1979, pp. 73–154. ISBN: 978-0-12-091650-4.

- DOI: [10.1016/B978-0-12-091650-4.50011-6](https://doi.org/10.1016/B978-0-12-091650-4.50011-6). URL: <https://linkinghub.elsevier.com/retrieve/pii/B9780120916504500116> (visited on 06/27/2020).
- [19] S Yoon and W L Glab. "Rydberg series of krypton excited from the $5p[3/2]_{1,2}$ states". In: *Journal of Physics B: Atomic, Molecular and Optical Physics* 27.18 (Sept. 1994), pp. 4133–4143. ISSN: 0953-4075, 1361-6455. DOI: [10.1088/0953-4075/27/18/013](https://doi.org/10.1088/0953-4075/27/18/013). URL: <https://iopscience.iop.org/article/10.1088/0953-4075/27/18/013> (visited on 06/27/2020).
- [20] Joseph Reader. "Spectrum and energy levels of singly ionized rubidium (Rb ii)". en. In: *Journal of the Optical Society of America* 65.3 (Mar. 1975), p. 286. ISSN: 0030-3941. DOI: [10.1364/JOSA.65.000286](https://doi.org/10.1364/JOSA.65.000286). URL: <https://www.osapublishing.org/abstract.cfm?URI=josa-65-3-286> (visited on 05/22/2020).
- [21] V. Kaufman. "Wavelengths and energy levels of neutral Kr-84 and level shifts in all Kr even isotopes". en. In: *Journal of Research of the National Institute of Standards and Technology* 98.6 (Nov. 1993), p. 717. ISSN: 1044-677X. DOI: [10.6028/jres.098.047](https://doi.org/10.6028/jres.098.047). URL: https://nvlpubs.nist.gov/nistpubs/jres/098/jresv98n6p717_A1b.pdf (visited on 07/25/2020).
- [22] W.R. Johnson, Dietmar Kolb, and K.-N. Huang. "Electric-dipole, quadrupole, and magnetic-dipole susceptibilities and shielding factors for closed-shell ions of the He, Ne, Ar, Ni (Cu+), Kr, Pb, and Xe isoelectronic sequences". en. In: *Atomic Data and Nuclear Data Tables* 28.2 (Mar. 1983), pp. 333–340. ISSN: 0092640X. DOI: [10.1016/0092-640X\(83\)90020-7](https://doi.org/10.1016/0092-640X(83)90020-7). URL: <https://linkinghub.elsevier.com/retrieve/pii/S0092640X83900207> (visited on 06/26/2020).
- [23] Jean Heinrichs. "Simple Calculation of Polarizabilities, Hyperpolarizabilities, and Magnetic Susceptibilities of Atoms and Ions". en. In: *The Journal of Chemical Physics* 52.12 (June 1970), pp. 6316–6319. ISSN: 0021-9606, 1089-7690. DOI: [10.1063/1.1672943](https://doi.org/10.1063/1.1672943). URL: <http://aip.scitation.org/doi/10.1063/1.1672943> (visited on 06/25/2020).

- [24] R. M. Sternheimer. “Quadrupole Polarizabilities of Various Ions and the Alkali Atoms”. en. In: *Physical Review A* 1.2 (Feb. 1970), pp. 321–327. ISSN: 0556-2791. DOI: [10.1103/PhysRevA.1.321](https://doi.org/10.1103/PhysRevA.1.321). URL: <https://link.aps.org/doi/10.1103/PhysRevA.1.321> (visited on 06/25/2020).
- [25] W Ritz. In: *Phys. Z.* 4 (1903), p. 406. ISSN: 0722-3277.
- [26] A. Sommerfeld. “Allgemeine spektroskopische Gesetze, insbesondere ein magnetooptischer Zerlegungssatz”. In: *Annalen der Physik (1900)* 368.19 (1920). Publisher: John Wiley & Sons Inc, pp. 221–263. ISSN: 0003-3804. DOI: [10.1002/andp.19203681903](https://doi.org/10.1002/andp.19203681903).
- [27] D. R. Hartree. “The Wave Mechanics of an Atom with a non-Coulomb Central Field. Part III. Term Values and Intensities in Series in Optical Spectra”. en. In: *Mathematical Proceedings of the Cambridge Philosophical Society* 24.3 (July 1928), pp. 426–437. ISSN: 0305-0041, 1469-8064. DOI: [10.1017/S0305004100015954](https://doi.org/10.1017/S0305004100015954). URL: https://www.cambridge.org/core/product/identifier/S0305004100015954/type/journal_article (visited on 06/24/2020).
- [28] G. W. F. Drake and R. A. Swainson. “Quantum defects and the $1/n$ dependence of Rydberg energies: Second-order polarization effects”. en. In: *Physical Review A* 44.9 (Nov. 1991), pp. 5448–5459. ISSN: 1050-2947, 1094-1622. DOI: [10.1103/PhysRevA.44.5448](https://doi.org/10.1103/PhysRevA.44.5448). URL: <https://link.aps.org/doi/10.1103/PhysRevA.44.5448> (visited on 06/24/2020).

5 | Conclusion and future work

	Dipole Polarizability (α_d)	Quadrupole Polarizability (α_q)	Reference
This Work (Adiabatic Approximation)	9.059(6)	19.1(5)	[1]
Previous Work (Adiabatic Approximation)	9.12(2)	14(3)	[2]
This Work (Non-Adiabatic Correction)	9.061(8)	43(2)	[1]
Previous Work (Non-Adiabatic Correction)	9.12(3)	36(4)	
This & Previous Work (Non-Adiabatic Correction)	9.068(8)	42(2)	[1]
Other Experiments	9.1(2)	$0 < \alpha_q < 43$	[3]
	9.1(6)	$0 < \alpha_q < 55$	[4]
	8.98		[5]
Theory	9.1	35.4	[6]
	9.076	35.41	[7]
	10.22		[8]
		38.43	[9]

TABLE 5.1: Compiled core polarizability results with the non-adiabatic corrected experimental results in this work, along with the adiabatic approximated results, as well as previous experimental results and theory.

5.1 Summary of results

A more precise measurement and more accurate analysis of core polarizability has been achieved using microwave spectroscopy of high- ℓ Rydberg states of Rb. The improved precision and persistent discrepancy with theory has led to the consideration of the non-adiabatic effect in this work. Table 5.1 shows a compilation of dipole and quadrupole polarizability results of previous work and theory, including both adiabatic approximated result and non-adiabatic corrected result found here.

The improved experimental results provide a valuable insight into core polarizability when comparing to theoretical calculations. Theoretical calculations show a dipole polarizability term commensurate with these experimental results; and the previous discrepancy between the theoretically calculated and experimentally determined quadrupole polarizability term has been resolved. The cogent inclusion of dynamic core polarization effects due to the motion of the Rydberg electron are presented through a formulation and application of non-adiabatic corrections treated as a perturbation to the adiabatic-approximated core polarizability. Typically, this effect is large for alkaline-earth metal atoms when compared to alkali metal atoms. For alkali metals, the ionic core has a closed electronic shell with energy spacing between the ion ground state and excited state approximately 20 times larger than the Rydberg electron states. Previously, the assumption had been made that the adiabatic approximation was sufficient for alkali metals; however, it is found here that this effect is non-negligible. The energy span of the Rydberg electron states and continua are approximately 15% that of the energy difference between the Rb^+ ionic core ground and effective excited state. For a sense of energy scales, the lowest lying excited state of the Rb^+ ionic core is 16.53 eV, the effective ionic core energy spacing is 28.76 eV, and the energy span of the Rydberg electron states and continua are 4.31 eV. To account for non-adiabatic effects, correction factors $k_{d,n\ell}$ and $k_{q,n\ell}$ are introduced to the adiabatic polarization energy. For the adiabatic approximation, $k_{d,n\ell} \rightarrow 1$ and $k_{q,n\ell} \rightarrow 1$ when

the energy span between the Rydberg electron radial matrix elements is small compared to the ionic core.

This approach requires determination of a single effective ion state energy above the ground state, dependent upon knowledge of oscillator strengths for the Rb^+ ion. Unfortunately, oscillator strengths for the Rb^+ ion are not well known, and a novel methodology is employed to calculate the effective single ion excited energy state with limited knowledge. This approach involves comparing the well-known photoionization cross-sections for the rubidium ionic core to well-known photoionization cross-sections and oscillator strengths for isoelectronic neutral krypton. Photoionization cross-sections are proportional to the derivative of oscillator strengths with respect to energy; thereby, a rough estimate for oscillator strengths are obtained.

Taking this non-adiabatic correction into account and finding correction factors $k_{d,n\ell}$ and $k_{q,n\ell}$ yields core polarizability results of $\alpha_d = 9.068(8) a_0^3$ and $\alpha_q = 42(2) a_0^5$. Dipole polarizability is minimally affected by the non-adiabatic correction; however, quadrupole polarizability is greatly impacted. Core polarizability obtained in this experiment and analysis is now in agreement with theory with the inclusion of non-adiabatic corrections, and the prior discrepancy between previous experiments and theory is resolved. Given the successful results by including the non-adiabatic effects leading to an agreement between experiment and theory, credence is lent to the theory.

5.2 Comparison to previous work

Core polarizability results in the adiabatic limit measured in this work are approximately three times more precise for the dipole polarizability term and six times more precise for the quadrupole polarizability term when compared to the previous experiment [2]. The improvement in precision is largely due to experimental design choices to reduce systematic effects that greatly impact spectroscopic measurement precision and accuracy

– namely sensitivity to external stray electric fields. Along the same vein of improvement over the previous experiment, the previous experimental data was re-analyzed in the same fashion performed in this research. Using the same methodology of calculating uncertainty in the adiabatic approximated core polarization model here, dipole and quadrupole polarizability results of the previous research are found to be $\alpha_d = 9.12 \pm 0.04$ and $\alpha_q = 13.7 \pm 3.7$. This uncertainty is approximately two times greater than what was reported for both the dipole and quadrupole polarizability terms. Therefore, it is possible that the experiment described in this thesis is six times more precise when considering dipole polarizability and twelve times more precise when considering quadrupole polarizability compared to previous experimental results.

The core polarizability analysis with the non-adiabatic correction is performed for both this work and the previous experiment to obtain a further comparison. The results are displayed in Table 5.1. The results are still more precise in this experiment and in reasonable agreement, with α_d differing by 1.6 standard deviations and α_q differing by 1.2 standard deviations. When comparing these results to theoretical calculations, the result of the previous experiment is in better agreement with theory with respect to the quadrupole polarizability term.

5.3 Future work

Improvements to measurements will only be useful if non-adiabatic correction calculations can be made. Improving experimental precision and reducing sources of systematic uncertainty are important; however, the dominant source of uncertainty is the knowledge of $k_{d,n\ell}$ and $k_{q,n\ell}$. Therefore, the ideal scenario to reduce uncertainty and improve accuracy would be a more sophisticated theoretical atomic structure calculation to account for non-adiabatic effects, or at the very least a better knowledge of Rb^+ oscillator strengths. This

would allow for improved core polarizability results using the existing measurements presented here.

Although this experiment resulted in a marked improvement in measurement accuracy, additional improvements can be made. Background electric and magnetic fields present the largest source of systematic uncertainty. To improve measurement fidelity, Stark shifts can be better controlled with an improved mechanism in the apparatus to adjust electric field in the transverse direction to the existing electric field plates. The most straightforward method would be to place additional electric field plates perpendicular to the existing plates or electrodes of a differing geometry to better null background electric fields [10]. To reach a precision of 100 kHz for the $nf \rightarrow ni$ transition, there would need to be a factor of 4 improvement of stray electric fields. Another method to reduce Stark shifts is to use a lower principal quantum number n . However, several additional experimental challenges present with this approach. Lower n would require a higher amplitude field ionization pulse and higher microwave frequencies.

If systemic shifts such as dc Stark shifts are reduced, statistical error can also be improved by reducing the spectroscopic linewidth. This can be achieved by using a longer microwave pulse duration. To achieve this, a mechanism to better control linewidth broadening from Zeeman effects would also be necessary. In the current configuration, Zeeman spectral line splitting is not resolved, but with longer microwave pulses resulting in lower transform spectral broadening, magnetic shielding or bias coils would be required to reduce Zeeman energy shifts. To achieve the same 100 kHz target, magnetic fields would have to be reduced by a factor of 3. Another method to reduce linewidths may include using cold atoms with continuous wave lasers. Narrower lineshapes and improvements in fine structure resolution may be possible over the current apparatus.

Another possibility to improve upon the current experiment is to excite to higher ℓ states. Core penetration effects will be further diminished and there would be additional points on the polarizability plot to fit to a line. This would also provide another method

for determining whether the ng states are penetrating. Accuracy of the core polarizability analysis would also be improved. These measurements pose additional challenges within the current experimental setup. The signal-to-noise ratio for $nf \rightarrow nj$ state transitions will be lower than the other ℓ states measured in this work, knowing that SNR decreases as ℓ increases. Furthermore, the measurement uncertainty δW is limited by the factors presented above and remains fairly consistent, but the level spacing ΔW decreases as ℓ increases. Therefore, the relative uncertainty $\delta W / \Delta W$ increases with the decreased energy spacing between the higher ℓ states.

A possible method to alleviate the need for spectroscopy measurements of higher ℓ states would be an absolute spectroscopy measurement of the nf state. The current apparatus does not allow for $nd \rightarrow nf$ transitions due to inaccessible microwave transition frequencies; however, absolute measurements of the nf states are possible given existing precise spectroscopic measurements for the nd states [11]. To support this method, either direct optical spectroscopy of the nf states or high frequency microwave spectroscopy of the $nd \rightarrow nf$ transition can be performed.

5.4 Impact of this work

The broader impact of this work is also considered. An explicit motivation for this work is to improve atom polarizability results from previous tune-out wavelength experiments and hopefully provide incentives for another atomic parity violation experiment. The original tune-out wavelength spectroscopy analysis presented in Ref. [12] used a dipole polarizability value of $\alpha_d = 9.08(10) a_0^3$ to determine the ratio of dipole matrix elements between the $5s_{1/2}$ and $5p_{3/2}$ states. Considering the improved measurements obtained in this analysis, the relative uncertainty in the dipole matrix element ratio is reduced by 20%, from 18 ppm to 14 ppm. Several factors that contribute to the uncertainty ratio are difficulty calibrating polarizability with an incident electric field, core polarization, and a correction

accounting for core-valence interactions. Significantly, the core polarization contribution uncertainty was the single largest; however, this is no longer the case. This reduction in uncertainty allows motivation to shift to constraining additional valence dipole matrix elements for Rb to support an atomic parity violation experiment with Rb.

References

- [1] S. J. Berl et al. “Core polarizability of rubidium using spectroscopy of the ng to nh , ni Rydberg transitions”. In: *arXiv:2004.08226 [physics]* (Apr. 2020). arXiv: 2004.08226. URL: <http://arxiv.org/abs/2004.08226> (visited on 06/03/2020).
- [2] Jeonghun Lee, J. Nunkaew, and T. F. Gallagher. “Microwave spectroscopy of the cold rubidium $(n + 1) d_{5/2} \rightarrow n g$ and $n h$ transitions”. en. In: *Physical Review A* 94.2 (Aug. 2016), p. 022505. ISSN: 2469-9926, 2469-9934. DOI: [10.1103/PhysRevA.94.022505](https://doi.org/10.1103/PhysRevA.94.022505). URL: <https://link.aps.org/doi/10.1103/PhysRevA.94.022505> (visited on 05/25/2020).
- [3] Jianing Han et al. “Rb $n f$ quantum defects from millimeter-wave spectroscopy of cold Rb 85 Rydberg atoms”. en. In: *Physical Review A* 74.5 (Nov. 2006), p. 054502. ISSN: 1050-2947, 1094-1622. DOI: [10.1103/PhysRevA.74.054502](https://doi.org/10.1103/PhysRevA.74.054502). URL: <https://link.aps.org/doi/10.1103/PhysRevA.74.054502> (visited on 06/03/2020).
- [4] L. A. M. Johnson. “Precision laser spectroscopy of rubidium with a frequency comb”. In: 2011.
- [5] I. Johansson. In: *Ark. Fys.* 20.135 (1961).
- [6] M. S. Safronova and U. I. Safronova. “Critically evaluated theoretical energies, lifetimes, hyperfine constants, and multipole polarizabilities in Rb 87”. en. In: *Physical Review A* 83.5 (May 2011), p. 052508. ISSN: 1050-2947, 1094-1622. DOI: [10.1103/PhysRevA.83.052508](https://doi.org/10.1103/PhysRevA.83.052508). URL: <https://link.aps.org/doi/10.1103/PhysRevA.83.052508> (visited on 06/06/2020).
- [7] W.R. Johnson, Dietmar Kolb, and K.-N. Huang. “Electric-dipole, quadrupole, and magnetic-dipole susceptibilities and shielding factors for closed-shell ions of the He, Ne, Ar, Ni (Cu+), Kr, Pb, and Xe isoelectronic sequences”. en. In: *Atomic Data and Nuclear Data Tables* 28.2 (Mar. 1983), pp. 333–340. ISSN: 0092640X. DOI: [10.1016/](https://doi.org/10.1016/)

- 0092-640X(83)90020-7. URL: <https://linkinghub.elsevier.com/retrieve/pii/S0092640X83900207> (visited on 06/26/2020).
- [8] Jean Heinrichs. “Simple Calculation of Polarizabilities, Hyperpolarizabilities, and Magnetic Susceptibilities of Atoms and Ions”. en. In: *The Journal of Chemical Physics* 52.12 (June 1970), pp. 6316–6319. ISSN: 0021-9606, 1089-7690. DOI: [10.1063/1.1672943](https://doi.org/10.1063/1.1672943). URL: <http://aip.scitation.org/doi/10.1063/1.1672943> (visited on 06/25/2020).
- [9] R. M. Sternheimer. “Quadrupole Polarizabilities of Various Ions and the Alkali Atoms”. en. In: *Physical Review A* 1.2 (Feb. 1970), pp. 321–327. ISSN: 0556-2791. DOI: [10.1103/PhysRevA.1.321](https://doi.org/10.1103/PhysRevA.1.321). URL: <https://link.aps.org/doi/10.1103/PhysRevA.1.321> (visited on 06/25/2020).
- [10] A. Osterwalder and F. Merkt. “Using High Rydberg States as Electric Field Sensors”. en. In: *Physical Review Letters* 82.9 (Mar. 1999), pp. 1831–1834. ISSN: 0031-9007, 1079-7114. DOI: [10.1103/PhysRevLett.82.1831](https://doi.org/10.1103/PhysRevLett.82.1831). URL: <https://link.aps.org/doi/10.1103/PhysRevLett.82.1831> (visited on 07/01/2020).
- [11] Wenhui Li et al. “Millimeter-wave spectroscopy of cold Rb Rydberg atoms in a magneto-optical trap: Quantum defects of the ns , np , and nd series”. en. In: *Physical Review A* 67.5 (May 2003), p. 052502. ISSN: 1050-2947, 1094-1622. DOI: [10.1103/PhysRevA.67.052502](https://doi.org/10.1103/PhysRevA.67.052502). URL: <https://link.aps.org/doi/10.1103/PhysRevA.67.052502> (visited on 07/01/2020).
- [12] R. H. Leonard et al. “High-precision measurements of the Rb 87 D -line tune-out wavelength”. en. In: *Physical Review A* 92.5 (Nov. 2015), p. 052501. ISSN: 1050-2947, 1094-1622. DOI: [10.1103/PhysRevA.92.052501](https://doi.org/10.1103/PhysRevA.92.052501). URL: <https://link.aps.org/doi/10.1103/PhysRevA.92.052501> (visited on 07/01/2020).

A | Rubidium core polarization paper submitted for publication

Core polarizability of rubidium using spectroscopy of the ng to nh, ni Rydberg transitions

S.J. Berl, C.A. Sackett,* and T.F. Gallagher

Department of Physics, University of Virginia, Charlottesville, Virginia 22904, USA

J. Nunkaew

Thailand Center of Excellence in Physics, Ministry of Higher Education, Science, Research and Innovation, 328 Si Ayuthaya Road, Bangkok, 10400, Thailand

(Dated: April 20, 2020)

We present a precise measurement of the rubidium ionic core polarizability. The results can be useful for interpreting experiments such as parity violation or black-body radiation shifts in atomic clocks since the ionic core electrons contribute significantly to the total electrical polarizability of rubidium. We report a dipole polarizability $\alpha_d = 9.063 \pm 0.007 a_0^3$ and quadrupole polarizability $\alpha_q = 43 \pm 2 a_0^5$ derived from microwave and radio-frequency spectroscopy measurements of Rydberg states with large angular momentum. By using a relatively low principal quantum number ($17 \leq n \leq 19$) and high angular momentum ($4 \leq \ell \leq 6$), systematic effects are reduced compared to previous experiments. We account for non-adiabatic corrections to the polarizability model, which resolves a previous discrepancy with theory but limits the accuracy of our results.

I. INTRODUCTION

The electric polarizability of an atom is of significant interest and importance. Accurate polarizability values are needed for many experiments, including atomic clocks, quantum computation, parity-nonconservation, thermometry, and studies of long-range molecules [1–5]. Polarizability measurements are also useful as benchmarks for theoretical calculations since the polarizability depends on the dipole matrix elements of the atomic wave functions, which are difficult to obtain using conventional spectroscopy. Calculation of matrix elements from first principles is very challenging for multi-electron atoms, so comparisons to experimental quantities, like polarizabilities, provide important checks. These motivations have prompted a series of improving polarizability measurements over the past several decades [6–13]. One promising new approach is tuneout spectroscopy [14], where the ac electric polarizability of an atom vanishes and the wavelength at which that occurs is measured. This technique can provide orders of magnitude improvement in the accuracy of the dipole matrix elements [10, 11, 13, 15].

Theoretical interpretation of the polarizability is simplest for alkali atoms, where most of the effect comes from the single valence electron. However, the contribution of the core electrons cannot be ignored. For instance, the core contributes about 3% to the total polarizability of a Rb atom [3], which is large compared to the 0.2% accuracy of a measurement such as in Ref. [9]. It can be useful to evaluate and subtract the core contribution from a measurement to obtain the valence polarizability alone since this provides the most direct connection to the matrix elements of the valence wave functions. This

approach has been used with both dc and tuneout measurements [10], but it is limited by the accuracy to which the core polarizability is known. We present here a new experimental measurement of the core polarizability of Rb, with an accuracy approximately three times better than previously achieved. We expect this to be useful as tune-out spectroscopy and other polarizability measurement techniques continue to improve.

The core polarizability is obtained in our experiment through microwave spectroscopy of atomic Rydberg states. When the valence electron is far from the core, the atom behaves much like hydrogen; however, the field from the electron polarizes the core and lowers the atomic energy. By comparing the energy of the actual atom to hydrogen, the core polarizability can be determined [16, 17]. This method was previously used in Rb with Rydberg states having principle quantum number n in the range of 27 to 30 [12]. The accuracy of the spectroscopy measurements was principally limited by Stark shifts from stray dc electric fields. The dc polarizability of a Rydberg atom as a whole is very large, so even fields below 1 V/cm can be significant [12]. To address this problem, the work here uses lower principal quantum numbers: $n = 17$ to 19. Since the atomic polarizability scales as n^7 , this reduces the electric field sensitivity by a factor of about 25 compared to previous work.

Because the valence electron produces a non-uniform field at the ion core, the energy of the Rydberg atom depends on both the dipole polarizability α_d and the quadrupole polarizability α_q of the core [18]. We use microwave spectroscopy to determine both of these parameters, and our results are consistent with previous measurements and theory [3, 12].

The Rydberg electron is moving, so its energy shift involves the dynamic, not just the static, polarizability of the core [19]. Since the Rydberg Bohr frequencies are much lower than the excitation frequencies of the core, this effect is small. We nonetheless find that it has a

arXiv:2004.08226v1 [physics.atom-ph] 17 Apr 2020

*Electronic address: sackett@virginia.edu

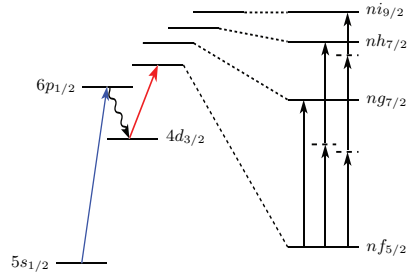


FIG. 1: Atomic states used in the measurement. Rubidium atoms in the $5s_{1/2}$ ground state are optically excited to $6p_{1/2}$, allowed to spontaneously decay to $4d_{3/2}$, and are then optically driven to the $nf_{5/2}$ Rydberg state for $n = 17 - 19$. The expanded diagram on the right shows microwave transitions from nf to ng , nh , and ni states using one, two, and three photon excitations, respectively. The $f - g$ interval is about 15 GHz, the $g - h$ interval is about 3 GHz, and the $h - i$ interval is about 1 GHz; the precise values depend on n .

significant impact on the quadrupole polarizability term. We develop an empirical approximation to account for this non-adiabatic effect, and using it we obtain good agreement with theoretical estimates for both the dipole and quadrupole core polarizabilities.

In the sections that follow, we describe the principle and setup of the experiments, the spectroscopic results, the analysis of the polarizabilities, and finally our conclusions.

II. EXPERIMENTAL APPROACH

In order to interpret the energy shifts of the Rydberg state in terms of the core polarizability, it is necessary for the valence electron to remain far from the core at all times. In addition to large n , this also requires the use of large angular momentum quantum number ℓ . Core penetration in a Rydberg state causes its fine structure splitting to differ significantly from that of hydrogen. Such distortions are observed in Rb for $\ell \leq 3$, so we use only states with $\ell \geq 4$. The atoms are excited using the scheme shown in Fig. 1 where a laser pulse first excites atoms from the $5s_{1/2}$ ground state to the $6p_{1/2}$ excited state. About a third of the excited atoms spontaneously decay to the long-lived $4d_{3/2}$ state, from which they are excited by a second laser pulse to the $nf_{5/2}$ Rydberg state. From there, microwave and radio frequency pulses drive transitions to the ng , nh and ni states. We use the $g - h$ and $h - i$ intervals to determine the dipole (α_d) and quadrupole (α_q) polarizabilities of Rb^+ .

The experiment is performed in an atomic beam apparatus, shown in Fig. 2. The Rydberg atoms are produced between two electric field plates separated by 1.5 cm. A

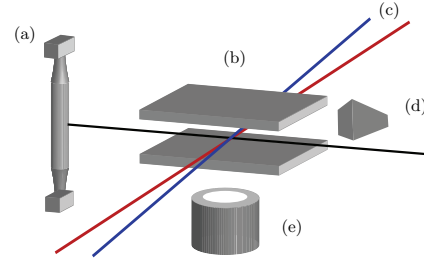


FIG. 2: Experimental apparatus (not to scale). A rubidium atomic beam is emitted from oven (a) and passes between electric field plates (b), which are separated by 1.5 cm. Two pulsed laser beams (c) excite the atoms into Rydberg states, and microwave horn (d) drives Rydberg state transitions. An electric field is applied to ionize the Rydberg atoms, and the ions are detected with microchannel plate (e).

potential difference of up to 6 kV can be applied between the plates. After the microwave pulse is applied, the electric field is ramped to a value sufficient to ionize the Rydberg states. By carefully controlling the timing and amplitude of the ramp, the atom ionization process can be made state selective such that atoms in $\ell \geq 4$ states are ionized while the nf atoms remain neutral. Any ions produced are detected using a microchannel plate operating in analog mode with spatially integrated channels. The resulting signal current is accumulated using a gated integrator to produce the spectroscopy signal.

The laser excitation pulses are produced by a pair of home-built dye lasers. The first pulse is at a wavelength of 420 nm, and is produced using Stilbene 420 dye pumped by the third harmonic of a Quanta Ray Nd:YAG laser. The second pulse is tuned between 713 nm and 720 nm to populate the desired nf state. This laser uses LD720 dye, pumped by the second harmonic of a Continuum Nd:YAG laser. Both laser pulses have 20 ns duration, and the second pulse is delayed by 250 ns with respect to the first. Both lasers are linearly polarized perpendicular to the field plates. While the $6p$ fine structure is resolved by laser tuning, the nf fine structure is not.

The lifetimes of the nf states are about $4 \mu\text{s}$ with an n^3 dependence, and the microwave spectroscopy pulses are applied $1 \mu\text{s}$ after the second laser pulse. In the case of the nf to ng transition, a single-photon transition is driven with a microwave frequency ranging from 11 to 17 GHz, depending on n . For the nf to nh transition, a two-photon transition is driven with microwaves at half the transition frequency, between 7 and 10 GHz. For the three-photon nf to ni transition, the two-photon microwave frequency is detuned from the nh state, and apply an RF frequency near 1 GHz to couple nh to ni . These three excitation schemes are illustrated in Fig. 1. The microwaves are produced by an Agilent

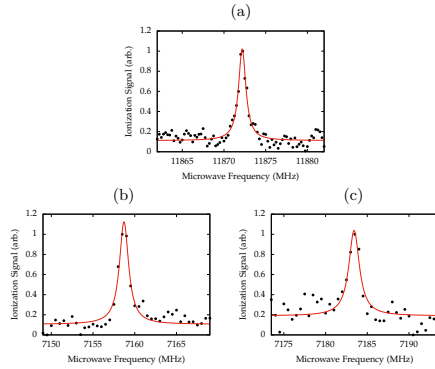


FIG. 3: Example spectroscopy line profiles. (a) Single-photon $19f_{5/2} \rightarrow 19g_{7/2}$. (b) Two-photon $19f_{5/2} \rightarrow 19h_{9/2}$. (c) Three-photon $19f_{5/2} \rightarrow 19i_{11/2}$.

83622B frequency synthesizer coupled to one of two microwave horns. The RF field is produced by coupling a HP 8673C synthesizer to one of the electric field plates. In all cases, the duration of the spectroscopy pulse is $1 \mu\text{s}$.

For each measurement, the microwave frequency was swept across the resonance. Each frequency step in the sweep was repeated at least ten times, and the sweep in its entirety was repeated five times. The resulting signals were averaged to produce a line profile, such as the example data shown in Fig. 3. The profiles were least-squares fit to Lorentzian functions to determine the line centers. Uncertainty in the line center was taken from the uncertainty estimate of the fit. However, in cases where the line center uncertainty from the fit was below 10% of the fit linewidth, we instead assigned an uncertainty of 10% of the linewidth to reflect the fact that the actual lineshape is not well characterized.

Several sources of systematic uncertainty must be taken into account, including dc Stark shifts, ac Stark shifts, Zeeman shifts, and fine structure splitting.

Although dc Stark shifts are reduced by operating at relatively low n , they must still be accounted for. The conducting field plates suppress electric fields parallel to the plates, but any residual voltage difference produces a significant field normal to the plates. We are able to apply a bias voltage across the plates during the experiment, and Fig. 4(a) shows how the $nf \rightarrow ng$ transition frequency varies as a function of the bias voltage. We fit such data to a parabola and then set the bias voltage to the vertex of the fit. We perform this calibration daily, and observe day-to-day variations of about 0.25 V/cm , corresponding to Stark shifts of the $nf \rightarrow ng$ transition on the order of 0.1 MHz . The apparatus provides no direct way to measure or control the transverse electric field components, but other experiments with similar geome-

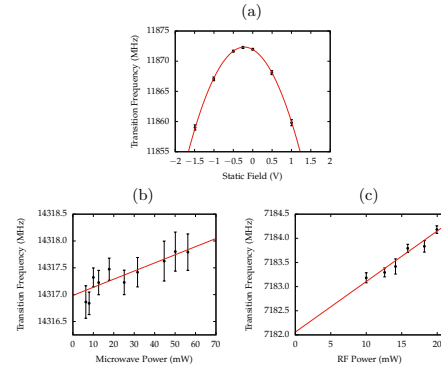


FIG. 4: a) Measurement of the dc Stark shift on the $19f_{5/2} \rightarrow 19g_{7/2}$ transition. For spectroscopy, the bias voltage is set to the vertex of the curve. b) Measurement of the ac Stark shift on the two-photon $19f_{5/2} \rightarrow 19h_{9/2}$. The line is a linear fit showing the extrapolation to zero microwave power. d) Measurement of the ac Stark shift due to the rf field on the three-photon $19f_{5/2} \rightarrow 19i_{11/2}$ transition, for a two-photon microwave detuning of 45.9 MHz . The line is again a linear fit.

tries show that the transverse fields are typically below 0.1 V/cm [12], corresponding to a shift here of less than 0.04 MHz .

There are no ac Stark shifts on the single-photon nf to ng transitions, but there are on the multiphoton transitions. These shifts are manifested as a function of microwave or rf power. We compensate for it by taking data over a range of powers and extrapolating the results to zero power. Example data are shown in Fig. 4(b) and (c). The ac Stark shift is largest for the three-photon $nf \rightarrow ni$ transition, and the shift depends on the two-photon detuning from the nh state. For these measurements, the microwave and rf powers were independently varied and extrapolated to zero. In addition, for each n we used at least two different two-photon detuning values, with at least one on each side of the h state resonance. The values obtained were consistent with the estimated uncertainties. In all cases, the extrapolation to zero power was performed using an error-weighted least squares fit to the data, and the uncertainty from this fit is reported as the uncertainty in the transition frequency measurement. The resulting values are reported in Table I. For the majority of transitions reported here, at least two measurements were completed on different days, and the results agreed within the stated uncertainty.

Zeeman shifts are nominally zero, since the linearly polarized laser beams produce a symmetric distribution of m levels, and the microwave and rf fields are also linearly polarized. In this case, a magnetic field would only

broaden the transition to first order. We computed the second-order Zeeman shift and the second-order coupling between the Zeeman and dc Stark shift, and found both to be negligible for our environmental field of about 1 G. We experimentally verified these conclusions by applying a dc field of 1 G and observed no linear shift on the $17f$ to $17g$ transition. On this basis, we ignore the Zeeman effect as a source of uncertainty.

In hydrogen, the fine structure (FS) splittings of the ng , nh and ni states range from 3.0 MHz to 0.6 MHz. This is comparable to or less than our experimental linewidth, so the fine structure is not well resolved, but it is significant compared to our measurement accuracy. To avoid uncertainty due to unresolved FS we take advantage of the fact that the excitation scheme of Fig. 1 ensures that the Rydberg atoms are always in the lower j fine structure state, $j = \ell - 1/2$. Accordingly, we have measured the intervals given in Table I.

We expect the $\ell \geq 4$ FS splittings in Rb to be similar to those of hydrogen, because the $\ell \geq 4$ states should not penetrate the core and the core polarization effect is independent of j . To verify this, we retuned the initial laser excitation pulse to the $6p_{3/2}$ state, which then allowed excitation of both the $nf_{5/2}$ and $nf_{7/2}$ states. The $nf_{7/2} \rightarrow ng_{7/2}$ transition is suppressed due to small Clebsch-Gordan coefficients, but we observed the $nf_{7/2} \rightarrow ng_{9/2}$ transition. Using the known f -state FS splitting [20], we obtained a value for the $17g$ FS splitting of 1.83 ± 0.06 MHz. This is in agreement with the hydrogenic value of 1.78 MHz and is consistent with the g -states being non-penetrating [21]. We therefore use the hydrogen FS values for the $\ell > 4$ states. For the analysis described below, we use transition frequencies from which the FS shift has been removed by referencing the transition to the center of gravity of the FS manifold. These frequencies are listed in Table I.

III. ANALYSIS & DISCUSSION

In the adiabatic core polarization model the electric field from the quasistatic charge distribution of the Rydberg $n\ell$ electron polarizes the ion core, which results in the polarization energy shift of the Rydberg $n\ell$ state relative to the hydrogenic $n\ell$ energy. The shift is given, in atomic units, by [17, 22]

$$W = -\frac{1}{2}\alpha_d^{(a)} \left\langle \frac{1}{r^4} \right\rangle_{n\ell} - \frac{1}{2}\alpha_q^{(a)} \left\langle \frac{1}{r^6} \right\rangle_{n\ell}, \quad (1)$$

where $\alpha_d^{(a)}$ and $\alpha_q^{(a)}$ are the dipole and quadrupole core polarizabilities of Rb^+ , and r is the distance of the valence electron from the nucleus. The superscript denotes the use of the adiabatic approximation, which will be subsequently relaxed. If we assume the $n\ell$ wavefunctions to be hydrogenic, there are closed form expressions for the required expectation values [17, 22, 23]. As a result, it is a straightforward matter to extract $\alpha_d^{(a)}$ and $\alpha_q^{(a)}$ from

the high ℓ Rydberg energies.

Equation (1) gives the energy shift of a state relative to the corresponding state of hydrogen, but we do not have accurate values for the absolute energies of the nf states, so we cannot evaluate the energies of the high- ℓ states relative to hydrogen. Instead, we consider the energy difference between two states $n\ell$ and $n\ell'$. Since the hydrogenic energies are independent of ℓ , the energy difference is

$$\Delta W = -\frac{1}{2}\alpha_d^{(a)} \Delta_d^{(a)} - \frac{1}{2}\alpha_q^{(a)} \Delta_q^{(a)}, \quad (2)$$

where

$$\Delta_d^{(a)} \equiv \left\langle \frac{1}{r^4} \right\rangle_{n\ell} - \left\langle \frac{1}{r^4} \right\rangle_{n\ell'} \quad (3)$$

and

$$\Delta_q^{(a)} \equiv \left\langle \frac{1}{r^6} \right\rangle_{n\ell} - \left\langle \frac{1}{r^6} \right\rangle_{n\ell'} \quad (4)$$

The energy difference ΔW corresponds to the FS-corrected transition frequencies reported in Table I.

To obtain the polarizabilities, we plot $2\Delta W/\Delta_d^{(a)}$ vs. $\Delta_q^{(a)}/\Delta_d^{(a)}$, for (ℓ, ℓ') pairs (4, 5) and (5, 6), with the results shown in Fig. 5. The subfigures detail the n dependence and show the least squares fit along with the data. The points are fit to a line, and the resulting intercept and slope correspond to $\alpha_d^{(a)} = 9.059(3) a_0^3$ and $\alpha_q^{(a)} = 19.1(3) a_0^5$. These are in reasonable agreement (3 standard deviations) with previous results $\alpha_d^{(a)} = 9.12(2)$ and $\alpha_q^{(a)} = 14(3)$ [12], but with reduced uncertainty.

However, we find that the adiabatic approximation is inadequate here and must be corrected to incorporate non-adiabatic effects [19, 24–27]. The non-adiabatic correction arises because Eq. (1) is an approximation to the second-order shift from the multipole expansion of the Coulomb interaction between the Rb^+ ion core and the Rydberg electron. The same method of analyzing the experimental data can be used if we introduce correction factors $k_{d,n\ell}$ and $k_{q,n\ell}$ into Eq. (1), which then reads [22]

$$W = -\frac{1}{2}k_{d,n\ell}\alpha_d \left\langle \frac{1}{r^4} \right\rangle_{n\ell} - \frac{1}{2}k_{q,n\ell}\alpha_q \left\langle \frac{1}{r^6} \right\rangle_{n\ell}. \quad (5)$$

In the adiabatic approximation, $k_{d,n\ell} = k_{q,n\ell} = 1$

To show the origin of the non-adiabatic correction we consider the contribution of the dipole polarizability to the polarization shift of a Rb $n\ell$ state [25, 28]. The atomic wavefunction is taken to be a direct product of the ion wavefunction and a hydrogenic wavefunction for the Rydberg electron. Consequently, the total energy is simply the sum of the ion and Rydberg energies. In a bound Rb $n\ell$ state, the Rydberg electron is coupled to the ground $4p^6$ state of Rb^+ , which we denote as a , so the bound Rydberg state is denoted $an\ell$. Similarly, a Rydberg $n'\ell'$ electron coupled to an excited state b of Rb^+

TABLE I: Measured transition frequencies and frequencies referenced to the center of gravity of the fine-structure doublet in MHz for $n = 17 - 19$, $f \rightarrow g$, $f \rightarrow h$, and $f \rightarrow i$.

n	$f_{5/2} \rightarrow g_{7/2}$	$f_{cg} \rightarrow g_{cg}$	$f_{5/2} \rightarrow h_{9/2}$	$f_{cg} \rightarrow h_{cg}$	$f_{5/2} \rightarrow i_{11/2}$	$f_{cg} \rightarrow i_{cg}$
17	16528.66(3)	16547.27(7)	19929.5(3)	19947.8(3)	20992.5(6)	21010.6(6)
18	13945.16(9)	13960.90(10)	16815.6(1)	16831.0(2)	17713.2(6)	17728.5(6)
19	11872.25(6)	11885.69(7)	14317.0(1)	14330.2(1)	15082.9(8)	15096.0(8)

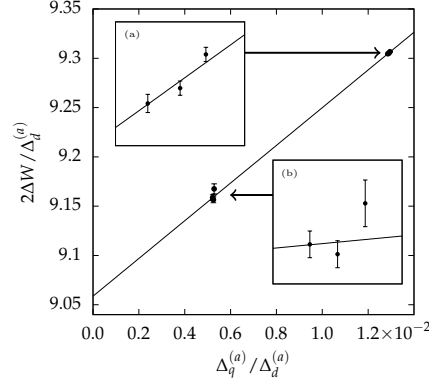


FIG. 5: Determination of core polarizabilities in the adiabatic approximation. In the main plot, ΔW is the measured energy interval between states $n\ell$ and $n'\ell'$. The parameters $\Delta_d^{(a)}$ and $\Delta_q^{(a)}$ depend on n , ℓ and ℓ' , and are given by Eqs. (3) and (4). The side plots show expanded views of the data for the (a) $g-h$ and (b) $h-i$ transitions. The line is an error-weighted best fit, with intercept and slope corresponding to $\alpha_d^{(a)}$ and $\alpha_q^{(a)}$, respectively. The present values are $\alpha_d^{(a)} = 9.059(3) a_0^3$ and $\alpha_q^{(a)} = 19.1(3) a_0^5$.

is denoted $bn'\ell'$. We restrict our attention to ion states which are dipole coupled to the ground state. In the Rydberg atom, the $an\ell$ state is coupled by the dipole term of the Coulomb expansion to the $bn'(\ell-1)$ and $bn'(\ell+1)$ states, as well as the $b\epsilon(\ell-1)$ and $b\epsilon(\ell+1)$ continua. The resulting dipole energy shift of the $4p^6n\ell$, the $an\ell$, state is given explicitly by

$$\Delta W_{d,n\ell} = \frac{1}{3} \sum_{b,n'} \left[\frac{\ell \langle a|r_1|b \rangle^2 \langle n\ell|r_2^{-2}|n'(\ell-1) \rangle^2}{(2\ell+1)(W_{an\ell} - W_{bn'(\ell-1)})} + \frac{(\ell+1) \langle a|r_1|b \rangle^2 \langle n\ell|r_2^{-2}|n'(\ell+1) \rangle^2}{(2\ell+1)(W_{an\ell} - W_{bn'(\ell+1)})} \right], \quad (6)$$

where the sums are understood to include the continua above the Rydberg and ion limits. Here r_1 represents a core electron and r_2 the Rydberg electron. The r_2^{-2}

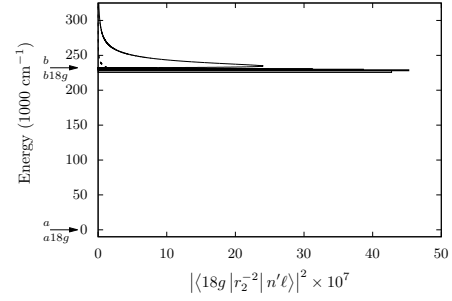


FIG. 6: Energy distribution of the $18g$ Rydberg matrix elements. The vertical axis is the energy of the Rydberg atom, with the core ion ground state a and excited state b indicated by arrows. The energy difference between the ion states and the Rydberg atom states $a18g$ and $b18g$ is too small to resolve. The horizontal axis shows the square matrix elements to the $bn'f$ and $bn'h$ states, and also to the bef and bch continua. The continuum states are normalized per unit energy and the bound states are plotted as boxes normalized per unit energy. Values for the h states are shown with dashed lines, but the f state matrix elements are generally much larger. The energy range over which the matrix elements remains appreciable is seen to be small, but not very small, compared to $W_b - W_a$. Here we take $W_b = 232\,000 \text{ cm}^{-1}$, corresponding to the effective ion excitation energy W_{Id} discussed in the text.

matrix elements are computed using Numerov's method, and their accuracy is verified using the sum rule [25]

$$\langle n\ell|r^{2s}|n\ell \rangle = \sum_{n'} \langle n\ell|r^s|n'\ell' \rangle^2. \quad (7)$$

The energy denominators of Eq. (6) can be rewritten as

$$W_{an\ell} - W_{bn'\ell'} = W_a - W_b + W_{n\ell} - W_{n'\ell'} \quad (8)$$

The adiabatic expression of Eq. (1) is the result of taking $W_{n\ell} - W_{n'\ell'} = 0$, since it is much smaller than $W_b - W_a$. However, the squared $\langle n\ell|r_2^{-2}|n'\ell' \rangle$ matrix elements actually do cover a substantial energy range, as shown by the $18g$ example of Fig. 6. Here the matrix elements cover an energy range that is about 15% of $W_b - W_a$.

Rather than neglecting $W_{n\ell} - W_{n'\ell'}$ entirely, we consider Taylor expanding Eq. (6) with $|W_{n\ell} - W_{n'\ell'}|/|W_a -$

6

W_b as a small parameter. In first order, it is possible to show that the sum over the ion transitions can be replaced by an effective transition to a single ion state at energy W_{Id} above the ground state, with W_{Id} given by

$$\frac{1}{W_{Id}} = \frac{\sum_b \frac{\langle a|r_1|b\rangle^2}{(W_a - W_b)^2}}{\sum_b \frac{\langle a|r_1|b\rangle^2}{W_a - W_b}}, \quad (9)$$

which is an appropriately weighted average of $1/(W_a - W_b)$. Similarly, we can obtain an effective matrix element

$$\langle a|r_1|I\rangle^2 = \frac{\left(\sum_b \frac{\langle a|r_1|b\rangle^2}{W_a - W_b}\right)^2}{\sum_b \frac{\langle a|r_1|b\rangle^2}{(W_a - W_b)^2}}. \quad (10)$$

Replacing the sum over the excited states of the ion with the effective state I allows the ion dipole matrix element to be removed from the sum, leaving

$$\Delta W_{d,n\ell} = \frac{1}{3} \langle a|r_1|I\rangle^2 \sum_{n'} \left[\frac{\ell(n\ell|r_2^{-2}|n'(\ell-1))^2}{(2\ell+1)(W_{an\ell} - W_{In'(\ell-1)})} + \frac{(\ell+1)(n\ell|r_2^{-2}|n'(\ell+1))^2}{(2\ell+1)(W_{an\ell} - W_{In'(\ell+1)})} \right], \quad (11)$$

In practice, it is not necessary to evaluate $\langle a|r_1|I\rangle^2$ since in this approximation, the ion polarizability is itself simply $\langle a|r_1|I\rangle^2/6W_{Id}$.

We do need to determine W_{Id} , which requires a knowledge of the distribution of oscillator strength f_a from the ion ground state. Unfortunately, this is not well known. However, the photoionization cross section, proportional to df_a/dW , is known and similar to the photoionization cross section of the isoelectronic neutral Kr [29, 30]. For Kr the oscillator strengths are known for both the bound states and the continuum [31], and using then we computed W_{Id} for Kr. We find a value 6% higher in energy than the first ionization limit of Kr at $112\,900\text{ cm}^{-1}$. We estimate the value for Rb^+ to also be 6% higher than the ionization limit at $220\,100\text{ cm}^{-1}$, resulting in $W_{Id} = 232\,300\text{ cm}^{-1}$.

Using $\langle a|r_1|I\rangle^2/3 = 2\alpha_d W_{Id}$, we can obtain an expression for k_d as

$$k_{d,n\ell} = \frac{W_{Id}}{\langle n\ell|r_2^{-4}|n\ell\rangle} \sum_{n'} \left[\frac{\ell(n\ell|r_2^{-2}|n'(\ell-1))^2}{(2\ell+1)(W_{an\ell} - W_{In'(\ell-1)})} + \frac{(\ell+1)(n\ell|r_2^{-2}|n'(\ell+1))^2}{(2\ell+1)(W_{an\ell} - W_{In'(\ell+1)})} \right]. \quad (12)$$

The values of k_d computed in this way are given in Table II.

TABLE II: Non-adiabatic correction factors, calculated as in Eq. (12). The lower- n values are relevant to the data taken here, and the higher- n values are for the data of Ref. [12].

n	k_d			k_q		
	$\ell=4$	5	6	4	5	6
17-19	0.978(2)	0.990(1)	0.994(1)	0.921(15)	0.967(7)	0.984(3)
27-30	0.977(2)	0.990(1)		0.921(15)	0.967(7)	

To obtain an estimate of the uncertainty in k_d , we note that W_{Id} is roughly bounded by the lowest ionic excited state energy and the second ionization energy. For instance, a calculation of W_{Id} in atomic hydrogen give a value just above the $1s - 2p$ transition energy, which reflects the fact that this transition contains over half of the total oscillator strength. In contrast, neutral Kr has six times as much oscillator strength in the first 20 eV above the ionization limit as in the bound states [31], which explains why W_{Id} is comparable to the ionization energy in that case. The first excited state of Rb^+ lies at $134\,000\text{ cm}^{-1}$, about 40% below the ionization limit. This sets the scale for the uncertainty range, but we believe the isoelectronic analogy to Kr to be reasonably sound, so we estimate an uncertainty of $\pm 10\%$ for W_{Id} . This translates directly to a 10% uncertainty in $(1 - k_{d,n\ell})$ and provides the uncertainties shown in Table III.

The quadrupole correction factor $k_{q,n\ell}$ is calculated in much the same way as $k_{d,n\ell}$. In this case the $\langle n\ell|r_2^{-3}|n'\ell'\rangle$ matrix elements are required, and they are similarly evaluated numerically for hydrogenic wave functions. To assign an effective energy W_{Iq} accounting for the ionic quadrupole transitions, we use an expression analogous to Eq. (9). Lacking better information, we calculate W_{Iq} for hydrogen and obtain $122\,465\text{ cm}^{-1}$, which is 12% over the ionization limit. Taking the same to be true for Rb^+ we obtain $W_{Iq} = 254\,000\text{ cm}^{-1}$. Using this value of W_{Iq} in the quadrupole analog of Eq. (12), we calculate $k_{q,n\ell}$. Since there is no analog to the Kr oscillator strength distribution for comparison, we assign a $\pm 20\%$ uncertainty to W_{Iq} and thus to $1 - k_{q,n\ell}$. The results are also shown in Table III.

Since we measure energy differences ΔW , we again use Eq. (2), but the definitions of Δ_d and Δ_q now include $k_{d,n\ell}$ and $k_{q,n\ell'}$ and are given by

$$\Delta_d \equiv \frac{1}{2} k_{d,n\ell} \left\langle \frac{1}{r^4} \right\rangle_{n\ell} - \frac{1}{2} k_{d,n\ell'} \left\langle \frac{1}{r^4} \right\rangle_{n\ell'} \quad (13)$$

and

$$\Delta_q \equiv \frac{1}{2} k_{q,n\ell} \left\langle \frac{1}{r^6} \right\rangle_{n\ell} - \frac{1}{2} k_{q,n\ell'} \left\langle \frac{1}{r^6} \right\rangle_{n\ell'}. \quad (14)$$

As before, we plot $\Delta W/\Delta_d$ vs. Δ_q/Δ_d , for (ℓ, ℓ') pairs (4, 5) and (5, 6), with the result shown in Fig. 7. We also include higher- n results for $(\ell, \ell') = (4, 5)$ taken from Ref. [12]. The points are fit to a line, and the resulting

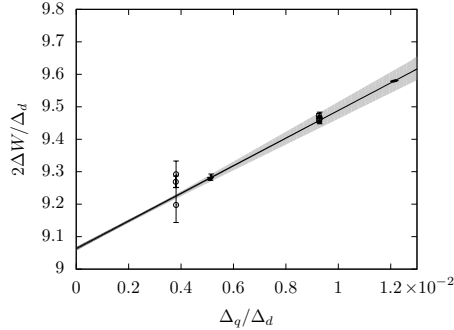


FIG. 7: Determination of core polarizabilities including non-adiabatic corrections. The plot is analogous to that of Fig. 5, but now using Eqs. (13) and (14) for the Δ variables. The data reported here are plotted as filled circles. We also include previous data at higher n from Ref. [12] as open circles. The higher- n data consist of energy shifts relative to hydrogen, rather than energy differences, so for those points we instead plot $2W/(k_{d,n\ell}(r^{-4})_{n\ell})$ vs. $(k_{q,n\ell}(r^{-6})_{n\ell})/(k_{d,n\ell}(r^{-4})_{n\ell})$. All of the points are fit to a line, whose slope and intercept give α_d and α_q . The dark gray band is a graphical representation of line fit errors. The light gray band shows the range of values obtained when k_d and k_q are varied by their uncertainties from Table III.

intercept and slope correspond to $\alpha_d = 9.063(5)$ au and $\alpha_q = 42.5(4)$ au, where the uncertainties are the statistical uncertainties returned by the fit. These values are obtained using the values of k_d and k_q given in Table III, assuming them to be perfectly accurate. We take the uncertainties in the non-adiabatic terms into account by varying W_{Id} and W_{Iq} by their uncertainties and fitting the data again. A $\pm 10\%$ change in W_{Id} leads to a ± 0.004 au change in α_d and a ± 1.7 au change in α_q . A $\pm 20\%$ change in W_{Iq} leads to a ∓ 0.003 au change in α_d and a ± 1.0 au change in α_q . Taking these uncertainties in W_{Id} and W_{Iq} into account, we assign the values $\alpha_d = 9.063(7)$ au and $\alpha_q = 43(2)$ au. Compared to the adiabatic result, the α_d value is slightly increased and the uncertainty is doubled. In contrast, the α_q value is substantially increased and the uncertainty is larger by an order of magnitude. This uncertainty is almost entirely due to the imprecision of W_{Id} and W_{Iq} . The gray band in Fig. 7 illustrates these uncertainties graphically.

Our results can be compared to theoretical estimates. Calculations of the core dipole polarizability range from 9.076 to 9.11 au [3], in reasonable agreement with our result. Estimates of the quadrupole term α_q range from 35.4 to 38.37 au [3], which are again reasonably consistent. This consistency lends support to the approximations made for our non-adiabatic corrections, and it resolves the large discrepancy between theory and the

TABLE III: Quantum defects for $n = 17$ to 19 g, h, i states, and the Ritz expansion coefficients of Eq. (16).

	ℓ	δ
$n = 17$	g	0.003908(2)
	h	0.0013697(5)
	i	0.0005762(2)
18	g	0.003918(2)
	h	0.0013750(5)
	i	0.0005794(2)
19	g	0.003927(2)
	h	0.0013794(5)
	i	0.0005821(2)
δ_0	g	0.004011(1)
	h	0.001424(3)
	i	0.000606(1)
δ_2	g	-0.0299(6)
	h	-0.0156(8)
	i	-0.0086(4)

adiabatic α_q of value 14(3) reported in [12].

Although we measure transition frequencies, we can use the extracted polarizabilities to calculate the absolute energy of the Rydberg states, and thus obtain the quantum defects. For this we use Eq. (1) and the adiabatic polarizability values $\alpha_d^{(a)}$ and $\alpha_q^{(a)}$, since that avoids the uncertainty in the non-adiabatic correction factors. The quantum defects are then found by setting

$$W_{n\ell} = \frac{1}{2n^2} - \frac{1}{2(n - \delta_{n\ell})^2}. \quad (15)$$

The results are listed in Table III. The variation of the quantum defect with n can be parameterized using the Ritz expansion [32]

$$\delta(n) = \delta_0 + \frac{\delta_2}{(n - \delta_0)^2}. \quad (16)$$

By combining our data with those of Ref. [12], we obtain the δ_0 and δ_2 values shown.

IV. CONCLUSIONS

We have demonstrated microwave spectroscopy of the high- ℓ states of Rb with precision improved by a factor of ten compared to previous results, and extending the measurements to $\ell = 6$. Using these data, we determined the dipole and quadrupole polarizabilities of the Rb^+ ionic core, including corrections for non-adiabatic effects. These corrections significantly impact and resolve discrepancies between previous work and theory, particularly for the quadrupole term.

We can consider methods to obtain yet higher accuracy. A straightforward improvement would be to use

a more sophisticated atomic structure calculation to account for the non-adiabatic effects, which would allow more precise polarizability values to be extracted from our existing data. Without such a calculation, improvements to the experiment itself would not be useful.

If the non-adiabatic correction factors can be determined more accurately, then the measurements could be improved in several ways. One possibility is to extend the measurements to higher ℓ states. This would provide more points in Fig. 7 and allow a better test of the underlying core polarization model. However, this is challenging because the signal-to-noise ratio on the $nf \rightarrow nj$ transition would be low in our existing apparatus, and the decreasing value of ΔW makes the relative frequency uncertainty more significant. A different approach would be to perform absolute spectroscopy of the nf state so that the energy shifts relative to hydrogen of the ng , nh and ni states could be used independently. We cannot carry out such spectroscopy with our current apparatus: although precise spectroscopy of the nd states is available [33], at low n values the $nd - nf$ frequency intervals are too large to access with our microwave technology.

The precision of the microwave measurements themselves could be improved by using a longer microwave pulse duration to obtain narrower transitions. This would require magnetic shielding to reduce line broadening from the Zeeman effect, and would benefit from a more complex field plate structure that allowed adjustment of all three components of the background bias field

to better eliminate dc Stark shifts.

We also hope that the improved core polarizability values determined here will be useful for precision measurements such as atomic clocks and tune-out spectroscopy. In regards to our own interest in tune-out spectroscopy, the core polarizability was a source of uncertainty in the determination of the ratio of the $5p_{3/2}$ to $5p_{1/2}$ dipole matrix elements. Our original analysis in [10] used $\alpha_d = 9.08(10)$ au. Using the improved value found here, we reduce the relative uncertainty in the ratio from 18 ppm to 14 ppm, where the core contribution is no longer a significant factor in the uncertainty. The value of the ratio, 1.992 17, remains unchanged. Ultimately, we hope to further use tune-out spectroscopy to constrain all the valence dipole matrix elements of Rb and support a future parity non-conservation measurement [10].

Acknowledgments

This work was supported by National Science Foundation (grant Number PHY-1607571) and the Air Force Office of Scientific Research (grant Number FA9550-14-1-0288). J. Nunkaew was supported by the Thailand Center of Excellence in Physics (ThEP-61-PHY-MU3). It is a pleasure to acknowledge Adam Fallon and Safra Niyaz for useful discussions.

-
- [1] L. J. LeBlanc and J. H. Thywissen, Phys. Rev. A **75**, 053612 (2007), URL <https://link.aps.org/doi/10.1103/PhysRevA.75.053612>.
- [2] J. Mitroy, M. S. Safronova, and C. W. Clark, J. Phys. B: At. Mol. Opt. Phys. **43**, 202001 (2010), ISSN 0953-4075, URL <http://stacks.iop.org/0953-4075/43/i=20/a=202001>.
- [3] M. S. Safronova and U. I. Safronova, Phys. Rev. A **83**, 052508 (2011), URL <https://link.aps.org/doi/10.1103/PhysRevA.83.052508>.
- [4] V. A. Dzuba, V. V. Flambaum, and B. Roberts, Phys. Rev. A **86**, 062512 (2012), URL <https://link.aps.org/doi/10.1103/PhysRevA.86.062512>.
- [5] C. Gaiser and B. Fellmuth, Phys. Rev. Lett. **120**, 123203 (2018), URL <https://link.aps.org/doi/10.1103/PhysRevLett.120.123203>.
- [6] C. R. Ekstrom, J. Schmiedmayer, M. S. Chapman, T. D. Hammond, and D. E. Pritchard, Phys. Rev. A **51**, 3883 (1995), URL <https://link.aps.org/doi/10.1103/PhysRevA.51.3883>.
- [7] A. Miffre, M. Jacquy, M. Büchner, G. Tréneç, and J. Vigué, Phys. Rev. A **73**, 011603 (2006), URL <https://link.aps.org/doi/10.1103/PhysRevA.73.011603>.
- [8] W. F. Holmgren, M. C. Reville, V. P. A. Lonij, and A. D. Cronin, Phys. Rev. A **81**, 053607 (2010), URL <https://link.aps.org/doi/10.1103/PhysRevA.81.053607>.
- [9] M. D. Gregoire, I. Hromada, W. F. Holmgren, R. Trubko, and A. D. Cronin, Phys. Rev. A **92**, 052513 (2015), URL <https://link.aps.org/doi/10.1103/PhysRevA.92.052513>.
- [10] R. H. Leonard, A. J. Fallon, C. A. Sackett, and M. S. Safronova, Phys. Rev. A **92**, 052501 (2015), URL <https://link.aps.org/doi/10.1103/PhysRevA.92.052501>.
- [11] A. Fallon and C. Sackett, Atoms **4**, 12 (2016).
- [12] J. Lee, J. Nunkaew, and T. F. Gallagher, Phys. Rev. A **94**, 022505 (2016), URL <https://link.aps.org/doi/10.1103/PhysRevA.94.022505>.
- [13] R. Trubko, M. D. Gregoire, W. F. Holmgren, and A. D. Cronin, Phys. Rev. A **95**, 052507 (2017), URL <https://link.aps.org/doi/10.1103/PhysRevA.95.052507>.
- [14] B. Arora, M. S. Safronova, and C. W. Clark, Phys. Rev. A **84**, 043401 (2011), URL <https://link.aps.org/doi/10.1103/PhysRevA.84.043401>.
- [15] M. D. Gregoire, N. Brooks, R. Trubko, and A. Cronin, Atoms **4** (2016).
- [16] M. Born and W. Heisenberg, Zeitschrift für Physik **23**, 388 (1924), ISSN 0044-3328, URL <https://doi.org/10.1007/BF01327603>.
- [17] B. Edlén, *Atomic Spectra* (Springer Berlin Heidelberg, Berlin, Heidelberg, 1964), pp. 80–220, ISBN 978-3-662-35391-2, URL https://doi.org/10.1007/978-3-662-35391-2_2.
- [18] J. E. Mayer and M. G. Mayer, Phys. Rev. **43**, 605 (1933), URL <https://link.aps.org/doi/10.1103/PhysRev.43.605>.
- [19] H. Eissa and U. pik, Proceedings of the Physical So-

- ciety **92**, 556 (1967), URL <https://doi.org/10.1088/2F0370-1328/2F92/2F3/2F307>.
- [20] J. Han, Y. Jamil, D. V. L. Norum, P. J. Tanner, and T. F. Gallagher, Phys. Rev. A **74**, 054502 (2006), URL <https://link.aps.org/doi/10.1103/PhysRevA.74.054502>.
- [21] N. H. Tran, H. B. van Linden van den Heuvell, R. Kachru, and T. F. Gallagher, Phys. Rev. A **30**, 2097 (1984), URL <https://link.aps.org/doi/10.1103/PhysRevA.30.2097>.
- [22] T. F. Gallagher, *Rydberg Atoms* (Cambridge University, 1994).
- [23] H. A. Bethe and E. E. Salpeter, *Quantum mechanics of one and two electron atoms* (Springer, 1957).
- [24] J. E. Mayer and M. G. Mayer, Phys. Rev. **43**, 605 (1933), URL <https://link.aps.org/doi/10.1103/PhysRev.43.605>.
- [25] J. H. Van Vleck and N. G. Whitelaw, Phys. Rev. **44**, 551 (1933), URL <https://link.aps.org/doi/10.1103/PhysRev.44.551>.
- [26] R. R. Freeman and D. Kleppner, Phys. Rev. A **14**, 1614 (1976), URL <https://link.aps.org/doi/10.1103/PhysRevA.14.1614>.
- [27] M. Peper, F. Helmrich, J. Butscher, J. A. Agner, H. Schmutz, F. Merkt, and J. Deiglmayr, Phys. Rev. A **100**, 012501 (2019), URL <https://link.aps.org/doi/10.1103/PhysRevA.100.012501>.
- [28] T. F. Gallagher, R. Kachru, and N. H. Tran, Phys. Rev. A **26**, 2611 (1982), URL <https://link.aps.org/doi/10.1103/PhysRevA.26.2611>.
- [29] B. M. McLaughlin and J. F. Babb, Monthly Notices of the Royal Astronomical Society **486**, 245 (2019), ISSN 0035-8711, <https://academic.oup.com/mnras/article-pdf/486/1/245/28310898/stz790.pdf>, URL <https://doi.org/10.1093/mnras/stz790>.
- [30] J. A. Samson (Academic Press, 1966), vol. 2 of *Advances in Atomic and Molecular Physics*, pp. 177 – 261, URL <http://www.sciencedirect.com/science/article/pii/S0065219908602195>.
- [31] J. Berkowitz, in *Photoabsorption, Photoionization, and Photoelectron Spectroscopy*, edited by J. Berkowitz (Academic Press, 1979), pp. 73 – 154, ISBN 978-0-12-091650-4, URL <http://www.sciencedirect.com/science/article/pii/B9780120916504500116>.
- [32] G. W. F. Drake and R. A. Swinson, Phys. Rev. A **42**, 1123 (1990), URL <https://link.aps.org/doi/10.1103/PhysRevA.42.1123>.
- [33] W. Li, I. Mourachko, M. W. Noel, and T. F. Gallagher, Phys. Rev. A **67**, 052502 (2003), URL <https://link.aps.org/doi/10.1103/PhysRevA.67.052502>.
- [34] J. Nipper, J. B. Balewski, A. T. Krupp, B. Butscher, R. Löw, and T. Pfau, Phys. Rev. Lett. **108**, 113001 (2012), URL <https://link.aps.org/doi/10.1103/PhysRevLett.108.113001>.
- [35] A. Reinhard, T. Cubel Liebisch, K. C. Younge, P. R. Berman, and G. Raithel, Phys. Rev. Lett. **100**, 123007 (2008), URL <https://link.aps.org/doi/10.1103/PhysRevLett.100.123007>.
- [36] P. Bohlouli-Zanjani, J. A. Petrus, and J. D. D. Martin, Phys. Rev. Lett. **98**, 203005 (2007), URL <https://link.aps.org/doi/10.1103/PhysRevLett.98.203005>.
- [37] B. R. Mollow, Phys. Rev. **175**, 1555 (1968), URL <https://link.aps.org/doi/10.1103/PhysRev.175.1555>.
- [38] T. F. Gallagher, L. M. Humphrey, W. E. Cooke, R. M. Hill, and S. A. Edelstein, Phys. Rev. A **16**, 1098 (1977), URL <https://link.aps.org/doi/10.1103/PhysRevA.16.1098>.
- [39] K. A. Safinya, T. F. Gallagher, and W. Sandner, Phys. Rev. A **22**, 2672 (1980), URL <https://link.aps.org/doi/10.1103/PhysRevA.22.2672>.
- [40] W. F. Holmgren, R. Trubko, I. Hromada, and A. D. Cronin, Phys. Rev. Lett. **109**, 243004 (2012), URL <https://link.aps.org/doi/10.1103/PhysRevLett.109.243004>.
- [41] J. Reader, J. Opt. Soc. Am. **65**, 286 (1975), URL <https://doi.org/10.1364/JOSA.65.000286>.

B | Hydrogen Radial Functions and Spherical Harmonics

Radial Functions for $n = 1 - 3, \ell = 0 - 2$

$$R_{1,0}(r) = \frac{2}{a_0^{3/2}} \exp\left(-\frac{r}{a_0}\right)$$

$$R_{2,0}(r) = \frac{2}{(2a_0)^{3/2}} \left(1 - \frac{r}{2a_0}\right) \exp\left(-\frac{r}{2a_0}\right)$$

$$R_{2,1}(r) = \frac{1}{\sqrt{3}(2a_0)^{3/2}} \frac{r}{a_0} \exp\left(-\frac{r}{2a_0}\right)$$

$$R_{3,0}(r) = \frac{2}{(3a_0)^{3/2}} \left(1 - \frac{2r}{3a_0} + \frac{2r^2}{27a_0^2}\right) \exp\left(-\frac{r}{3a_0}\right)$$

$$R_{3,1}(r) = \frac{4\sqrt{2}}{9(3a_0)^{3/2}} \frac{r}{a_0} \left(1 - \frac{r}{6a_0}\right) \exp\left(-\frac{r}{3a_0}\right)$$

$$R_{3,2}(r) = \frac{2\sqrt{2}}{27\sqrt{5}(3a_0)^{3/2}} \left(\frac{r}{a_0}\right)^2 \exp\left(-\frac{r}{3a_0}\right)$$

Spherical Harmonics for $\ell = 0 - 2$

$$Y_{0,0} = \frac{1}{\sqrt{4\pi}}$$

$$Y_{1,0} = \sqrt{\frac{3}{4\pi}} \cos \theta$$

$$Y_{1,\pm 1} = \mp \sqrt{\frac{3}{8\pi}} \sin \theta e^{\pm i\phi}$$

$$Y_{2,0} = \sqrt{\frac{5}{16\pi}} (3 \cos^2 \theta - 1)$$

$$Y_{2,\pm 1} = \mp \sqrt{\frac{15}{8\pi}} \sin \theta \cos \theta e^{\pm i\phi}$$

$$Y_{2,\pm 2} = \sqrt{\frac{15}{32\pi}} \sin^2 \theta e^{\pm 2i\phi}$$

C | Expectation values for hydrogenic states

$$G_P(n, \ell) = \frac{2^P Z^P (2\ell - P + 2)!}{n^{P+1} (2\ell + P - 1)!} \quad (\text{C.1})$$

$$f_r(\ell) = \frac{(\ell + r)!}{(\ell - r)!} \quad (\text{C.2})$$

$$\langle r^{-2} \rangle = G_2(n, \ell) / 2$$

$$\langle r^{-3} \rangle = n G_3(n, \ell)$$

$$\langle r^{-4} \rangle = G_4(n, \ell) [3n^2 - f_1(\ell)]$$

$$\langle r^{-5} \rangle = 6G_5(n, \ell) \left\{ \frac{5}{3}n^3 - n \left[f_1(\ell) - \frac{1}{3} \right] \right\}$$

$$\langle r^{-6} \rangle = 3G_6(n, \ell) \left\{ \frac{35}{3}n^4 - 10n^2 \left[f_1(\ell) - \frac{5}{6} \right] + f_2(\ell) \right\}$$

$$\langle r^{-7} \rangle = 30G_7(n, \ell) \left\{ \frac{21}{5}n^5 - \frac{14}{3}n^3 \left[f_1(\ell) - \frac{3}{2} \right] + n \left[f_2(\ell) - \frac{4}{3}f_1(\ell) + \frac{4}{5} \right] \right\}$$

⋮

G. W. F. Drake and R. A. Swainson, Phys. Rev. A **42**, 1123 (1990), URL <https://link.aps.org/doi/10.1103/PhysRevA.42.1123>.

D | Calculated quantum defects for $n = 10 - 40, \ell = 4 - 8$

Calculated quantum defects for $n = 10 - 40$ and $\ell = 4 - 8$ using the core polarizability results in this work.

n	ℓ	δ_ℓ	Error
10	4	0.00372727	0.00000163
10	5	0.00127567	0.00000044
10	6	0.00052043	0.00000017
10	7	0.00023848	0.00000008
10	8	0.0001185	0.00000004
11	4	0.00377506	0.00000166
11	5	0.0013006	0.00000045
11	6	0.00053523	0.00000018
11	7	0.00024802	0.00000008
11	8	0.00012501	0.00000004
12	4	0.00381144	0.00000169
12	5	0.00131956	0.00000046
12	6	0.00054648	0.00000018
12	7	0.00025527	0.00000008
12	8	0.00012996	0.00000004
13	4	0.00383977	0.00000171
13	5	0.00133433	0.00000047
13	6	0.00055525	0.00000019
13	7	0.00026091	0.00000009
13	8	0.00013382	0.00000004
14	4	0.00386226	0.00000173
14	5	0.00134605	0.00000047
14	6	0.0005622	0.00000019
14	7	0.00026539	0.00000009
14	8	0.00013687	0.00000005

n	ℓ	δ_ℓ	Error
15	4	0.00388042	0.00000174
15	5	0.00135551	0.00000047
15	6	0.00056781	0.00000019
15	7	0.000269	0.00000009
15	8	0.00013934	0.00000005
16	4	0.00389529	0.00000175
16	5	0.00136325	0.00000048
16	6	0.0005724	0.00000019
16	7	0.00027196	0.00000009
16	8	0.00014136	0.00000005
17	4	0.00390762	0.00000176
17	5	0.00136966	0.00000048
17	6	0.00057621	0.00000019
17	7	0.00027441	0.00000009
17	8	0.00014303	0.00000005
18	4	0.00391797	0.00000177
18	5	0.00137504	0.00000048
18	6	0.0005794	0.00000019
18	7	0.00027646	0.00000009
18	8	0.00014443	0.00000005
19	4	0.00392672	0.00000177
19	5	0.00137959	0.00000048
19	6	0.0005821	0.0000002
19	7	0.0002782	0.00000009
19	8	0.00014562	0.00000005
20	4	0.0039342	0.00000178
20	5	0.00138348	0.00000049
20	6	0.0005844	0.0000002
20	7	0.00027969	0.00000009
20	8	0.00014663	0.00000005

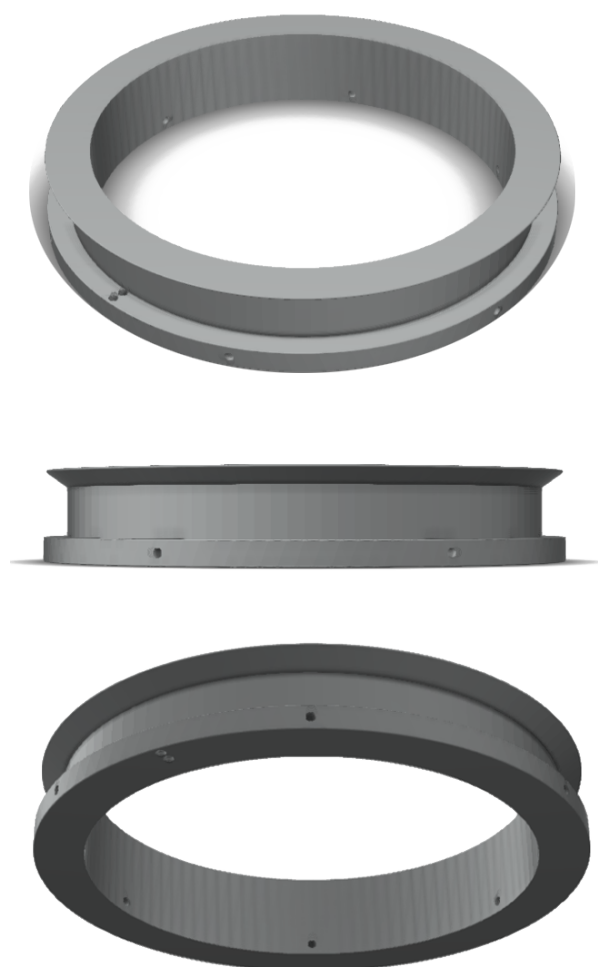
n	ℓ	δ_ℓ	Error
21	4	0.00394064	0.00000179
21	5	0.00138683	0.00000049
21	6	0.00058638	0.0000002
21	7	0.00028096	0.00000009
21	8	0.00014751	0.00000005
22	4	0.00394623	0.00000179
22	5	0.00138973	0.00000049
22	6	0.0005881	0.0000002
22	7	0.00028207	0.00000009
22	8	0.00014826	0.00000005
23	4	0.0039511	0.00000179
23	5	0.00139226	0.00000049
23	6	0.0005896	0.0000002
23	7	0.00028304	0.00000009
23	8	0.00014892	0.00000005
24	4	0.00395538	0.0000018
24	5	0.00139448	0.00000049
24	6	0.00059092	0.0000002
24	7	0.00028389	0.00000009
24	8	0.0001495	0.00000005
25	4	0.00395916	0.0000018
25	5	0.00139644	0.00000049
25	6	0.00059208	0.0000002
25	7	0.00028463	0.00000009
25	8	0.00015001	0.00000005

n	ℓ	δ_ℓ	Error
26	4	0.00396251	0.0000018
26	5	0.00139818	0.00000049
26	6	0.00059311	0.0000002
26	7	0.0002853	0.00000009
26	8	0.00015046	0.00000005
27	4	0.0039655	0.0000018
27	5	0.00139973	0.00000049
27	6	0.00059403	0.0000002
27	7	0.00028589	0.00000009
27	8	0.00015087	0.00000005
28	4	0.00396818	0.00000181
28	5	0.00140111	0.00000049
28	6	0.00059485	0.0000002
28	7	0.00028642	0.0000001
28	8	0.00015123	0.00000005
29	4	0.00397058	0.00000181
29	5	0.00140236	0.00000049
29	6	0.00059559	0.0000002
29	7	0.00028689	0.0000001
29	8	0.00015155	0.00000005
30	4	0.00397275	0.00000181
30	5	0.00140348	0.00000049
30	6	0.00059626	0.0000002
30	7	0.00028732	0.0000001
30	8	0.00015184	0.00000005

n	ℓ	δ_ℓ	Error
31	4	0.00397472	0.00000181
31	5	0.0014045	0.0000005
31	6	0.00059686	0.0000002
31	7	0.00028771	0.0000001
31	8	0.00015211	0.00000005
32	4	0.0039765	0.00000181
32	5	0.00140542	0.0000005
32	6	0.00059741	0.0000002
32	7	0.00028806	0.0000001
32	8	0.00015235	0.00000005
33	4	0.00397812	0.00000181
33	5	0.00140626	0.0000005
33	6	0.0005979	0.0000002
33	7	0.00028838	0.0000001
33	8	0.00015257	0.00000005
34	4	0.00397961	0.00000182
34	5	0.00140703	0.0000005
34	6	0.00059836	0.0000002
34	7	0.00028867	0.0000001
34	8	0.00015277	0.00000005
35	4	0.00398097	0.00000182
35	5	0.00140773	0.0000005
35	6	0.00059877	0.0000002
35	7	0.00028894	0.0000001
35	8	0.00015295	0.00000005

n	ℓ	δ_ℓ	Error
36	4	0.00398222	0.00000182
36	5	0.00140838	0.0000005
36	6	0.00059916	0.0000002
36	7	0.00028919	0.0000001
36	8	0.00015312	0.00000005
37	4	0.00398336	0.00000182
37	5	0.00140897	0.0000005
37	6	0.00059951	0.0000002
37	7	0.00028941	0.0000001
37	8	0.00015327	0.00000005
38	4	0.00398442	0.00000182
38	5	0.00140952	0.0000005
38	6	0.00059983	0.0000002
38	7	0.00028962	0.0000001
38	8	0.00015342	0.00000005
39	4	0.0039854	0.00000182
39	5	0.00141002	0.0000005
39	6	0.00060013	0.0000002
39	7	0.00028981	0.0000001
39	8	0.00015355	0.00000005
40	4	0.00398631	0.00000182
40	5	0.00141049	0.0000005
40	6	0.00060041	0.0000002
40	7	0.00028999	0.0000001
40	8	0.00015367	0.00000005

E | 3D printed coil forms



Coil forms to fit around and secure to 8" vacuum chamber flanges. Additive manufacturing (3D printing) was employed to fabricate these custom parts for this experiment. Wires are wound to 250 turns around this coil form and the coil form is secured to the outer diameter of the vacuum flange.

F | Continuum Surelite SLI-20

Trigger Setup

Section 3: System Operation

Table 6 ASCII response

Returns	Description
00	Normal return
01	Surelite not in serial mode
02	Coolant flow interrupted
03	Coolant temperature over temp
04	(not used)
05	Laser head problem
06	External interlock
07	End of charge not detected before lamp fire
08	Simmer not detected
09	Flow switch stuck on.

The response to **SC** (Shot count) is a 9 digit ASCII code terminated by a Carriage Return. An example is shown in Table 7 below.

Table 7 SC response

Returns	Description
000123456	shot count = 123,456

To disable RS232

1. With system running, transmit the ASCII code ST 0.
2. Press **START/STOP** button to off.
3. Press **SELECT** button to **Son**.
4. Press **ARROW DOWN** button to **SoF**.
5. Resume normal operation.

Direct Access Triggering (DAT)

Stanford Research Pulse Generator Setup

NECESSARY EQUIPMENT

- 1 ea. Delay Generator model #DG535
- 2 ea. Standard BNC cables
- 1 ea. 9 pin “D” connector, male

STEPS

1. Make up a special cable consisting of 2 BNC cables and a 9 pin D male.
 - Label one of the BNC cables FIRE and the other Q-SWITCH.
 - Take the FIRE and Q-SWITCH BNC cables and remove the connector from one end and expose the center conductor and shield.
 - Solder center conductor of the FIRE BNC to pin 7 of the 9 pin D connector.

Continuum Surelite Laser

- Solder the shield of the FIRE BNC to pin 2 of the 9 pin D connector.
 - Solder the center conductor of the Q-SWITCH BNC to pin 6 of the 9 pin D connector.
 - Solder the shield of the Q-SWITCH BNC to pin 3 of the 9 pin D connector.
2. Program the DG535 as follows:
 - TRIGGER - set to internal and 10 Hz or desired rep rate.
 - OUTPUTS - set all outputs to High Z, TTL and NOR-MAL
 - DELAYS -
 - $A = T = + 0$
 - $B = A + 10 \mu s$
 - $C = A + 150 \mu s$
 - $D = C + 10 \mu s$
 3. Connect the special cable 9 pin D to the external connector on front of PCU.
 4. Connect the FIRE BNC to AB\Bar (positive going to negative).
 5. Connect the Q-switch BNC to CD/Bar (positive going to negative).
 6. At the rear of the PCU flip the Q-SWITCH SELECT toggle to the EXT position (for lowest jitter).
 7. Start up the Surelite as follows:
 - Toggle on AC power
 - Turn keyswitch to ON
 - Press SELECT button until "EoP" is displayed
 - Press UP ARROWS so that display reads "Eon"
 - Press on the START/STOP button

**LASER RADIATION!**

Lasing output occurs at next step!

- Press on the SHUTTER button.
8. Adjust the Delay of "C" on the DG535 to maximize laser power. Final "C" delay is normally between 100 μs and 300 μs .

To enable DAT

The Surelite laser may be directly controlled by user provided TTL level signals. Select this mode of operation when the application requires laser output be synchronized with other occurrences. Listed below are the steps necessary to externally trigger your Surelite.

Section 3: System Operation**NECESSARY EQUIPMENT**

- User supplied TTL negative going signal (5 V .0 V 10 μ s wide)
- 9 pin D style male connector
- Shielded cable (suggest RG-174 coaxial cable)

DAT Mode 1 (± 10 ns jitter)

In this mode the operator can fire the laser by providing a single negative going pulse (5 V .0 V). Jitter time of the laser output with respect to the input fire command will be ± 10 ns. Lead time between the fire command and laser output will be ~ 180 μ s.

1. Flip up external Q-switch toggle located on rear panel of the PCU to **INT** position (see page 24).
2. Solder center lead of coaxial cable to pin 7 of a D style male connector. Solder shield of same coaxial cable to pin 2 of the male D connector.
3. Plug D connector made in step 2 to the **EXTERNAL** connector on front panel of the PCU.
4. Plug the Surelite into ac supply and toggle on the **AC POWER**.
5. Turn the keyswitch to the **ON** position.
6. Press the **SELECT** button until **EoF** is displayed on the LED readout.
7. Press **UP ARROW** button so that display reads **Eon**.
8. Open exit port shutter at front of the laser bench.
9. Press the **START/STOP** button located of front panel of the PCU to **ON**.
10. Press the **SHUTTER** button located of front panel of the PCU to **ON**.
11. Input the Fire Command onto pin 7 of the D connector. User circuit should generate a TTL level pulse that goes from 5V .0V for 10 μ s each time laser output is desired.

DAT Mode 2 (± 1 ns jitter)

This mode give the lowest possible jitter between input commands and laser output. Mode 2 requires the input of 2 TTL level negative going signals (5 V .0 V, 10 μ s wide).

The first TTL signal called Fire Command will cause the laser head lamps to flash. This signal proceeds lasing by ~ 180 μ s. The second TTL signal called Q-switch Command fires the Pockels cell and precedes lasing by ~ 170 ns.

1. Flip down external Q-switch toggle located on rear panel of the **PCU** to **EXT** position (see Figure facing page 3-1).

Continuum Surelite Laser

2. Make the following connections on the D style male connector:
 - Q-switch Command - solder center lead of co-axial cable to pin 6 and solder shield of same coaxial cable to pin 3 of the connector.
 - Fire Command - solder center lead of a second coaxial cable to pin 7. Solder shield of second coaxial cable to pin 2.
3. Plug D connector made in step 2 to the **EXTERNAL** connector on front panel of the **PCU**.
4. Plug the Surelite into ac supply and toggle on the **AC POWER**.
5. Turn the keyswitch to the **ON** position.
6. Press the **SELECT** button until **EoF** is displayed on the LED readout.
7. Press **UP ARROW** button so that display reads **Eon**.
8. Open exit port shutter at front of the laser bench.
9. Press the **START/STOP** button located of front panel of the **PCU** to **ON**.
10. Press the **SHUTTER** button located of front panel of the **PCU** to **ON**.
11. Input the Fire Command onto pin 7 of the D connector (TTL level 5 V .0 V, 10 μ s wide).
12. Input Q-switch Command onto pin 6 with a delay of \sim 180 μ s with respect to Fire Command (TTL level 5 V .0 V, 10 μ s wide).
13. Adjust .T between Fire Command and Q-switch Command for maximum energy.

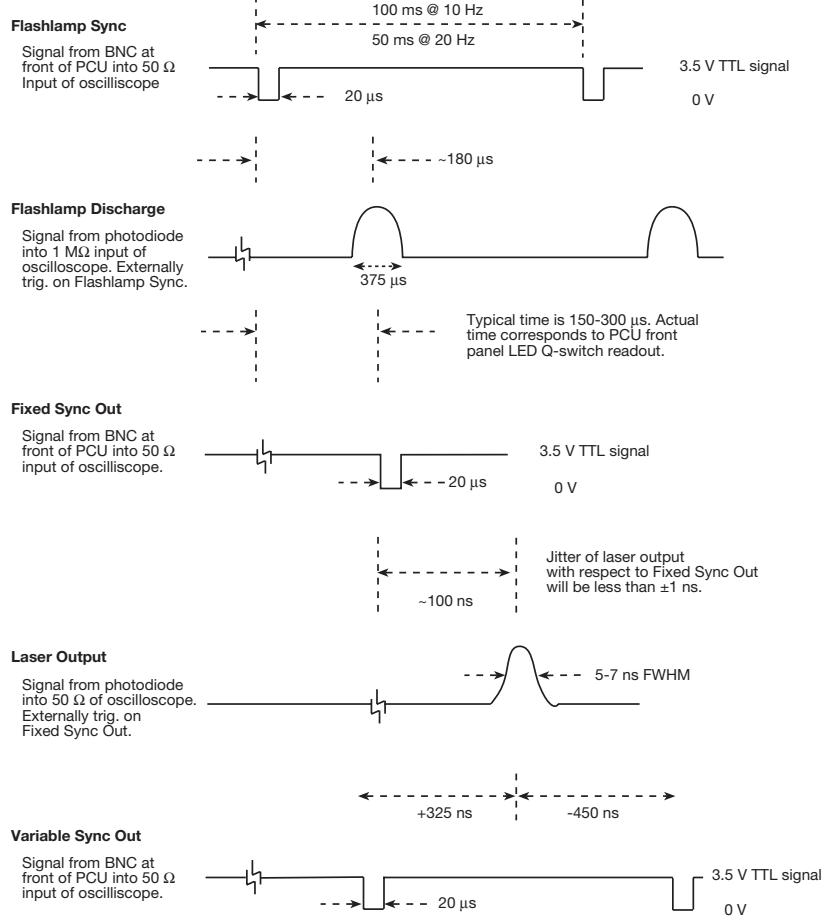
Note: When running the system in the external mode you must flash the laser head lamps at approximately the same frequency that the system was optimized at time of purchase. Changing lamp frequency will change thermal lensing of the YAG rod which can result in reduced system performance.

To disable DAT

1. Press the **START/STOP** button to stop lamps from flashing.
2. Press the **SELECT** button to **Eon**.
3. Press the **ARROW DOWN** button to **EoF**.
4. Resume normal operation.

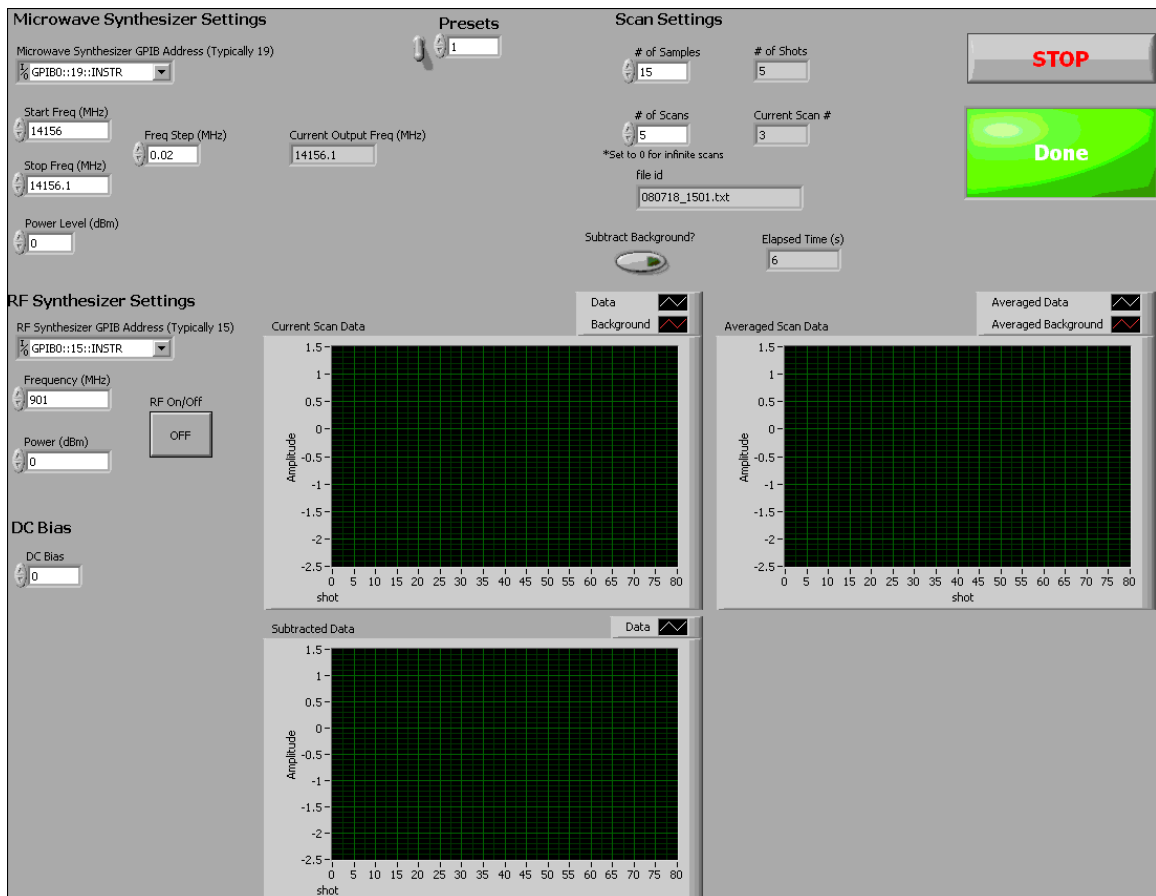
Section 3: System Operation

Figure 27 Surelite chronograph

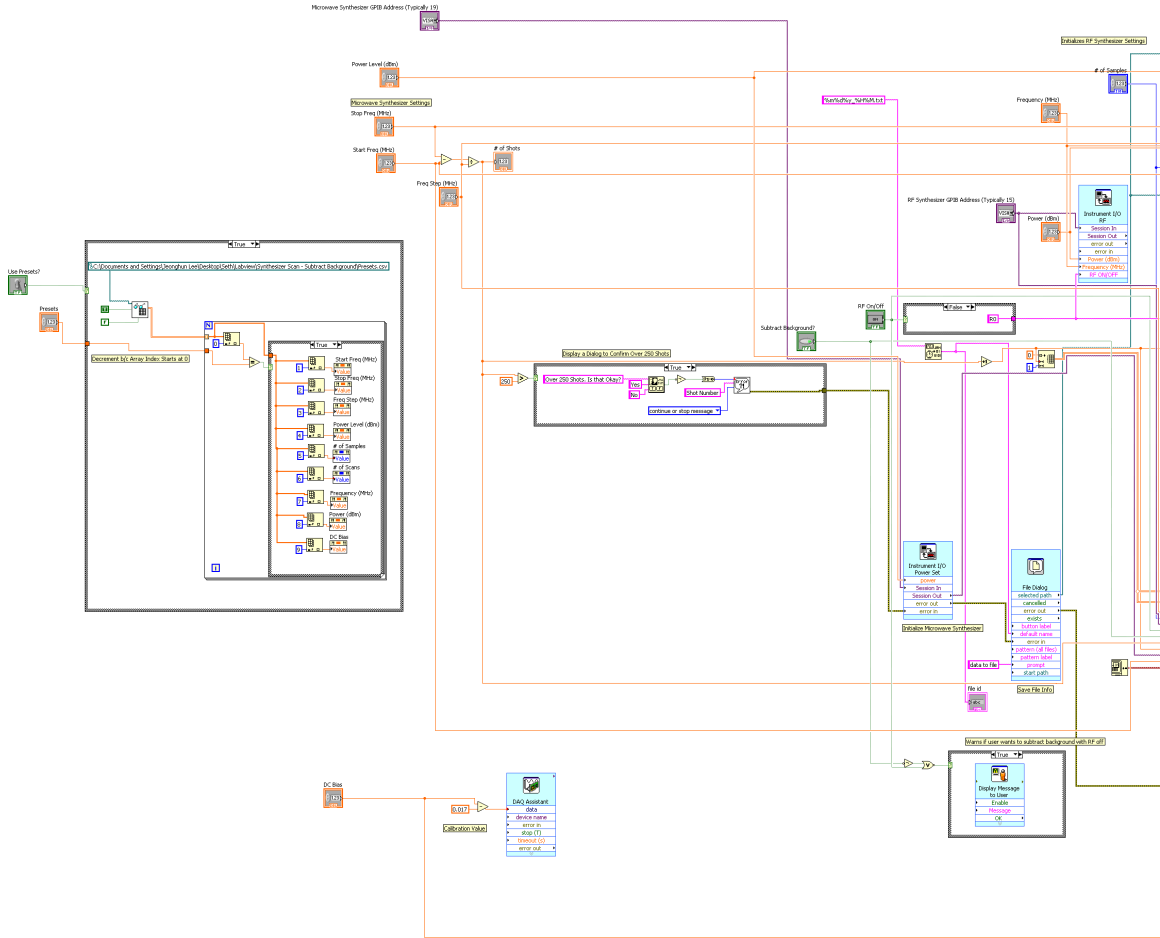


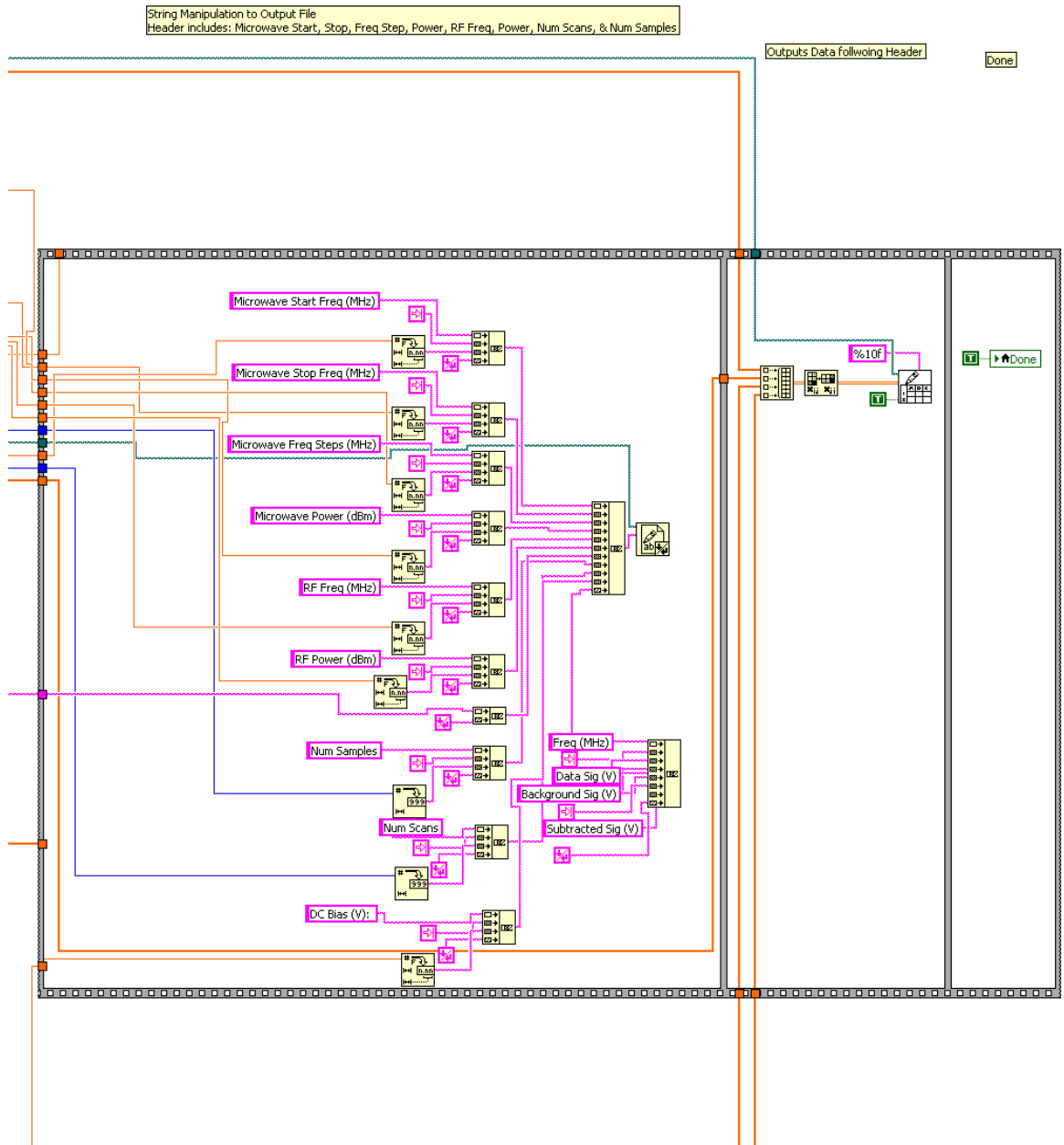
G | LabView experiment control software

G.1 Front panel



G.2 Back panel





H | Laser dyes

H.1 Stilbene 420



2150 Bixby Road
Lockbourne, OH 43137
Tel: 614.492.5610
E-mail: info.exciton@luxotticaretail.com
www.exciton.luxottica.com

STILBENE 420

Synonym: 2,2'-([1,1'-biphenyl]-4,4'-diyldi-2,1-ethenediyl)bis-benzenesulfonic acid disodium salt; Stilbene 3

Catalog No.: 04200

CAS No.: 27344-41-8

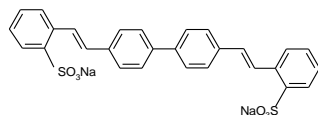
Chemical Name: C₂₈H₂₀O₆S₂·2Na

Molecular Weight: 562.56

Appearance: Yellow powder

Molar Absorptivity (in methanol): 270nm-400nm, absorption maximum 353nm

Structure:



Lasing Wavelength Max. (nm)	Range (nm)	Pump Source (nm)	Solvent	Concentration (molar)	Abs λ-max	FI λ-
424	410-454	XeCl(308) ¹¹⁴	EtOH/H ₂ O, 9/1	1.4 x 10 ⁻³	349 ^m	425 ^o
425	405-467	XeCl(308) ¹¹⁸	Ethanol	1 x 10 ⁻³ (osc)		402
425	412-435	XeCl(308) ¹¹⁰	Methanol	1 x 10 ⁻³		
	450(sh)					
425	412-436	Nd:YAG(355, m-I, QS, 100ps) ¹⁶⁹	Methanol	3 x 10 ⁻³		
425	412-444	Nd:YAG(355) ⁵⁷	Methanol	3.9 x 10 ⁻⁴ (osc), 1 x 10 ⁻⁴ (amp)		
425	415-435	Nd:YAG(355) ¹⁰⁹	Methanol/ethanol, 1/1	1.5 x 10 ⁻³		
425	420-459	Nd:YAG(355) ⁵³	Methanol	5.3 x 10 ⁻⁴ (osc), 9.1 x 10 ⁻⁵ (amp)		
424	415-437	N ₂ (337) ¹³⁹	Methanol	1.7 x 10 ⁻³		
425	400-460	N ₂ (337) ⁹⁰	EtOH/H ₂ O, 1/4	2.1 x 10 ⁻³		
425	407-468	N ₂ (337) ¹¹⁴	EtOH/H ₂ O, 8/2	9 x 10 ⁻⁴		
425	408-453	N ₂ (337) ⁴¹	Methanol	1.8 x 10 ⁻³		
427	400-465	N ₂ (337) ¹⁸³	Methanol	1.8 x 10 ⁻³		
431	415-458	N ₂ (337) ⁴¹	H ₂ O+NP-10	1.8 x 10 ⁻³		
445	421-468	N ₂ (337) ⁴¹	H ₂ O	1.8 x 10 ⁻³		
432	406-448	Ar(uv) ⁴²	EG/methanol, 9/1	2 x 10 ⁻³		
432	420-470	Ar(334-364) ²⁰⁶	EG	2 x 10 ^{-3*}		
435	407-466	Ar(334-364) ^{123,187}	EG			
449	420-470	Ar(uv) ⁵²	EG	1.5 x 10 ⁻³		
449	436-493	Ar(uv) ⁴²	EG/methanol, 9/1	2 x 10 ⁻³		
425	400-480	Kr(uv) or Ar(uv) ⁶⁸	EG	80% pump absorption		

* This represents a maximum value. Concentration should be adjusted to 80-85% absorption of the pump light.

m = methanol; e = ethanol; EtOH/H₂O = Ethanol/water; EG = Ethylene glycol

H.2 LDS 722



2150 Bixby Road
Lockbourne, OH 43137
Tel: 614.492.5610
E-mail: info.exciton@luxotticaretail.com
www.exciton.luxottica.com

LDS 722

Synonym: 4-[4-(4-(dimethylamino)phenyl)-1,3-butadienyl]-1-ethyl-pyridinium perchlorate; Pyridine 2

Catalog No.: 07220

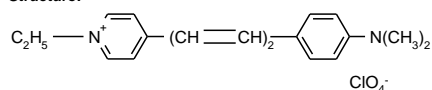
CAS No.: 89846-21-9

Chemical Formula: C₁₉H₂₃N₂.ClO₄

MW: 378.85

Appearance: Purple crystals

Structure:



Lasing Wavelength Max. (nm)	Range (nm)	Pump Source (nm)	Solvent	Concentration (molar)	Abs λ-max	Fl λ-max
715	686-795	Nd:YAG(532) ^{127c}	Methanol		494 ^m	702 ^m
718	691-751	Nd:YAG(532) ²³⁹	Ethanol	6.6 x 10 ⁻⁴		
722	685-760	Nd:YAG(532) ⁵⁷	Methanol			
724		Nd:YAG(532)→F548(544) ¹⁴⁸	Methanol	3.4 x 10 ⁻⁴ (osc), 1.3 x 10 ⁻⁴ (amp)		
735	700-780	N ₂ (DFDL) ¹⁶²	DMSO	7 x 10 ⁻³		
713	680-795	Ar(458-514) ²⁰⁶	PC/EG,2/8	4 x 10 ^{-3*}		
725	690-770	Ar(Blue/Green,SF) ⁶⁸	PC/EG	2.7 x 10 ⁻³		
726	688-775	Ar(Blue/Green,bb) ⁶⁸	PC/EG			
745	685-800	Ar(Blue/Green,SF) ⁶⁸	PC/EG	2.7 x 10 ⁻³		
747	682-810	Ar(Blue/Green,bb) ⁶⁸	PC/EG			
722	687-755	Cu(511,578) ¹⁷⁵	Methanol	2.6 x 10 ⁻³		

* This represents a maximum value. Concentration should be adjusted to 80-85% absorption of the pump light.

m = methanol, DMSO = dimethylsulfoxide, EG = ethylene glycol, PC = propylene carbonate

REFERENCES:

57. Quanta-Ray, Note: Quanta-Ray is now incorporated as a part of Spectra-Physics, 1250 W. Middlefield Road, Mountain View, CA 94039
68. Coherent Inc., 3210 Porter Dr., Palo Alto, CA 94304
127. a. Cw Operation of Laser Dyes Styryl-9 and Styryl-11, J. Hoffnagle, L. Ph. Roesch, N. Schlumpf and A. Weis, *Optics Commun.*, 42, 267 (1982); b. K. Kato, see Reference 5 in 127 a ; c. K. Kato, unpublished results
148. Dye Laser Radiation in the 605-725nm Region Pumped by a 544nm Fluorescein Dye Laser, K.D. Bonin and T.J. McIlrath, *Applied Optics*, 23(17), 2854 (1984)
162. Novel Method for Wavelength Tuning of Distributed Feedback Dye Lasers, J. Jasny, *Optics Commun.*, 53(4), 238 (1985)
175. CVL-Pumped Dye Laser For Spectroscopic Application, M. Broyer, J. Chevalyere, G. Delacretaz and L. Wöste, *App. Phys. B*, 35, 31 (1984)
206. Coherent Inc., 3210 Porter Dr., Palo Alto, CA 94304; (599 Composite Tuning Curves, 1992: The concentration shown represents a maximum value. The final concentration should be adjusted to obtain 80-85% absorption of the pump light.)
239. P. Jauernik, private commun., Sirah Laser- und Plasmatechnik, 2003.

For a current list of biology, biological stain, or biochemistry references for LDS 722 from PubMed, click on the following link:

[LDS 722 or Pyridine 2](#)

Index

- ac Stark effect, 76
- adiabatic approximation, 16
- anode, 55
- atomic parity violation, 4
- Bohr magnetron, 80
- computer aided design (CAD), 86
- core polarization model, 15
- dc Stark effect, 71
- delayed field ionization (DFI), 50
- diffusion vacuum pump, 30
- dipole matrix elements, 8
- Direct Access Trigger (DAT), 59
- dynamic polarizability, 10
- electric polarizability, 9
- field effect transistor (FET), 53
- forbidden transition, 7
- fundamental symmetry, 2
- Granville Phillips 330 Hot Cathode Ion Gauge
 - Controller, 32
- gyromagnetic ratio, 80
- ionization gauge, 32
- Landé formula, 79
- Landé g-factor, 80
- Legendre polynomials, 115
- mechanical roughing pump, *see* rotary vane pump, roughing pump, forepump
- microwave horn antenna, 48
- monochromator, 45
- multi-channel plate (MCP), 28, 55
- non-adiabatic effect, 112
- oscillator strength, 123
- parity transformation, 2
- parity violation, 2, 4
- photodiode detector, 45
- photoionization cross-section, 124
- physics beyond the Standard Model, 1
- PNC transition rate, 7
- pulse modulation, 47
- quadratic Stark effect, 72
- quantum defect, 14, 130
- Rabi frequency, 70
- radial functions, 6
- rotary vane pump, 30
- rotating wave approximation (RWA), 77
- rydberg atom, 12
- Rydberg formula, 14
- selection rule, 7
- selection rules, 4
- selective field ionization (SFI), 50
- signal to noise ratio (SNR), 27
- single-photon transition, 47
- spectroscopy, 66
- spherical harmonics, 6
- spin-orbit interaction, 69
- spontaneous emission, 8
- Stark effect, 9, 71
- Taylor expansion, 119
- The Standard Model, 1
- thermal beam, 34
- thermocouple gauge, 32
- transform broadening, 70, 80
- tune-out wavelength spectroscopy, 10
- vacuum chamber, 28

weak mixing angle, 3

Zeeman effect, 79